

AD-A112 977

AEROSPACE CORP EL SEGUNDO CA VEHICLE ENGINEERING DIV

F/G 7/4

THE HIGH TEMPERATURE THERMOCHEMICAL PROPERTIES OF CARBON. (U)

MAR 82 R L BAKER, M A COVINGTON

F04701-81-C-0082

UNCLASSIFIED

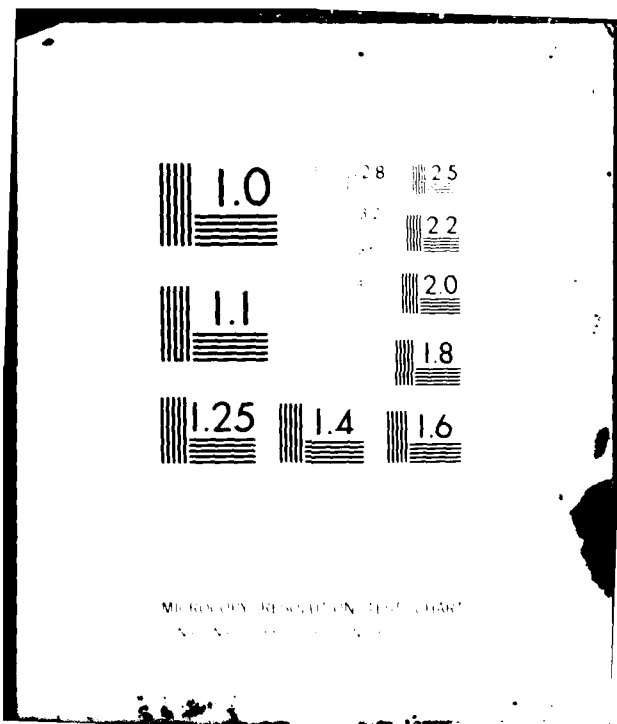
TR-0082(2729)-1

SD-TR-82-19

NL

1 OF 1
AD-2
2-9-82

END
DATE
FILED
04-18-82
DTIC



ADA112977

REPORT SD-TR-82-19

(12)

The High Temperature Thermochemical Properties of Carbon

R. L. BAKER
Vehicle Engineering Division
Engineering Group
The Aerospace Corporation
El Segundo, Calif. 90245

and

M. A. COVINGTON
NASA Ames Research Center
Moffet Field, Calif. 94035

31 March 1982

Interim Report

APPROVED FOR PUBLIC RELEASE;
DISTRIBUTION UNLIMITED

REPRODUCTION IN WHOLE OR IN PART
IS PERMITTED FOR ANY PURPOSE OF
THE UNITED STATES GOVERNMENT

Prepared for
OFFICE OF NAVAL RESEARCH
Arlington, Va. 22217
SPACE DIVISION
AIR FORCE SYSTEMS COMMAND
Los Angeles Air Force Station
P.O. Box 92960, Worldway Postal Center
Los Angeles, Calif. 90009

STIC
SELECTED
APR 6 1982
H

DTIC FILE COPY

8.5 116

This interim report was prepared for the Office of Naval Research, Arlington, VA 22217, by The Aerospace Corporation, El Segundo, CA 90245, under Contract No. F04701-81-C-0082 with the Space Division, Air Force Systems Command, P.O. Box 92960, Worldway Postal Center, Los Angeles, CA 90009. It was reviewed and approved for The Aerospace Corporation by E.G. Hertler, Director, Aero Engineering Subdivision.

This report has been reviewed by the Public Affairs Office (PAS) and is releasable to the National Technical Information Service (NTIS). At NTIS, it will be available to the general public, including foreign nations.

This technical report has been reviewed and is approved for publication. Publication of this report does not constitute Air Force approval of the report's findings or conclusions. It is published only for the exchange and stimulation of ideas.



Gerhard E. Aichinger
Technical Advisor

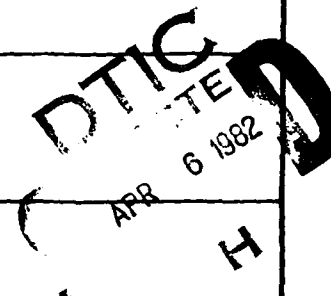
FOR THE COMMANDER



Kalman L. Huler
Chief, Special Contracts Office

UNCLASSIFIED

SECURITY CLASSIFICATION OF THIS PAGE (When Data Entered)

REPORT DOCUMENTATION PAGE		READ INSTRUCTIONS BEFORE COMPLETING FORM
1. REPORT NUMBER SD-TR-82-19	2. GOVT ACCESSION NO. AD-A112 977	3. RECIPIENT'S CATALOG NUMBER
4. TITLE (and Subtitle) THE HIGH TEMPERATURE THERMOCHEMICAL PROPERTIES OF CARBON	5. TYPE OF REPORT & PERIOD COVERED Interim Report	
7. AUTHOR(s) R. L. Baker (The Aerospace Corporation) M. A. Covington (NASA Ames Research Center)	6. PERFORMING ORG. REPORT NUMBER TR-0082(2729)-1	
9. PERFORMING ORGANIZATION NAME AND ADDRESS The Aerospace Corporation El Segundo, California 90245	8. CONTRACT OR GRANT NUMBER(s) F04701-81-C-0082	
11. CONTROLLING OFFICE NAME AND ADDRESS Office of Naval Research Eastern/Central Regional Office Boston, MS 02210	10. PROGRAM ELEMENT, PROJECT, TASK AREA & WORK UNIT NUMBERS	
14. MONITORING AGENCY NAME & ADDRESS (if different from Controlling Office) Space Division Air Force Systems Command Los Angeles, CA 90009	12. REPORT DATE 31 March 1982	13. NUMBER OF PAGES 93
	15. SECURITY CLASS. (of this report) Unclassified	16. DECLASSIFICATION/DOWNGRADING SCHEDULE
18. DISTRIBUTION STATEMENT (of this Report) Approved for public release; distribution unlimited.	17. DISTRIBUTION STATEMENT (of the abstract entered in Block 20, if different from Report) 	
19. KEY WORDS (Continue on reverse side if necessary and identify by block number) carbon vapor pressure, melt temperature carbon species vaporization coefficients high temperature carbon ablation laser-induced phase change nonequilibrium phase change	nonlinear Knudsen layer modeling molecular dynamics simulation deg	
20. ABSTRACT (Continue on reverse side if necessary and identify by block number) A new method based on the combined use of carbon laser ablation data and analytical modeling has been used to determine carbon vapor pressure and vaporization coefficients at high temperatures (up to 4600°K). The JANAF carbon species C ₃ thermochemical data have been rejected in favor of alternate data. The JANAF data predict a total vapor pressure too low by a factor of		

UNCLASSIFIED

SECURITY CLASSIFICATION OF THIS PAGE(When Data Entered)

19. KEY WORDS (Continued)

20. ABSTRACT (Continued)

greater than two at 4000°K. The melt temperature of carbon has been concluded to be greater than 4500°K using a surface reflectivity method. The temperature dependence of vaporization coefficients for carbon species has been determined for the first time from 3300 to 4600°K.

UNCLASSIFIED

SECURITY CLASSIFICATION OF THIS PAGE(When Data Entered)

PREFACE

This work was supported by the Office of Naval Research under Air Force/Space Division Contract No. F04701-80-C-0081. The authors wish to thank contract monitor Dr. L. H. Peebles for his enthusiastic support and pertinent suggestions. The significant contributions of Dr. A. G. Whittaker and Mr. P. L. Kintner in obtaining the CW laser data are gratefully acknowledged. Efficient and timely computer programming was provided by Dr. W. M. Adams. The authors wish to especially thank Dr. G. M. Rosenblatt for his contributions to the experiment planning and data analysis.

1

Accession For	
NTIS GRA&I	
DTIC TAB	
Unannounced	
Justification	
FV	
Distribution	
Availability	
Dist	SP
A	



CONTENTS

PREFACE	1
I. INTRODUCTION	7
II. SUPPORTING ANALYSES	11
A. Nonlinear Knudsen Layer Model	11
1. Model Description	11
2. Baseline Calculated Results	15
3. Sensitivity Studies	17
a. Closure Assumption for Conservation Equations	17
b. Chemical Species Equilibrium in the Knudsen Layer	21
c. Frozen Internal Energy States in the Knudsen Layer	21
d. Surface Adsorbed Layer Kinetics	24
B. Molecular Dynamics Simulations	26
III. DATA INTERPRETATION	29
A. Summary of Approach, Critical Assumptions	29
1. Relationship of Directly Measured Quantities to Desired Thermochemical Properties	29
a. Vaporization Coefficients	29
b. Vapor Pressure	31
c. Melt Temperature	34
2. Critical Assumptions	34
a. Continuous Wave Laser Ablation Data	34
b. Pulsed Laser Ablation Data	35
B. Thermochemical Properties	40
1. Vaporization Coefficients	40
2. Vapor Pressure	47

PRECEDING PAGE BLANK-NOT FILMED

CONTENTS (Continued)

3. Melt Temperature	59
a. Carbon Phase Change Detection Using Surface Reflectance	59
b. Experimental Results and Conclusions	65
III. C. Remaining Questions	73
IV. SUMMARY AND CONCLUSIONS	75
REFERENCES	77
APPENDICES:	
A. DATA SUMMARY	A-1
B. GRAPHNOL DATA INTERPRETATION	B-1
C. INFORMATION AVAILABLE FROM CW VERSUS PULSED LASER DATA	C-1

FIGURES

1. The Knudsen Layer	13
2. Baseline Calculated Results	18
3. Normalized Stagnation Pressure and Mass Loss Ratios	19
4. Closure Assumption Sensitivity	20
5. Sensitivity to Chemical Species Relaxation Rates	22
6. Sensitivity to Internal Energy States Relaxation Rates	23
7. Sensitivity to Adsorbed Layer Kinetics	25
8. Relationship of Experiments to Objectives	30
9. Effect of Ambient Pressure and Thermochemical Data on Mass Loss Rate	33
10. Comparison of CW Laser Data and Predicted Results (Livermore) . .	42
11. Comparison of CW Laser Data and Predicted Results (JANAF)	43
12. Vaporization Coefficients Derived from CW Laser Data	44
13. Comparison of Pulsed Laser Data and Predicted Results (Livermore)	46
14. Comparison of Pulsed Laser Data and Predicted Results (JANAF) . .	47
15. Pulsed Laser Data and Data Line.	48
16. Vaporization Coefficients Derived from Pulsed Laser Data	49
17. Vaporization Coefficients for Livermore Thermochemical Data.	50
18. Vaporization Coefficients for JANAF Thermochemical Data.	51
19. Carbon Total Vapor Pressure.	52
20. Variation of Mass Loss Rate with Surface Temperature and Ambient Pressure	54

FIGURES (Continued)

21.	Comparison of Measured and Predicted Mass Loss Rates, (a) $p_a=0.02$ atm, (b) $p_a=0.05$ atm	55
22.	Comparison of Measured and Predicted Mass Loss Rates, (a) $p_a=0.1$ atm, (b) $p_a=0.2$ atm	56
23.	Comparison of Measured and Predicted Mass Loss Rates, (a) $p_a=0.5$ atm, (b) $p_a=1.0$ atm	57
24.	Bidirectional Reflectivity of Silicon	63
25.	Bidirectional Reflectivity of Pyrolytic Graphite	64
26.	Experimental Apparatus	66
27.	Reflectance Below Melting Temperature	68
28.	Reflectance at Melting Temperature	69
29.	Reflectance of Pyrolytic Graphite	71
A-1.	Free-Jet Peak Total Pressure versus Peak Surface Temperature . .	A-5
A-2.	Derived Free-Jet Total Pressure versus Peak Laser Flux for Vaporization in Argon	A-6
A-3.	Peak Surface Temperature versus Peak Laser Flux for Vaporization in Argon	A-7
A-4.	Comparison of Pyrolytic Graphite and Graphnol Data	A-8
B-1.	Comparison of Low Pressure Pyrolytic Graphite and Graphnol Mass Loss Rate Data	B-3
B-2.	Vaporization Coefficients (Livermore) Derived from Pulsed Laser Data	B-4

TABLES

A-1.	Pyrolytic Graphite Ablation Data	A-2
A-2.	Graphnol Ablation Data	A-3

I. INTRODUCTION

The superior energy dissipating efficiency of carbon materials in ablative thermal protection system applications is well-known. However, in advanced systems applications such as planetary entry, both the solid-vapor interphase mass transport rate and the carbon (graphite) surface temperature may achieve levels considerably higher than in any previous use. Thus, questions concerning energy dissipation efficiency in these new regimes must be addressed if survivable systems are to be designed.

Historically, carbon ablation models have been based on the assumption of equilibrium thermodynamics,^{1,2} i.e., the carbon vapor state at the ablation surface is assumed to be given by equilibrium thermodynamic properties at the surface temperature. At temperatures above 4000°K, the equilibrium total vapor pressure of carbon is presently uncertain, with some literature values^{2,3} being as much as an order of magnitude greater than the JANAF⁴ predicted value. Also, reported melt temperatures range from about 4000 to 4400°K.⁵ When melting occurs, the ablation efficiency may decrease by as much as a factor of three if the liquid carbon is stripped away without vaporizing. Thus, even from the perspective of an equilibrium ablation model, carbon ablation efficiencies above 4000°K cannot at the present time be predicted with desired accuracy.

¹Dolton, T. A., H. E. Goldstein, and R. E. Mauer, "Thermodynamic Performance of Carbon in Hyperthermal Environments," Progress in Astronautics and Aeronautics: Thermal Design Principles of Spacecraft and Entry Bodies, Vol. 21, Ed. J. T. Bevans, Academic Press, NY, 1969, pp 169-201.

²Baker, R. L., "Graphite Sublimation Chemistry Nonequilibrium Effects," AIAA Journal, Vol. 15, Oct. 1977, pp. 1391-1397.

³Kratsch, K. M., et al., "Graphite Ablation in High Pressure Environments," AIAA Paper 68-1153, 1968.

⁴JANAF Thermochemical Tables, National Bureau of Standards, NBS-37, June 1971.

⁵Baker, R. L. and P. G. Crowell, "Graphite Material Ablation Performance in High Thermal Radiation Environments," Progress in Astronautics and Aeronautics: Entry Heating and Thermal Protection, Vol. 69, Ed. W. Oistad, AIAA, NY, 1980, pp. 198-221.

This picture is further complicated by the multi-species character of the carbon vapor state⁶ and the nonequilibrium nature of carbon ablation in advanced applications.^{2,5,7} To encompass these features, an ablation model must express the interphase mass transport rate in terms of the vaporization kinetics of each carbon species.

In such a nonequilibrium model, these rates are given in terms of the species vaporization coefficients. Carbon species vaporization coefficients have been experimentally determined only at the relatively low temperature of 2700°K.^{6,8} There is apparently no published information concerning their temperature dependence.

In summary, the primary thermochemical properties required in order to accurately predict expected carbon mass loss rates per unit input of energy are the vapor pressure, the melt temperature, and the kinetic rates associated with a nonequilibrium phase change. The current uncertainty or nonexistence of values for these properties at operating temperatures above 4000°K provided the motivation for the work reported herein. The principal objectives were to determine the above properties through a combined experimental and analytical effort.

The vapor pressure and vaporization coefficient determination techniques used in this work represent a significant departure from standard high temperature methods,^{6,9} i.e., Knudsen cells and free vaporization experiments. The present method is based upon correlating experimental carbon laser ablation data with an analytical model of the nonequilibrium phase change

⁶Palmer, H. B. and M. Shelef, "Vaporization of Carbon," Chemistry and Physics of Carbon, Vol. 4, Ed. P. L. Walker, Jr., Marcel Dekker, Inc., NY, 1968.

⁷Baker, R. L., "An Irreversible Thermodynamics Model for Graphite Sublimation in Radiation Environments," Progress in Astronautics and Aeronautics: Outer Planet Heating and Thermal Protection Systems, Vol. 64, Ed. R. Viskanta, AIAA, NY, 1979, pp. 210-227.

⁸Zavitsanos, P. D., "The Vaporization of Pyrolytic Graphite," General Electric Co., GE R 66SD31, May 1966.

process. The biggest advantage of this new approach is that it allows the upper temperature limit of the carbon data to be extended from the normal 2700°K up to 4600°K. A unique approach for the determination of carbon melting, based on detecting changes in surface reflectivity, has also been used.

Experimental carbon ablation data have been obtained over a wide range of surface temperature (3300 to 4600°K) by employing a continuous wave laser for data at the lower end of this temperature range and a pulsed laser for achieving higher temperatures. A nonlinear analytical model describing the nonequilibrium gas dynamics and chemical rate processes that occur when carbon is rapidly vaporized has also been developed¹⁰ as an extension of earlier work with linearized models.^{2,5,7} This report discusses comparison of model predictions with the experimental data and conclusions from this regarding the desired high temperature thermochemical properties of carbon.

The supporting analytical work is described in Section II, followed by a discussion of data interpretation in Section III. Conclusions are summarized in Section IV.

⁹Margrave, J. L., Ed. The Characterization of High-Temperature Vapors, John Wiley & Sons, NY, 1967.

¹⁰Baker, R. L., "Carbon Nonequilibrium Phase Change," Office of Naval Research Interim Report, TR-0081(6728-02)-1, The Aerospace Corporation, El Segundo, CA, December 1981.

II. SUPPORTING ANALYSES

In order to obtain the desired thermochemical properties from the experimental carbon laser ablation data, an analytical description of the non-equilibrium gas dynamics and chemical kinetics of the phase change process is needed. The nonlinear Knudsen layer model which we have developed from this purpose has been described in Ref. 10. In Subsection II-A below, the model is briefly reviewed and recent improvements to it are described. Following this, baseline model predictions and the sensitivity of calculated results to model parameters are discussed. In Subsection II-B, complementary analytical work in progress through a joint effort with the University of Texas at Austin is described.

A. NONLINEAR KNUDSEN LAYER MODEL

1. Model Description

As shown schematically in Fig. 1a, the Knudsen layer is a thin region (the order of a few mean free paths in thickness) immediately above the rapidly subliming or vaporizing carbon surface. In this region, nonequilibrium gas dynamic and chemical rate processes occur which determine the carbon vapor state as it is transported away from the ablating surface. Macroscopic measurements of pressure p , density ρ , temperature T , and convective velocity u can only be made in the continuum gas dynamics region above the Knudsen layer edge. A Knudsen layer model provides the relationships between these measurable variables and the equilibrium (saturation, subscript s) thermodynamic properties of the carbon vapor at the solid or liquid surface.

The modeling approach we have used represents an extension of the method first described by Anisimov.¹¹ It is based upon equations for the

¹¹Anisimov, S. I., "Vaporization of Metal Absorbing Laser Radiation," Soviet Physics (JETP), Vol. 27, No. 1, 1968, pp. 182-183.

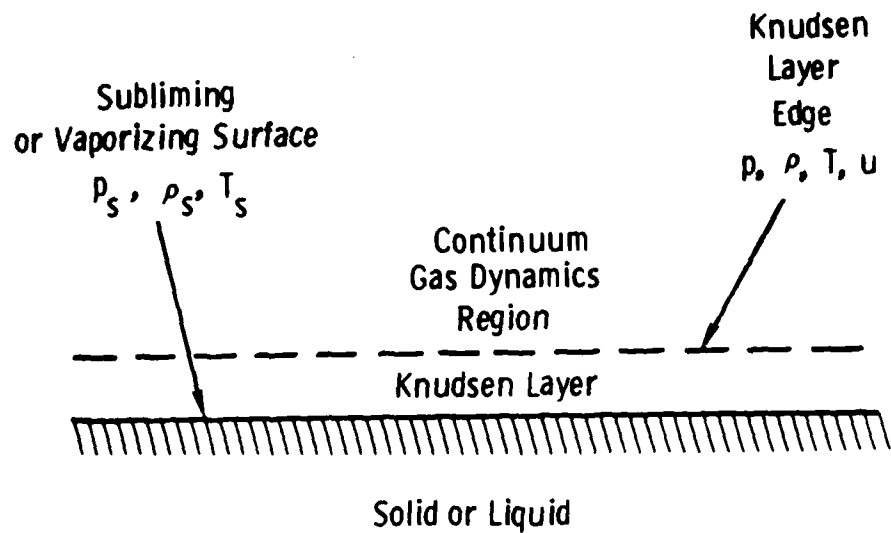
conservation of mass, momentum, and energy across the Knudsen layer. This is shown schematically in Fig. 1b, where J may be thought of as a flux of mass, momentum, or energy. At the edge of the Knudsen layer, the fluxes are represented by their well-known expressions from continuum gas dynamics. At the surface, $\alpha_v J_s$ represents directional fluxes away from the surface due to a change of phase from the solid, and J_b represents incoming directional fluxes caused by backscattering of molecules during collision processes within the Knudsen layer. A fraction of J_b , $\alpha_c J_b$, is condensed while the remaining fraction $(1 - \alpha_c) J_b$ is reflected. The quantities α_v and α_c are the vaporization and condensation coefficients, respectively.

Following Anisimov and Bird,¹² the mass, momentum and energy conservation equations across the Knudsen layer for carbon species C_i , $i=1, 2, \dots, n$, may be written

$$[\rho_i u_i]_J = \left[\alpha_{v_i} \rho_{s_i} \sqrt{\frac{RT_s}{2\pi\mu_i}} \right]_{J_s} + \left[\alpha_{c_i} \bar{\rho}_{b_i} T_b^{1/2} \rho_i \sqrt{\frac{RT}{2\pi\mu_i}} f^1(x_i) \right]_{J_b} \quad (i = 1, 2, \dots, n) \quad (1)$$

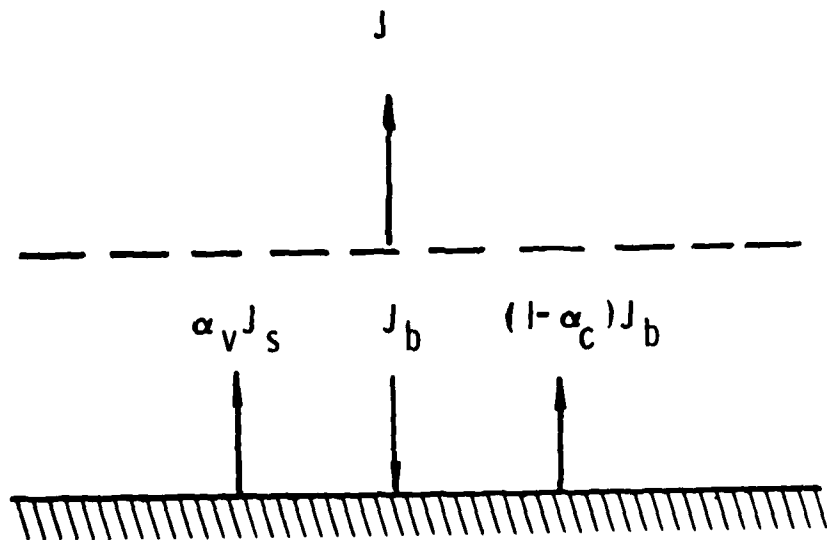
$$\begin{aligned} \left[\rho \left(u^2 + \frac{RT}{\mu} \right) \right]_J &= \left[\frac{RT_s}{2} \sum_{i=1}^n \frac{\alpha_{v_i} \rho_{s_i}}{\mu_i} \right]_{J_s} \\ &+ \left[T_b RT \sum_{i=1}^n \rho_{b_i} (2 - \alpha_{c_i}) \frac{\rho_i}{\mu_i} f^2(x_i) \right]_{J_b} \end{aligned} \quad (2)$$

¹²Bird, G. A., Molecular Gas Dynamics, Oxford University Press, London, 1976.



(a)

(a) Intensive Property Changes Across Knudsen Layer



(b)

(b) Balance of Fluxes Across Knudsen Layer

Fig. 1. The Knudsen Layer

$$\left[\rho u \left(\left[\frac{5}{2} + G \right] \frac{RT}{M} + \frac{1}{2} u^2 \right) \right]_s = \left[\frac{(RT_s)^{3/2}}{(2\pi)^{1/2}} \sum_{i=1}^n \frac{\alpha_{v_i} \rho_{s_i}}{M_i^{3/2}} (2+G_i) \right]_{J_s} + \left[T_b^{3/2} \frac{(RT)^{3/2}}{(2\pi)^{1/2}} \sum_{i=1}^n \frac{\alpha_{c_i} \bar{\rho}_b \rho_i}{M_i^{3/2}} \left\{ f^3(x_i) + f^1(x_i) G_i \right\} \right]_{J_b} \quad (3)$$

The functions $f(x_i)$ are given by

$$f^1(x_i) = \pi^{1/2} x_i \operatorname{erfc}(x_i) - e^{-x_i^2} \quad (4a)$$

$$f^2(x_i) = \left(x_i^2 + \frac{1}{2} \right) \operatorname{erfc}(x_i) - \frac{x_i}{\pi^{1/2}} e^{-x_i^2} \quad (4b)$$

$$f^3(x_i) = x_i \left(x_i^2 + \frac{5}{2} \right) \pi^{1/2} \operatorname{erfc}(x_i) - \left(x_i^2 + 2 \right) e^{-x_i^2} \quad (4c)$$

where

$$x_i = \bar{w}_i T_b \frac{u_i}{\sqrt{2RT/M_i}} \quad (4d)$$

Quantities not yet defined in the above equations are the molecular weight M , the convective velocity w of the backscattered molecules striking the surface, and G which is related to the ratio of specific heats γ by

$$G(\gamma) = \frac{(5 - 3\gamma)}{2(\gamma - 1)} \quad (5)$$

The quantities in Eqs. (1) through (4) are dimensional except for x_i , \bar{T}_b , and \bar{w} . The latter two variables are nondimensionalized by T and u , respectively, and x_i is directly proportional to a species Mach number M_i , i.e.

$$\bar{T}_b = T_b/T \quad (6a)$$

$$\bar{w} = w/u \quad (6b)$$

$$x_i = \sqrt{\gamma_i/2} \bar{w}_i \bar{T}_b M_i \quad (6c)$$

When it is assumed that $T_b = T$ and $w = u$, then $\bar{T}_b = \bar{w} = 1$ and the above equations reduce to those described in Ref. 10. The three conservation equations do not allow one to solve for T_b and w . An ad hoc assumption must be made in order to solve for the other quantities. Anisimov assumed $\bar{T}_b = \bar{w} = 1$. If the equations are written as above, these quantities may be parametrically varied over their entire allowable range, i.e.

$$1 \leq \bar{T}_b \leq T_s/T, \quad 0 \leq \bar{w} \leq 1 \quad (7)$$

In this way, the sensitivity of the calculated results to the ad hoc closure assumption can be assessed.

2. Baseline Calculated Results

In all of the calculations in this report, it has been assumed that $\alpha_c = \alpha_v = \alpha$. Thus, from this point on the subscripts c and v will be dropped. Additional assumptions must be made before the coupled nonlinear

equations (1) through (3) can be solved. These assumptions are summarized below:

	<u>Baseline</u>	<u>Sensitivity Study</u>
Closure assumption for conservation equations	$T_b = \bar{w} = 1$	$1 \leq T_b \leq \frac{T_s}{T}, 0 \leq \bar{w} \leq 1$
Knudsen layer chemical species relaxation	Frozen	Equilibrium
Knudsen layer internal energy states relaxation	Equilibrium	Frozen
Species vaporization coefficients (adsorbed layer kinetics)	Frozen	Equilibrium

The baseline assumptions are supported by the relatively large number of molecular collisions (thousands) required for species relaxation, the small (5 to 10) number of molecular collisions required for rotational energy states to relax, and the short residence time in the surface adsorbed layer for molecules passing from the solid to the continuum vapor when the surface temperature is 3000°K or greater.¹³ When the kinetic processes in the adsorbed layer are frozen, the species vaporization coefficients are assumed to be given by

$$\alpha_i = \alpha \quad (8a)$$

and when these processes are in equilibrium, it can be shown^{13,14} that

$$\alpha_i = (\alpha_1)^i \quad (8b)$$

¹³Rosenblatt, G. M., Personal Communication, Pennsylvania State University, Department of Chemistry, University Park, PA.

¹⁴Kleinschmidt, P. D. and G. M. Rosenblatt, "Relative Vaporization Rates of As₂(g) and As₄(g) from an Arsenic (111) Surface," American Society of Mass Spectrometry Meeting, June 1977.

Baseline calculated results are shown in Fig. 2. The ratio of quantities across the Knudsen layer (see Fig. 1a) is presented as a function of the Mach number $M = u / \sqrt{\gamma RT/M}$ at the Knudsen layer edge. The parameter variation with α is also shown. From this figure, the values of p/p_s for a Mach number of 1, i.e., p^*/p_s , can be obtained. The ratio of stagnation pressure p_0 to p_s can then be determined, since for $M = 1$

$$\frac{p_0}{p^*} = \left(\frac{\gamma + 1}{2} \right)^{\frac{\gamma}{\gamma - 1}} , \quad \frac{p_0}{p_s} = \frac{p^*}{p_s} \frac{p_0}{p^*} \quad (9)$$

Thus, the desired relationships between quantities measured in the laser ablation experiments, i.e., the mass loss rate $\dot{m} = \rho u$, p_0 , and T_s , and the vapor pressure p_s and vaporization coefficient α have been established. The rather weak nonlinear dependence of p_0/p_s and \dot{m}^*/\dot{m} on α can be seen by renormalizing and plotting these quantities as shown in Fig. 3. Note that \dot{m}^* is the value \dot{m} when the Knudsen layer edge Mach number M is 1 and $\dot{m}_s = \rho_s \sqrt{RT_s / 2\pi\mu}$. Thus, Fig. 3 represents calculated solutions of Eqs. (1) through (3) as a function of α for the case $M = 1$.

Predicted results such as those shown in Fig. 3 can be used directly to obtain vaporization coefficients from the experimental data. The method is described further in Subsection III-B-1. Similarly, predicted results, such as those presented in Fig. 2, can be used to obtain vapor pressure p_s from experimental data as described in Subsection III-B-2 and Ref. 10.

3. Sensitivity Studies

a. Closure Assumption for Conservation Equations

The sensitivity of calculated results, for the primary quantities of direct interest p/p_s and \dot{m}/\dot{m}_s , to the closure assumption $T_b = \bar{w} = 1$ is shown in Fig. 4. Both T_b and \bar{w} were systematically changed over their entire range

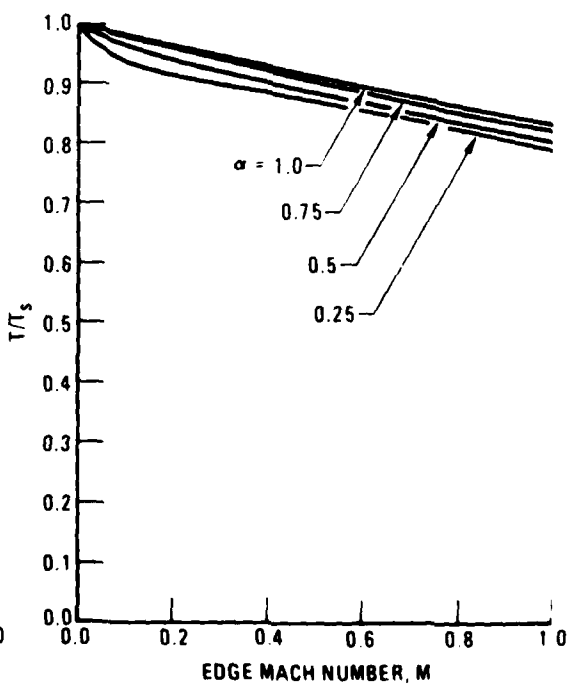
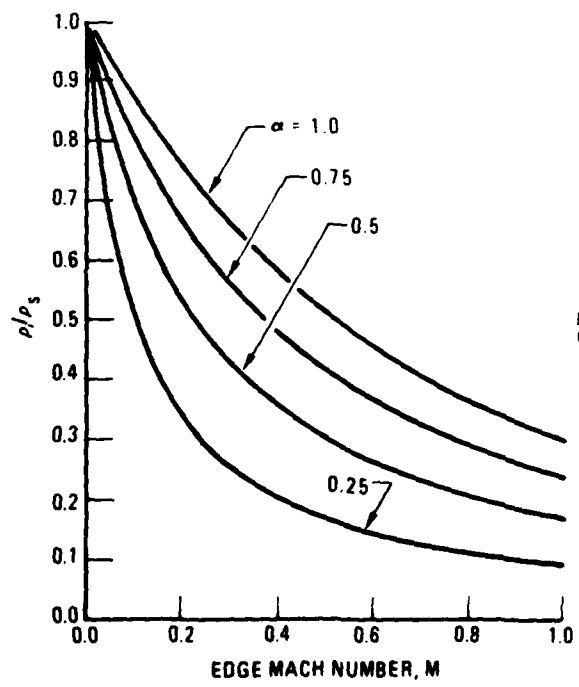
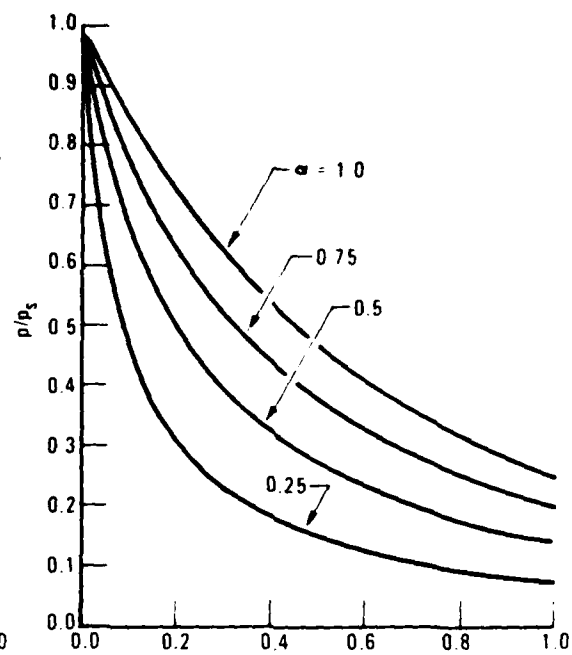
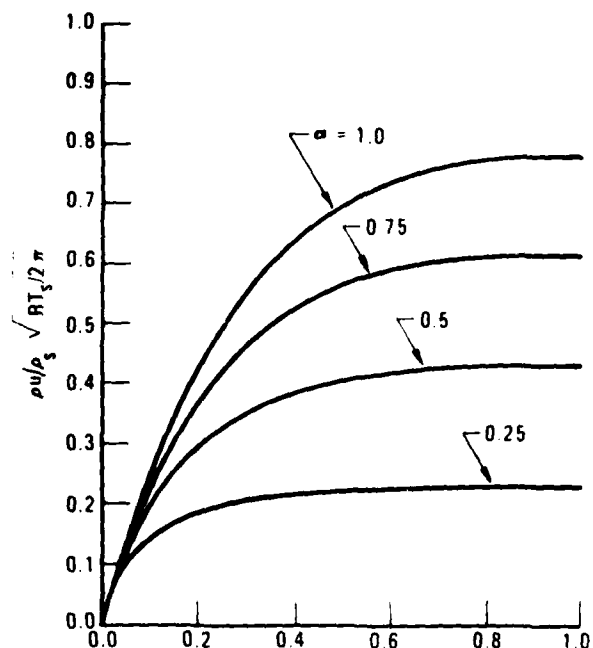


Fig. 2. Baseline Calculated Results

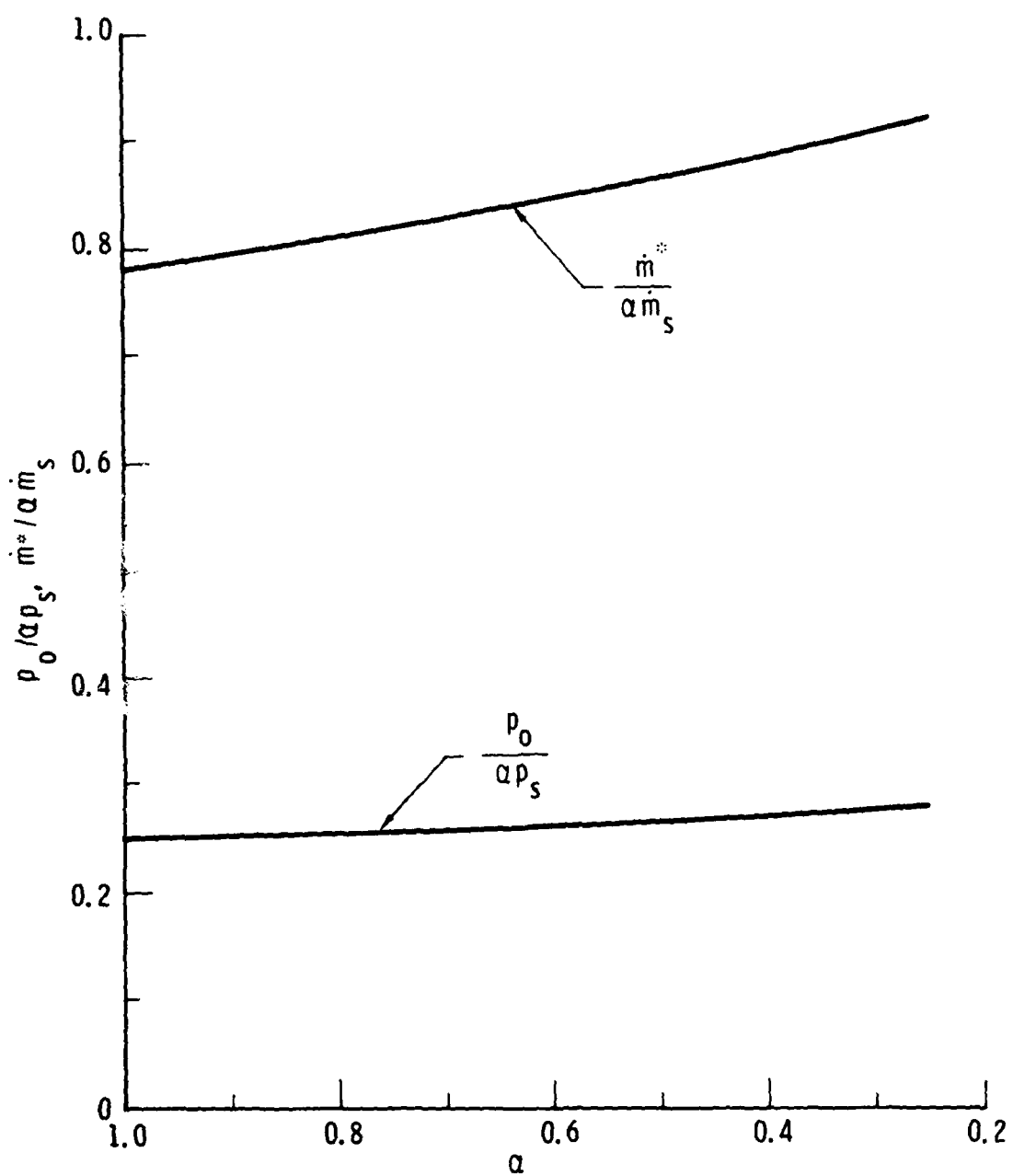


Fig. 3. Normalized Stagnation Pressure and Mass Loss Ratios

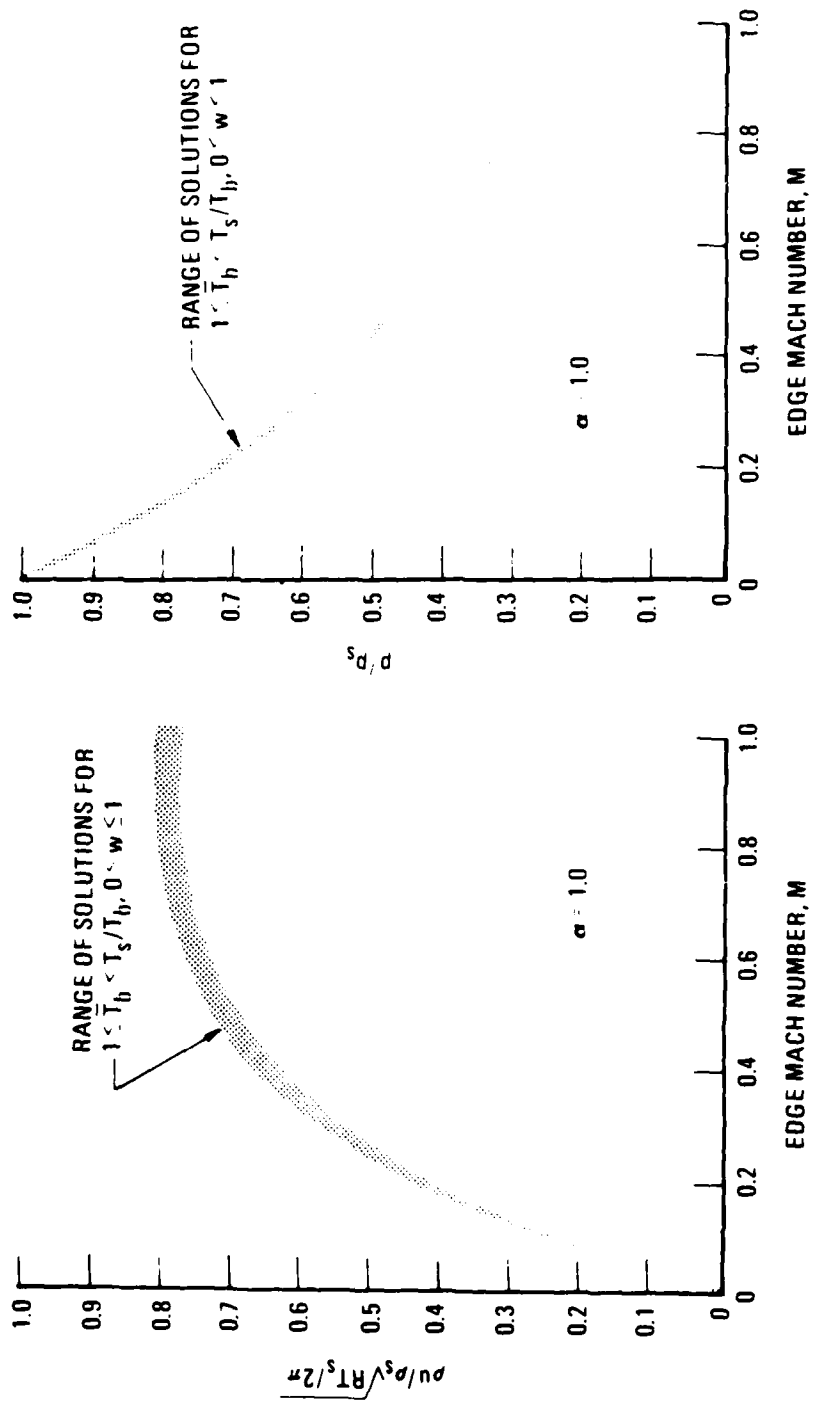


Fig. 4. Closure Assumption Sensitivity

of possible values, i.e., Eq. (7). As noted, p/p_s is extremely insensitive to the closure assumption. The other variable \dot{m}^*/\dot{m}_s increases by a maximum of 5 percent when it is assumed that $\bar{w} = 0$ and $T_b = T_s/T$. Physically, assuming $\bar{w} = 0$ would not appear to be realistic when the Mach number is large. Thus, especially for $M = 1$, the baseline calculated results for \dot{m}^*/\dot{m}_s should be very close to the correct value.

b. Chemical Species Equilibrium in the Knudsen Layer

If the carbon species concentrations in the Knudsen layer are assumed to be in chemical equilibrium rather than frozen at their saturation condition values, as in the baseline calculations, the predicted results change as shown in Fig. 5. The primary quantities of interest, p/p_s and (\dot{m}/\dot{m}_s) as well as ρ/ρ_s , are relatively insensitive to the rate of chemical relaxation processes in the Knudsen layer. The temperature, however, is more sensitive to this assumption, since equilibration involves changes in individual species concentrations with relatively large net energy release.

c. Frozen Internal Energy States in the Knudsen Layer

The baseline calculations assume that the internal energy states of the polyatomic carbon species are in equilibrium throughout the Knudsen layer. If, instead of this, the energy in these states is frozen at the saturation temperature T_s value, then much less energy is available to be transferred to translational and directed (convective) velocity states. As a consequence, when these states are frozen the temperature at the edge of the Knudsen layer is considerably reduced.

This effect and the effects on \dot{m} , p , and ρ are seen in Fig. 6. For a Knudsen layer edge Mach number of 1, both the temperature and pressure ratios are decreased 20 percent, the mass loss ratio increases 3 percent, and the density remains virtually the same. This is the largest effect seen thus far in the sensitivity studies, and must be kept in mind when the comparisons of experimental data with predictions are made.

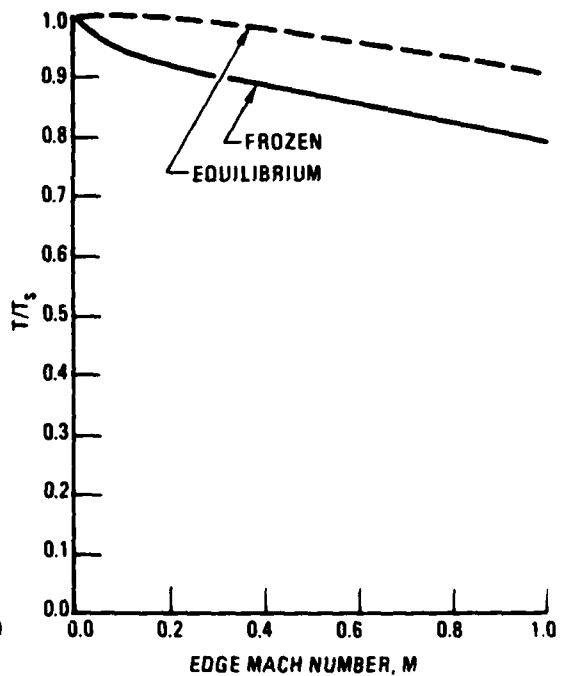
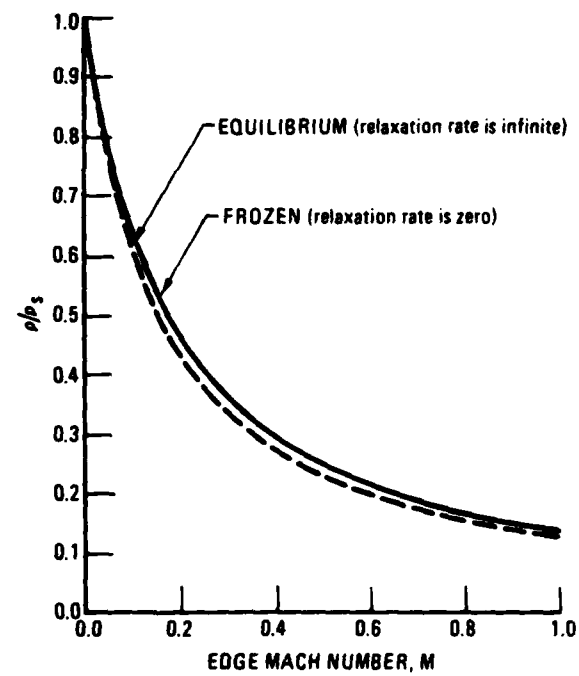
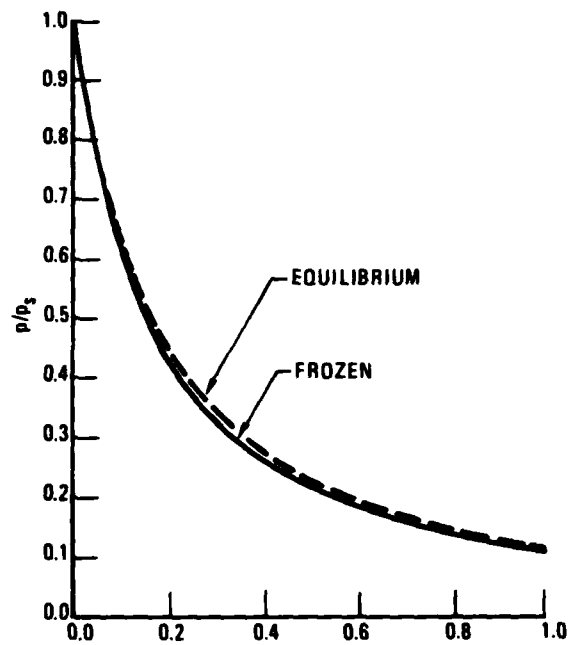
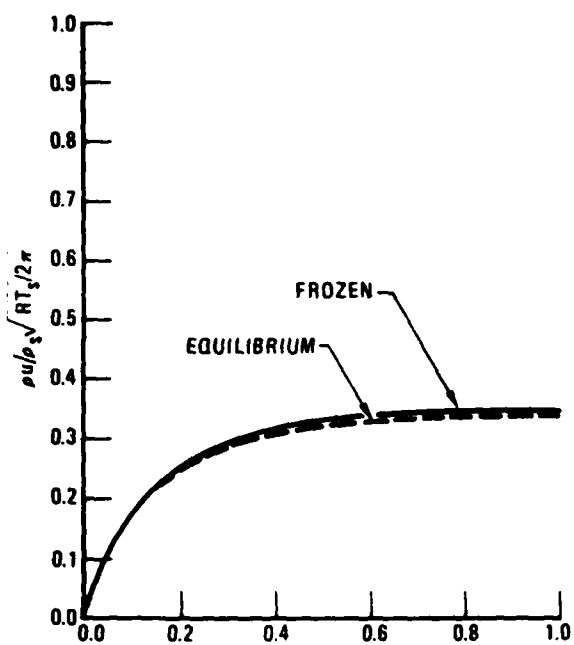


Fig. 5. Sensitivity to Chemical Species Relaxation Rates

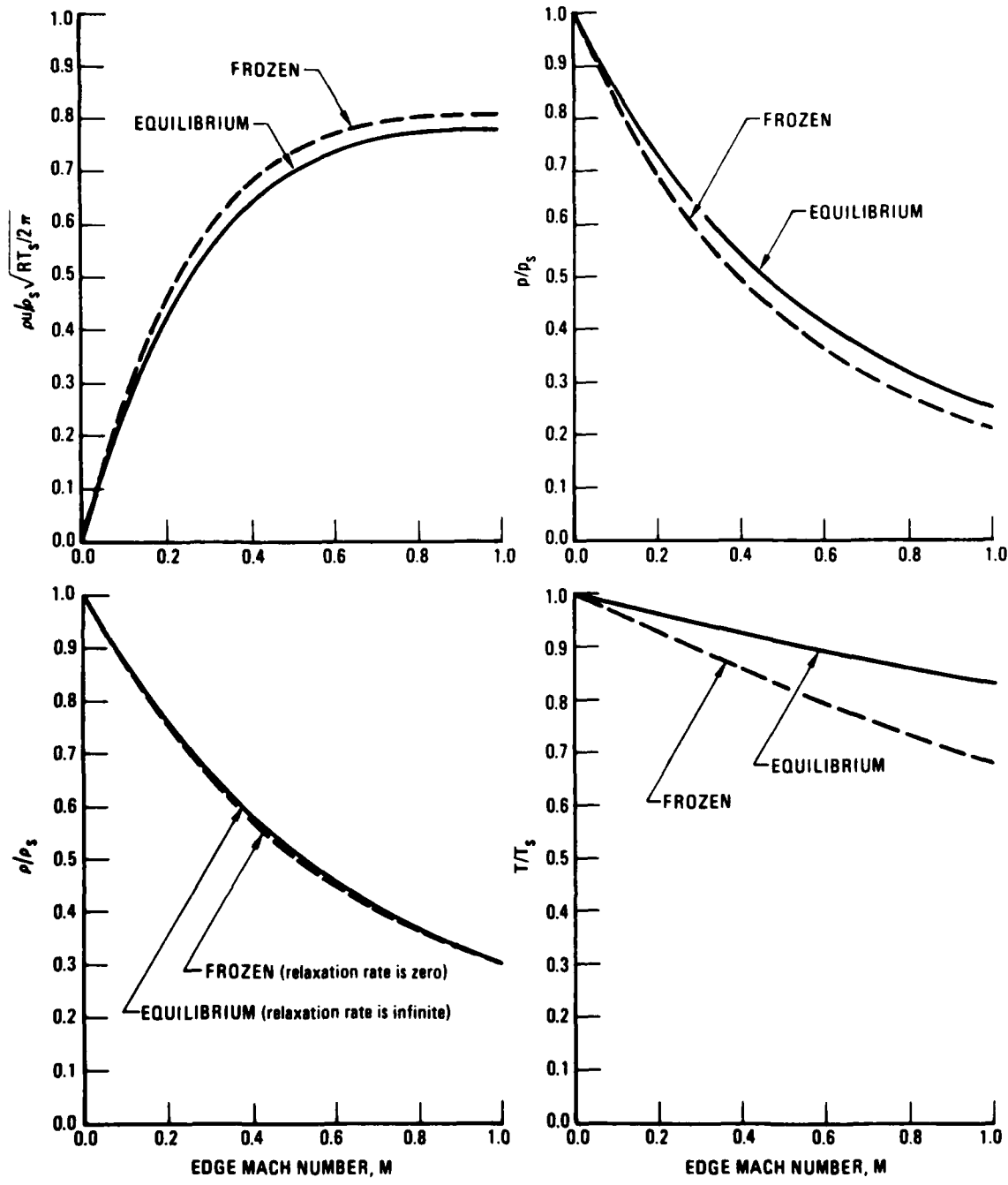


Fig. 6. Sensitivity to Internal Energy States Relaxation Rates

Most of the carbon vapor is made up of C_3 molecules.⁶ Therefore, the relaxation of internal energy states across the Knudsen layer is likely to be somewhere between frozen and equilibrium. That is, the internal energy of the C_3 molecule at moderate temperature ($< 4500^{\circ}\text{K}$) is distributed mainly between rotational and vibrational modes. Since the rotational energy states equilibrate (relax) rapidly within a few molecular collisions, they are likely to be in equilibrium. In contrast to this, the vibrational energy states equilibrate (relax) slowly requiring thousands of molecular collisions. Thus, they are likely to remain nearly frozen.

d. Surface Adsorbed Layer Kinetics

The baseline calculations assume $\alpha_i \equiv \alpha$, i.e., all of the species vaporization coefficients are equal to one another. If, instead of this, the individual species remain in the adsorbed layer on the surface long enough for chemical equilibrium to be established within the layer, then the α_i will not be equal but rather related to α_1 through Eq. (8b). The sensitivity of calculated results to the carbon species vaporization coefficients is shown in Fig. 7.

Results are shown for Cases A, B, and C with species vaporization coefficients as given below:

Case	α_1	α_3	α_i
A (baseline)	0.39	0.39	$\alpha_i = \alpha_1$
B	0.73	0.39	$\alpha_i = (\alpha_1)^{1/3}$
C	1.0	0.39	$\alpha_{i,i \neq 3} = 1.0$

Even with the extreme (unphysical) assumption C, the calculated results differ very little from the baseline results (A). This indicates the dominant importance of α_3 .

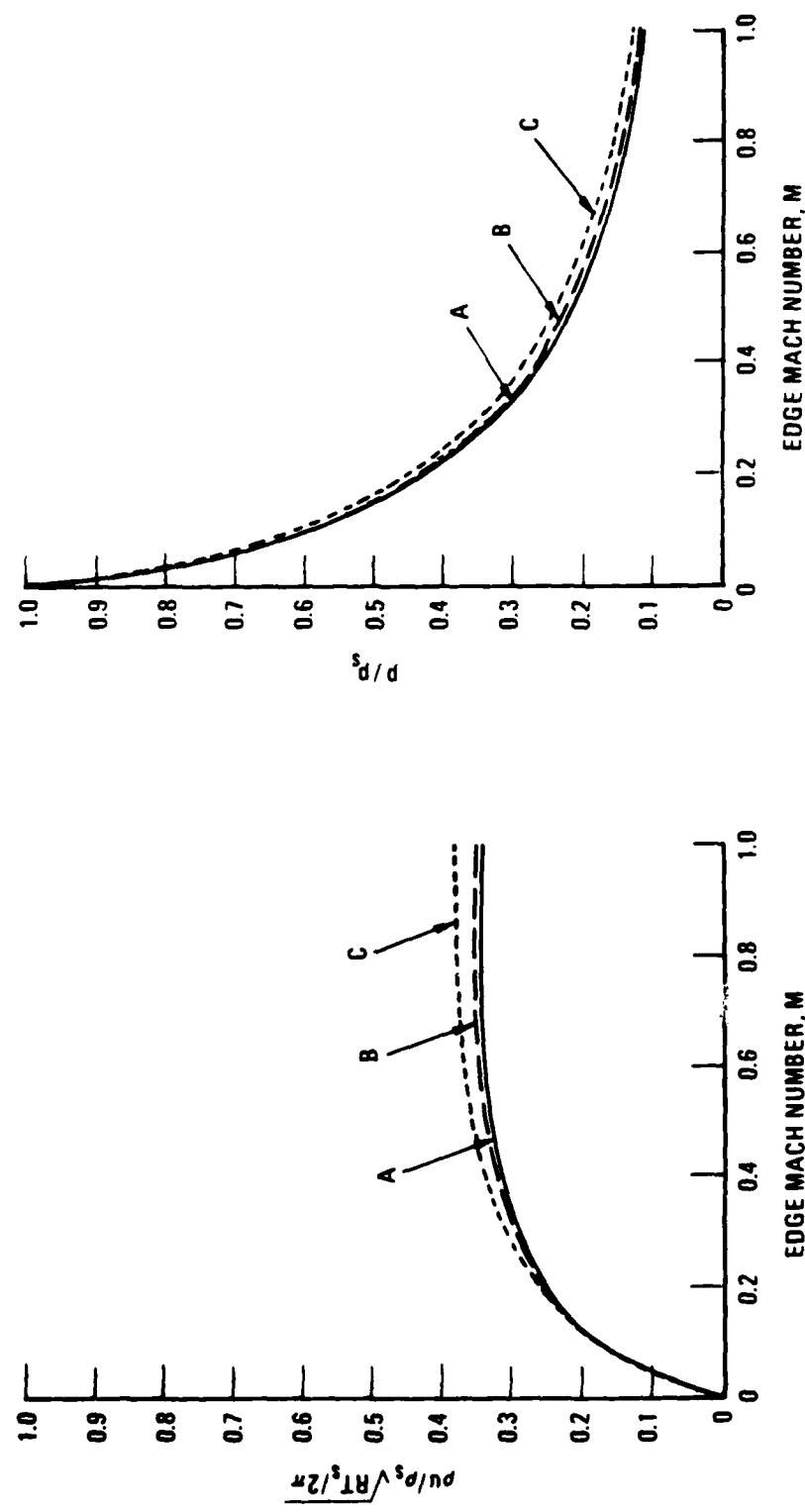


Fig. 7. Sensitivity to Adsorbed Kinetics
(For case definitions, see text)

B. MOLECULAR DYNAMICS SIMULATIONS

The ad hoc manner in which the mass, momentum, and energy conservation equations discussed in Subsection II-A must be closed fortunately does not lead to great uncertainty in the primary calculated variables of interest. However, the conservation equation approach is, effectively, only able to consider limiting cases of frozen or equilibrium chemical reaction rates for adsorbed layer, internal energy states, and carbon species relaxation processes. The sensitivity studies indicate that model predictions for use in the determination of carbon total vapor pressure and vaporization coefficients are also not critically dependent upon the rate of these relaxation processes. Therefore, for the principal objectives of this work, a model based upon the conservation equation approach appears to be adequate.

If a Knudsen layer model capable of including the effects of the above finite rate relaxation processes were available, it should be possible to determine these rates experimentally by comparing data with model predictions. In this way, a Knudsen layer can be considered a tool for chemical kinetics studies in a manner analogous to the well-known use of shock waves for such studies.¹⁵ The differences in these approaches are appealing from an instrumentation point of view. Whereas with a shock wave the kinetic processes are relaxing to a higher energy state (temperature), in a Knudsen layer, they are relaxing to a lower energy state thus aiding the early time (initial) detection accuracy.

¹⁵Resler, E. L., "The Shock Tube and Chemical Kinetics," Fluid Dynamics and Applied Mechanics, Ed. Diaz and Pai, 1961, pp. 125-145.

A multi-species chemically reacting Knudsen layer model is presently being developed through a collaborative effort with the University of Texas at Austin. The model is based upon reactive molecular dynamics simulation algorithms^{16,17} which have previously been applied to complex problems of non-equilibrium chemistry. Such a model seeks to retain all essential features of physical and chemical reality. A report on this work will be written separately.

¹⁶Turner, J. S., "Discrete Simulation Methods for Chemical Kinetics," Journal of Physical Chemistry, Vol. 81, 1977, pp. 2379-2408.

¹⁷Turner, J. S., "From Microphysics to Macrochemistry via Discrete Simulations," Computer Modeling of Matter, ACS Symposium Series No. 86, American Chemical Society, Washington, D.C., Ed. P. Lykos, pp. 231-264.

III. DATA INTERPRETATION

A. SUMMARY OF APPROACH, CRITICAL ASSUMPTIONS

1. Relationship of Directly Measured Quantities to Desired Thermochemical Properties

The way in which the continuous wave (CW) laser and the pulsed laser carbon ablation experiments are related to overall program objectives is shown schematically in Fig. 8. Whereas both sets of experimental data supply vaporization coefficient information, carbon vapor pressure values can only be derived from the CW laser data. The reason for this limitation of information available from the data is discussed in Appendix C. Only the pulsed laser data reach temperatures sufficiently high to potentially supply carbon melting data.

a. Vaporization Coefficients

The present method of obtaining vaporization coefficients from the laser ablation data is closely related to the classical Langmuir Method. The Langmuir vapor pressure p_L is the product of the vaporization coefficient and the equilibrium vapor pressure p_s of the saturated vapor at temperature T_s . Classically, these quantities are related to the vaporization rate \dot{m} and the molecular weight M by the Langmuir relation

$$p_L = \alpha p_s = \dot{m} \sqrt{\frac{2\pi RT_s}{M}} \quad (10)$$

The Langmuir method is carried out by vaporizing material into a vacuum. The analysis discussed in Subsection II-A indicates that when vaporization takes place into a finite back pressure environment, but the equilibrium vapor pressure p_s is sufficiently greater than the ambient pressure p_a ,

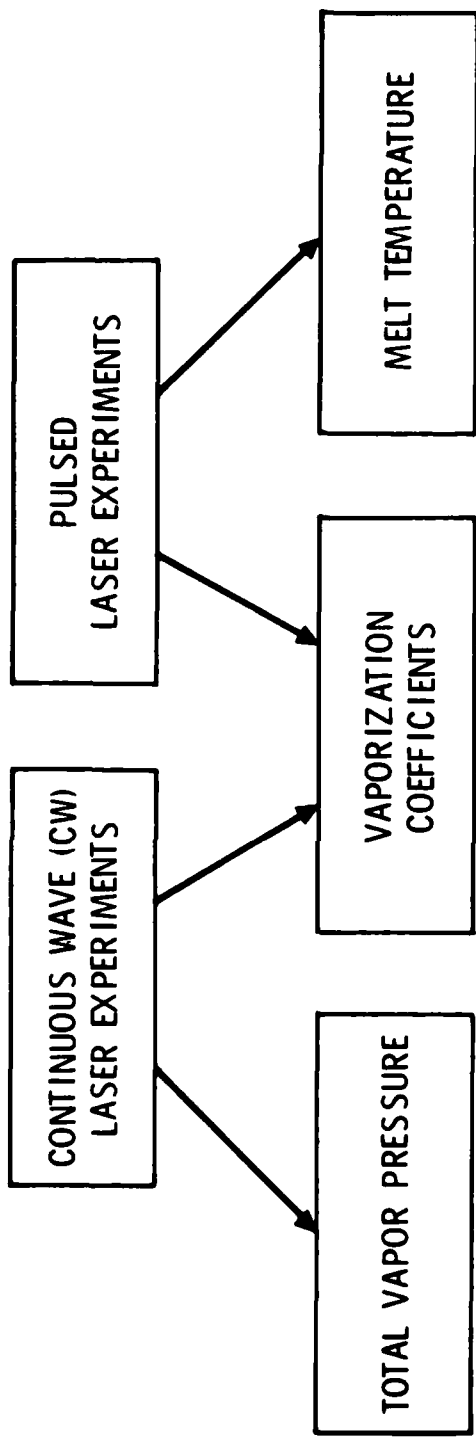


Fig. 8. Relationship of Experiments to Objectives

the Langmuir pressure and the vaporization (mass loss) rate \dot{m} are related by

$$p_L = \alpha p_s = F_1(\alpha, \gamma) \dot{m} \sqrt{\frac{2\pi RT_s}{M}} \quad (11)$$

where $F_1(\alpha, \gamma)$ is a nonlinear function of vaporization coefficient α and also depends on the ratio of specific heats γ .

Thus, if Eq. (11) is used instead of the Langmuir relation, Eq. (10), measured mass loss rate \dot{m} data can be converted to Langmuir pressures. Then for a given vapor pressure relationship which supplies p_s as a function of temperature T_s , $\alpha(T_s)$ can be determined. Because the function $F_1(\alpha, \gamma)$ is nonlinear, the conversion of \dot{m} to α is best accomplished by carrying out the iteration graphically. This is illustrated in Subsection III-B. For the NASA pulsed laser experiments, the Langmuir pressure p_L is similarly related to the measured free-jet stagnation pressure p_0 , i.e.

$$p_L = F_2(\alpha, \gamma)p_0 \quad (12)$$

It should be emphasized that the values of vaporization coefficient as a function of temperature determined in this manner depend on the equilibrium vapor pressure, i.e., $\alpha = p_L/p_s$. To uniquely determine the vaporization coefficient from p_L , the correct equilibrium vapor pressure relationship must be known as discussed below.

b. Vapor Pressure

Once the Langmuir vapor pressure as a function of T_s is known, vaporization coefficients $\alpha_A(T_s)$ and $\alpha_B(T_s)$ corresponding to literature vapor pressure relationships A and B, respectively, can be determined. The analytical model discussed in Subsection II-A can then be used to predict \dot{m} as a

function of T_s for constant p_a . Calculations of this type for two representative carbon vapor pressure specifications, A and B (not to be confused with Cases A, B, and C of Section II), are shown in Fig. 9 for ambient pressures p_a of 1 atm and 0.1 atm. For a given p_a , the predicted results are asymptotic to Eq. (11) at the upper end of the temperature range, i.e., where $p_s \gg p_a$. Here, both thermochemical data sets A and B, with vaporization coefficients $\alpha_A(T_s)$ and $\alpha_B(T_s)$, respectively, predict the same values of total mass loss rate \dot{M} .

For given p_a , as the temperature T_s is decreased the predicted \dot{M} values for vapor pressure relationships A and B differ. This difference becomes greater as T_s is lowered still more. At the lower range of temperatures for given p_a , \dot{M} varies rapidly with T_s and the predicted results become asymptotic to the linear Knudsen-Langmuir equation

$$\dot{M} = \alpha \sqrt{\frac{K}{2\pi RT_s}} (p_s - p_a) A_{sp} \quad (13)$$

where A_{sp} is the area of the laser irradiated spot.

From Eq. (13), it can easily be seen that the rapid increase of \dot{M} with T_s occurs whenever $p_s(T_s)$ is only slightly greater than p_a . Since vapor pressure relationships A and B predict $p_s = p_a$ at different values of T_s , the predicted differences in \dot{M} versus $1/T_s$ behavior seen in Fig. 9 may be directly attributed to the different values of p_s at a given T_s .

Given measurements of \dot{M} and T_s at a specified value of p_a , comparison of such experimental data with predicted results such as those shown in Fig. 9, allows the proper equilibrium vapor pressure relationship (A or B or some other) to be determined.

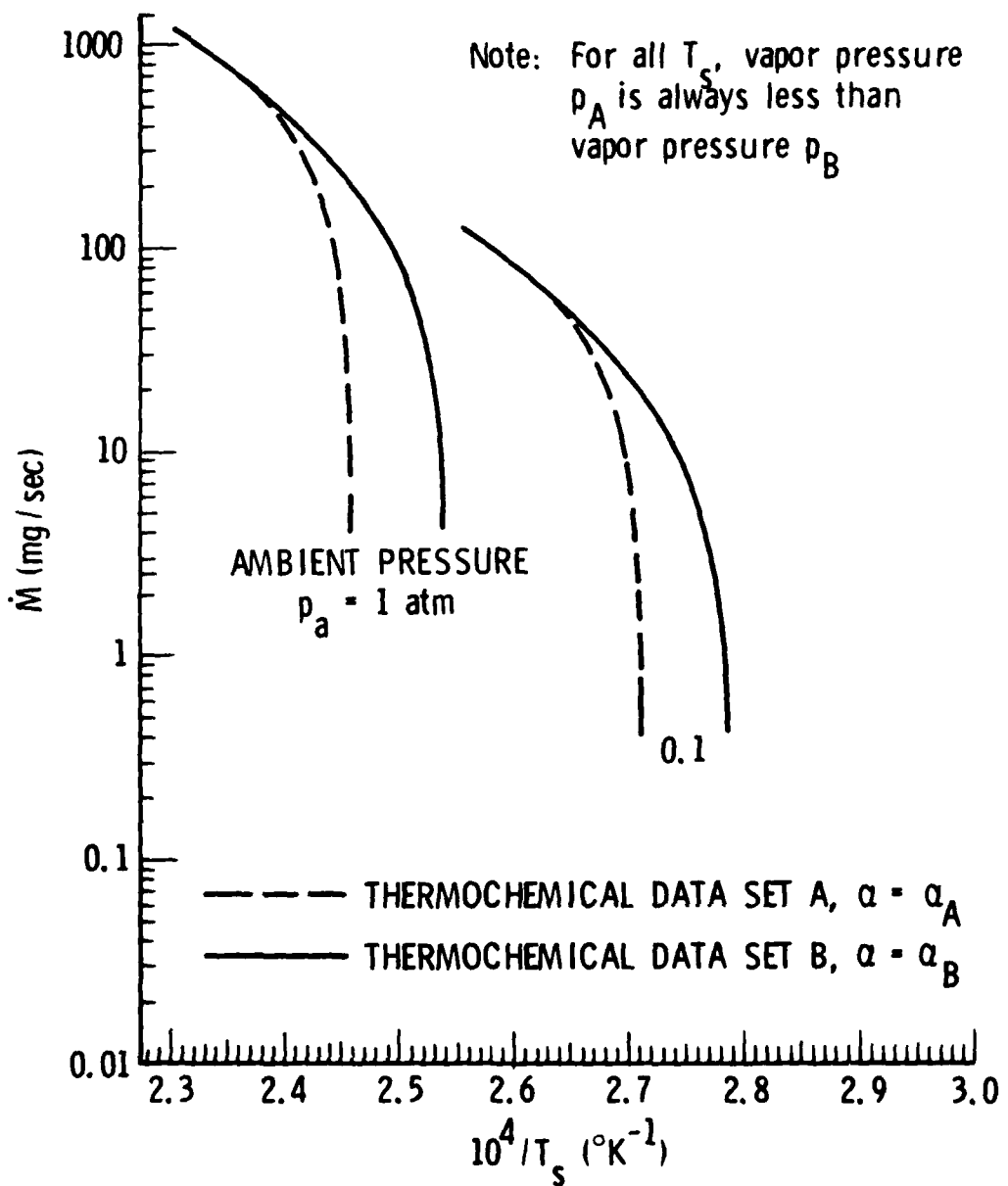


Fig. 9. Effect of Ambient Pressure and Thermochemical Data on Mass Loss Rate

c. Melt Temperature

As originally envisioned in this work, the occurrence of carbon melting was to be related to observed changes in \dot{M} versus $1/T_s$ behavior of the high temperature pulsed laser data. Since the heat of vaporization (liquid-vapor) is always less than the heat of sublimation (solid-vapor), an observed change of slope in the data could possibly be related to the onset of melting.

Subsequently, a more direct approach involving monitoring the surface reflectivity as a function of time during the laser pulse was recommended¹³ and implemented. For the laser annealing of semiconductor materials, this technique has been used very successfully to detect melting by observing the large increase in reflectivity when the semiconductor surface melts.¹⁸ An auxiliary laser is used to monitor the reflectivity.

2. Critical Assumptions

The purpose of the following discussion is to examine some of the key assumptions related to the validity of the data interpretations presented in Subsection III-B.

a. Continuous Wave Laser Ablation Data

For this data set, the directly measured quantities are total mass loss, run time, and surface temperature. The quantities compared to analytical model predictions are the mass loss rate \dot{M} and the saturated vapor temperature T_s which is assumed to be equal to the measured surface temperature.

¹⁸Auston, D. H., et al., "Time Resolved Reflectivity of Ion-Implanted Silicon During Laser Annealing," Applied Physics Letters, Vol. 33, 1978, pp. 437-440.

To obtain the mass loss rate, two key assumptions are made. First, it is assumed that all mass loss takes place by sublimation and, secondly, that the area over which the sublimation takes place is the same as the irradiating laser spot size, even though the sample is rotating. It is difficult to conclusively substantiate these assumptions. The latter assumption is at least qualitatively confirmed by the visually observed carbon vapor plume, i.e., its flow direction is nearly parallel to the axis of the incoming laser beam. The differential time used to convert the total mass loss to a mass loss rate was obtained from the strip chart records of surface temperature. The time increment used in each case was that for which the surface temperature remained within a small fraction, approximately 5 percent of its highest value T_s .

The most critical assumption related to the measured surface temperatures is the assumed emissivity value of unity. For the pyrolytic graphite samples which were irradiated and viewed by the pyrometer in a direction parallel to the a-b plane, this assumption is most defensible.^{19,20} A change of emissivity from 1.0 to 0.9 shifts the measured surface temperatures up $\sim 100^\circ\text{K}$ which would significantly affect the vapor pressure conclusions.

b. Pulsed Laser Ablation Data

For this data set, the stagnation pressure p_0 of the vaporized carbon plume is assumed to be derivable from the measured Mach disk geometry using a simple algebraic relationship.²¹ This relationship is substantiated

¹⁹Pyrolytic Graphite Handbook, Metallurgical Production Dept., General Electric Co., Schenectady, NY, 1964, as quoted in Gokcen, N. A., et al., "Determination of Graphite/Liquid/Vapor Triple Point by Laser Heating," High Temperature Science, Vol. 8, June 1976, pp. 81-97.

²⁰Touloukian, Y. S., Ed., Thermophysical Properties of Matter, Vol. 8, IFI/Plenum Press, NY, 1970.

²¹Covington, M. A., G. N. Liu, and K. A. Lincoln, "Free-jet Expansions from Laser-vaporized Planar Surfaces," AIAA Journal, Vol. 15, August 1977, pp. 1174-1179.

for sonic orifices for a wide range of gases, temperatures, and pressure ratios.²² It is further assumed that the choked carbon vapor flow vaporized from the solid carbon surface subsequently behaves as if emanating from an orifice. The pyrometrically measured surface temperature, as in the CW laser data case, is sensitive to the assumed emissivity.

The relatively steep slope of stagnation pressure p_0 versus $1/T_s$ observed in the pyrolytic graphite vaporization data necessitated considerable reexamination of the methods for determining both p_0 and T_s . This slope was expected to have a numerical value near that of the normalized heat of formation of carbon, i.e., $\Delta H^{\circ}/R \approx 93,000^{\circ}\text{K}$. The slope seen in the data is about $126,000^{\circ}\text{K}$. Possible explanations for this behavior which have been considered are:

- o Emissivity a function of temperature
- o Steady-state energy balance not achieved
- o Significant radial conduction of energy
- o Unsteady surface morphology
- o Condensation of carbon vapor in the free-jet plume
- o Energy release effects in the free-jet plume
- o Strongly temperature-dependent vaporization coefficients

Our conclusions thus far regarding these effects are discussed consecutively below.

If the emissivity changes with temperature, it is likely to increase as temperature increases. It can easily be shown that accounting for such a temperature dependence in the data reduction would increase the slope of the measured data, making it even more difficult to explain.

²²Ashkenas, H. and F. S. Sherman, Rarefied Gas Dynamics, Ed. J. H. de Leeuw, Academic Press, NY, 1966, Vol. 2, p. 84.

The effect of not having achieved a steady-state balance of energy at the ablating surface has been looked at by performing one-dimensional heat conduction calculations. Even at the lowest laser input energy levels, where the time to steady state would be longest, a reasonably quasi-steady Mach disk flow field is established. Thus, non-steady-state energy balance effects do not appear to be influencing the measured data.

For the pulsed laser data, the pyrolytic graphite samples were irradiated parallel to the c-axis. Thus, the high thermal conductivity direction was radially outward from the circular laser spot. To determine if radial conduction of energy was significantly affecting the measured data, additional pyrolytic graphite data were obtained using a new sample configuration to minimize radial conduction. Cylindrical samples were irradiated end-on, with the cylinder diameter approximately equal to the laser spot size. The new data showed no significant differences from the older data for which the laser spot was focussed on a flat planar area much larger than the spot size. Thus, it was concluded that radial conduction of energy was not affecting the data.

As ablation (surface mass removal) is initiated, the surface morphology changes as etch pits are formed and the number of sites at which atoms and molecules are released from the solid increases. When the surface has been completely covered with etch pits, the number of sites releasing atoms/molecules remains fixed, i.e., the surface morphology is at steady state. At the lower levels of laser irradiation, considerably less mass is removed from the sample than at the highest level of energy deposition. If the amount of mass removed is not sufficient to have established a steady-state surface, then increasing numbers of surface vaporization sites with increasing energy deposition could be the cause of the unexpectedly high slope in the data. Based upon estimates of the amount of mass removal required to establish a steady-state surface morphology,^{13,23} it was concluded that a steady surface is likely to be established even at the lowest levels of energy deposition.

The analytical calculations indicate that if the chemical reaction rates, i.e., the carbon species equilibration rates as well as the internal energy-translational energy relaxation rates, are frozen, then the expanding carbon vapor leaving the nonequilibrium region close to the surface (the Knudsen layer) is highly supersaturated. If this vapor subsequently condenses to solid carbon in the free-jet expansion, measured stagnation pressures would be too low. To "explain" the data slope, a physical explanation supporting significant condensation at the lower end of the temperature-stagnation pressure range and little or no condensation at the upper end would be required. It is planned in future experiments to look for the presence of condensed carbon by measuring backscattering of He-Ne laser light from the free-jet plume region.

There are two potentially significant sources of energy release in the expanding carbon vapor free-jet. A frozen vapor at the edge of the Knudsen layer would begin to react and equilibrate carbon species in the free-jet region thereby releasing about 200 cal/mol. Similarly, nonequilibrium between internal and translational energy degrees of freedom at the Knudsen layer edge would also, upon equilibration, release about the same amount of energy. Arguing that this energy is transferred into translational degrees of freedom and thus increases the pressure (and the stagnation pressure), the measured stagnation pressures would be too high whenever significant collisional relaxation takes place. Since collisional relaxation increases with pressure and the measured stagnation pressures are "too high" at larger values of pressure, this effect could explain the data. However, literature data for Mach disk geometries, including energy release effects (relaxation of internal and translational degrees of freedom), shows a very weak dependence on the ratio of specific heats γ .²⁴ This indicates that energy release has little effect on the Mach disk location (geometry).

²³Rosenblatt, G. M., "The Role of Defects in Vaporization: Arsenic and Antimony," Surface Defect Properties of Solids, Vol. 5, 1976, pp. 36-64.

²⁴Wen, Y. S., "Derivation of the Free-Jet Mach-disk Location Using the Entropy-balance Principle," Physics of Fluids, Vol. 18, No. 11, pp. 1421-1425.

If the vaporization coefficient changes rapidly with temperature, the temperature dependence, which is expressed through an activation energy ΔH^* , is represented by²⁵

$$\ln \alpha = \frac{-\Delta H^* + \Delta H^\circ}{RT} + \Delta S^* - \Delta S^\circ \quad (14)$$

where ΔS^* is an activation entropy. Combining this with the vapor pressure expression which is given in terms of the standard heat of formation ΔH° and the standard entropy of formation by

$$\ln p_s = \frac{-\Delta H^\circ}{RT} + \Delta S^\circ \quad (15)$$

the Langmuir vapor pressure $p_L = \alpha p_s$ is given by

$$\ln p_L = \frac{-\Delta H^*}{RT} + \Delta S^* \quad (16)$$

From Eq. (14), a rapid variation of α with T requires $\Delta H^* \gg \Delta H^\circ$. Combining Eqs. (12) and (16)

$$\ln p_0 = \frac{-\Delta H^*}{RT} + \Delta S^* - \ln F_2(\alpha, \gamma) \quad (17)$$

²⁵ Rosenblatt, G. M., "Evaporation from Solids," Treatise on Solid State Chemistry, Vol. 6a, Ed. N. B. Hannay, Plenum Press, NY, 1976, p. 199.

Thus, rapid variation of α means the slope of p_0 versus $1/T$, $-\Delta H^*/R$, will be considerably larger in absolute value than $-\Delta H^*/R$ as seen in the data. Conclusions regarding this effect are discussed in Subsection III-B-1.

B. THERMOCHEMICAL PROPERTIES

1. Vaporization Coefficients

The dominant importance of the numerical value of the carbon species C_3 vaporization coefficient α_3 on the calculated results was shown by the parametric sensitivity study discussed in relation to Fig. 7 in Subsection II-A. Because of this and because the assumption of equal values of vaporization coefficients for all species is reasonable above 3000°K ,¹³ in all the results presented here it has been assumed that $\alpha_1 \equiv \alpha$.

For given values α and γ , the calculated results shown in Fig. 3 and represented functionally by Eq. (11), can be expressed as

$$\dot{m} = C \sqrt{\frac{M}{2\pi RT_s}} p_s \quad (18)$$

where C is a constant. A semi-log plot of \dot{m} versus $1/T_s$ [see Eq. (15)] thus will have nearly the same slope as p_s , i.e., the slope will be $-\Delta H^*/R$ where ΔH^* is the reference heat of formation. For different values of α , the "constant" C has a different numerical value. Lines showing $\dot{m} = \dot{m}A_{sp}$ versus $1/T_s$ for the various values of α will be parallel to one another as shown in Fig. 10. The total mass loss rate \dot{M} (mg/sec) is obtained from \dot{m} ($\text{g}/\text{cm}^2\text{-sec}$) by multiplying by the laser spot area A_{sp} (cm^2) and dividing by 1000.

The lines in Fig. 10 were calculated assuming the total vapor pressure p_s to be given by the carbon species thermochemical data tabulated in Refs. 26 and 27. Hereafter, these thermochemical data will be referred to as the Livermore data. If, instead, the JANAF data⁴ are used, the predicted M versus inverse temperature behavior will be as shown in Fig. 11. Some of the reasons for the difference in these two thermochemical data sets are discussed in the final paragraphs of Subsection III-B-2. Note the different slopes and intercepts for given constant α in Figs. 10 and 11.

Comparison of the predicted results in Figs. 10 and 11 with experimental data allows α to be determined graphically as a function of T_s . Low ambient pressure data for pyrolytic graphite samples obtained in the continuous wave laser experiments (See Appendix A and Ref. 10) are also shown in these figures along with a best fit line through the data. Comparison of the data lines in Figs. 10 and 11 with the predicted results gives the vaporization coefficient values and temperature dependence shown in Fig. 12 for the two thermochemical data sets.

Similarly, for given values of α and γ , the calculated results shown in Fig. 13 and represented functionally by Eq. (12), can be expressed as

$$p_0 = C_2 p_s \quad (19)$$

²⁶Lee, E. L. and R. H. Sanborn, "Extended and Improved Thermal Functions for the Gaseous Carbon Species C₁-C₇ from 298 to 10,000°K," High Temperature Science, Vol. 5, 1973, pp. 438-453.

²⁷Leider, H. R., O. H. Krikorian, and D. A. Young, "Thermodynamic Properties of Carbon Up to the Critical Point," Carbon, Vol. 11, 1973, pp. 555-563.

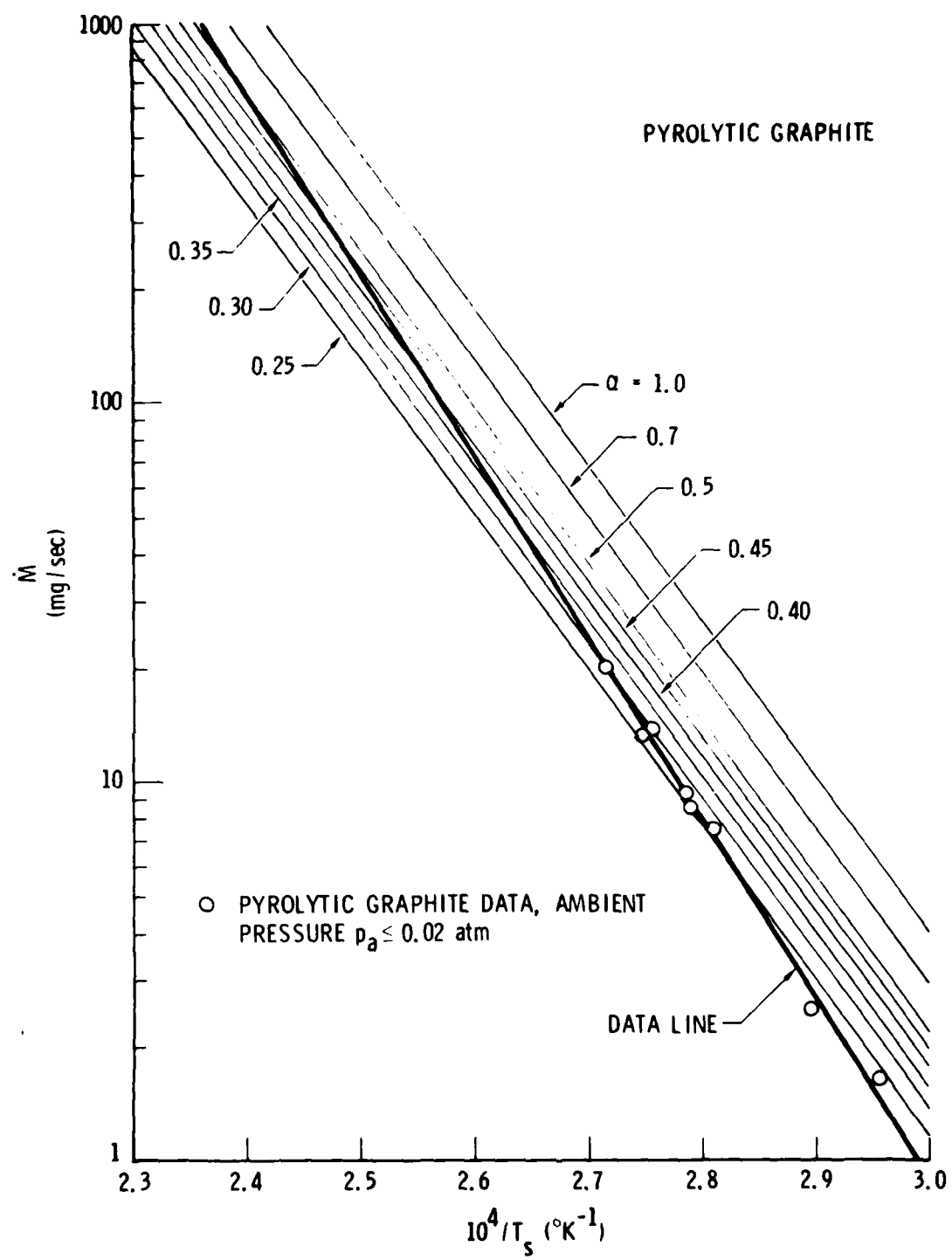


Fig. 10. Comparison of CW Laser Data and Predicted Results (Livermore)

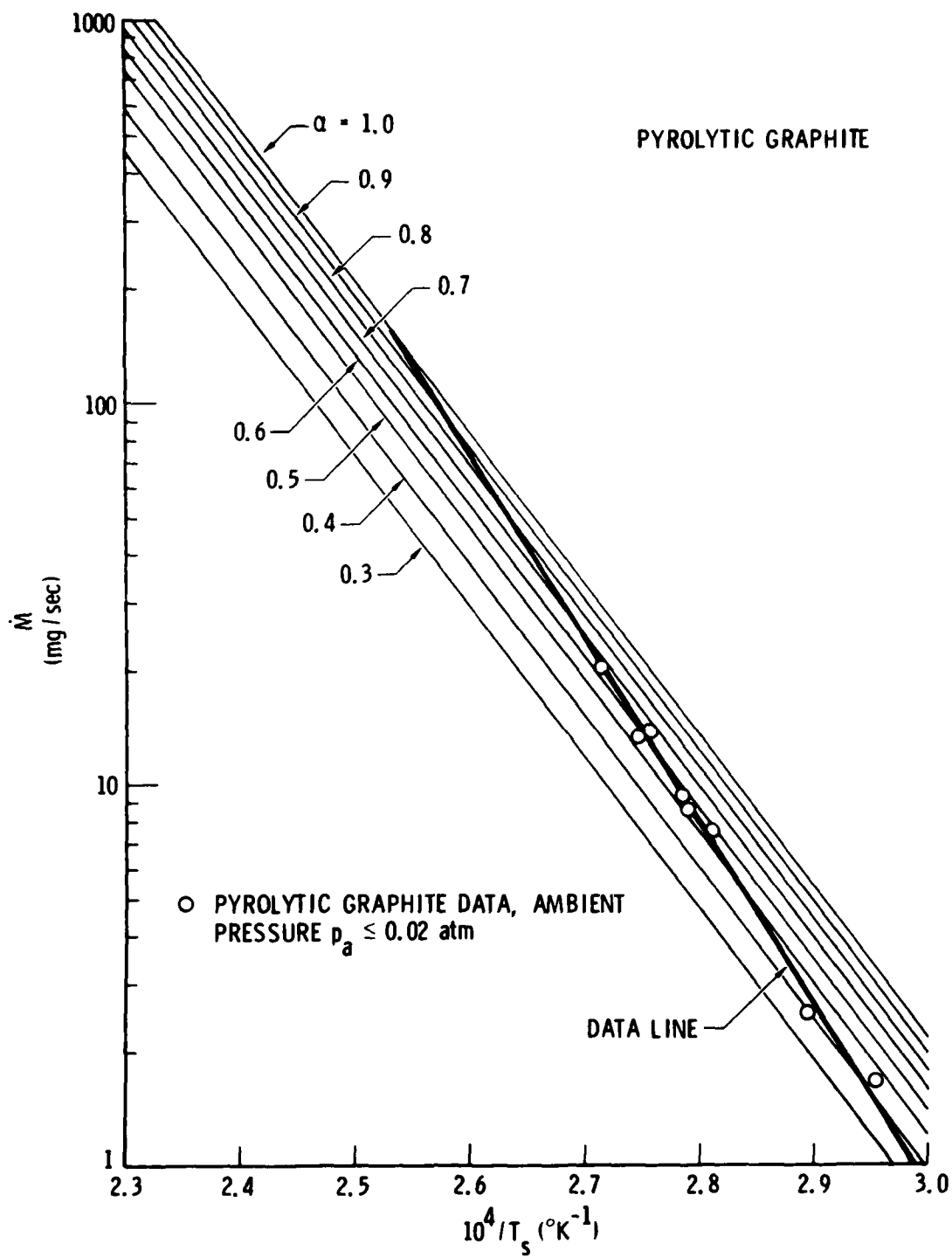


Fig. 11. Comparison of CW Laser Data and Predicted Results (JANAF)

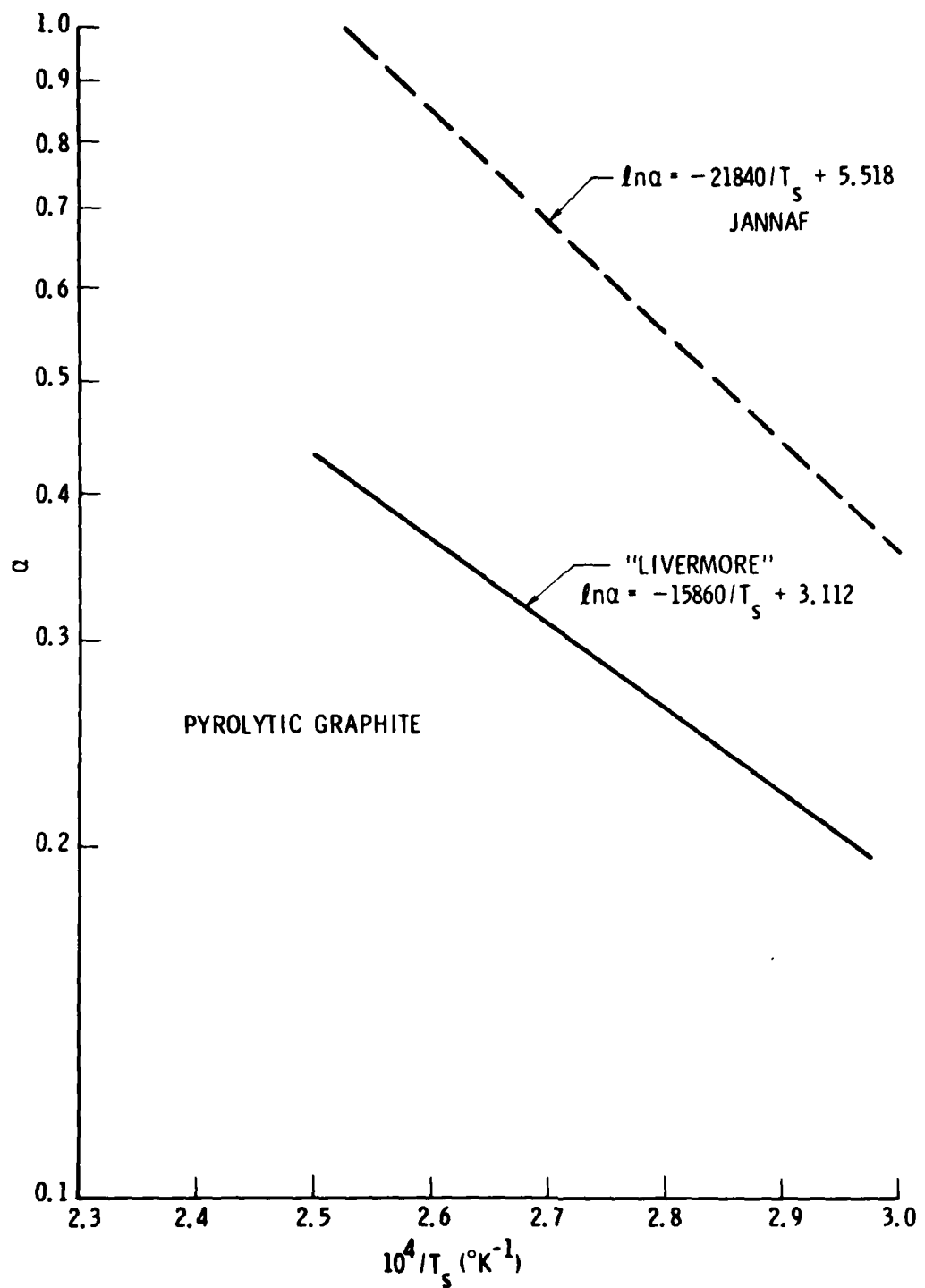


Fig. 12. Vaporization Coefficients Derived from CW Laser Data

Figures 13 and 14 give the predicted stagnation pressure p_0 as a function of inverse temperature for the same thermochemical data and vaporization coefficient values as in Figs. 10 and 11. The pulsed laser stagnation pressure data are presented in Fig. 15. The data line from Fig. 15 is also shown in Figs. 13 and 14. (It is severely truncated in Fig. 14 because α values > 1.0 are not physically meaningful.) Vaporization coefficients obtained graphically from Figs. 13 and 14 are seen in Fig. 16.

The results of Figs. 12 and 16 are combined, and the experimentally determined values of α from 3400°K to 4600°K are presented in Figs. 17 and 18 for the Livermore and JANAF thermochemical data, respectively. In Fig. 17, the high sensitivity of the results to the value of surface emissivity, used in reducing the pyrometer data to obtain surface temperature, is also shown. An emissivity of 0.97 for the pulsed laser data is particularly attractive because the numerical values of the high temperature data then match the lower temperature data at 4000°K and approach unity at the Livermore theoretical triple point (melt) temperature (4765°K). In marked contrast, the vaporization coefficients based on the JANAF thermochemical data (Fig. 18) are physically meaningful, i.e., less than unity, above 4200°K only if much lower values of emissivity are appropriate for the pulsed laser data.

2. Vapor Pressure

The vaporization coefficient discussion just completed gives values of the vaporization coefficient as a function of temperature derived from two vapor pressure relationships, i.e., Livermore and JANAF. The total vapor pressure for carbon predicted by these two sets of recommended thermochemical data is shown in Fig. 19. The Livermore-predicted total vapor pressure is higher by a factor of about 2.5 at 4000°K and by a factor of about 3.9 at 4765°K.

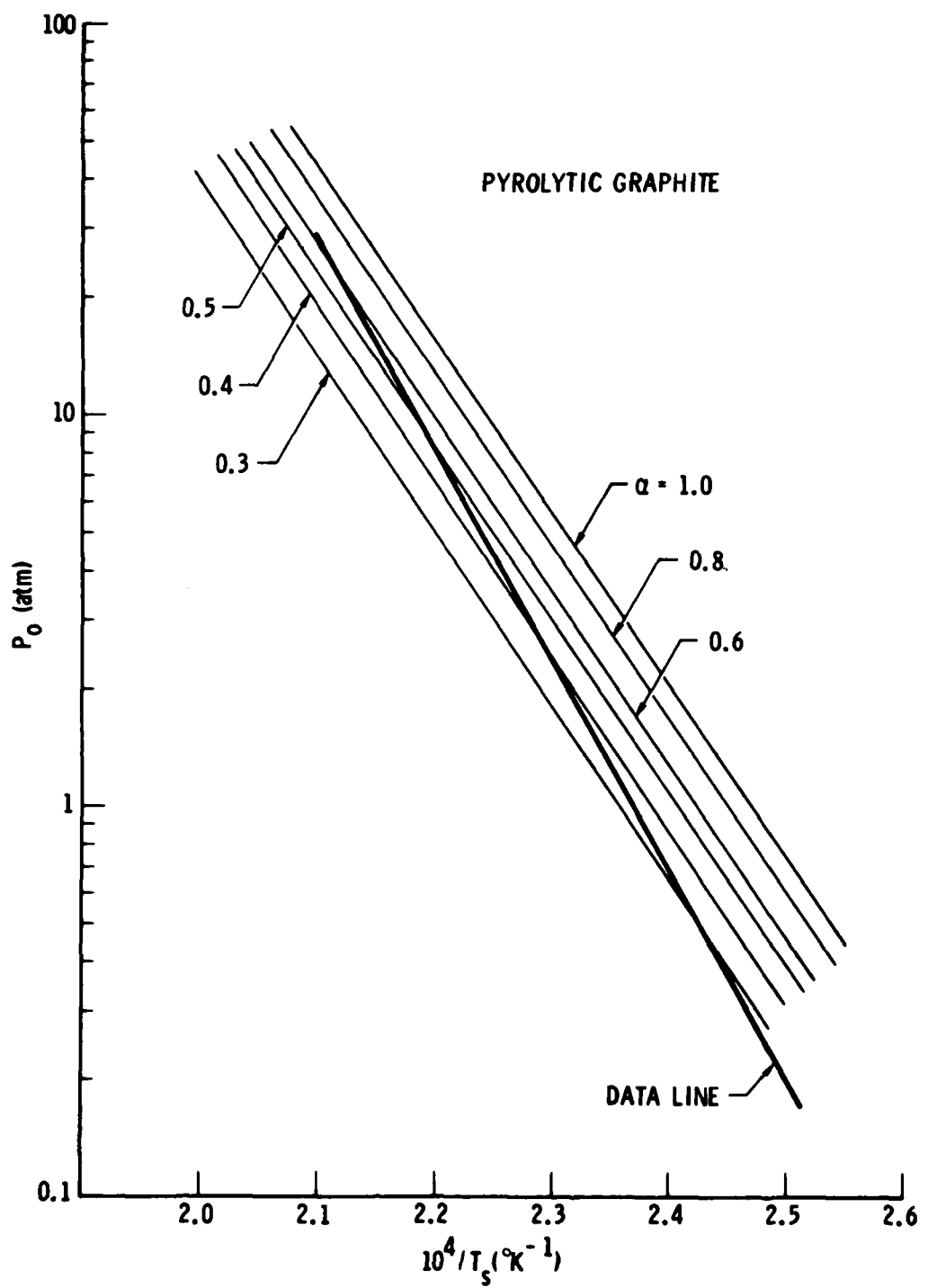


Fig. 13. Comparison of Pulsed Laser Data and Predicted Results (Livermore)

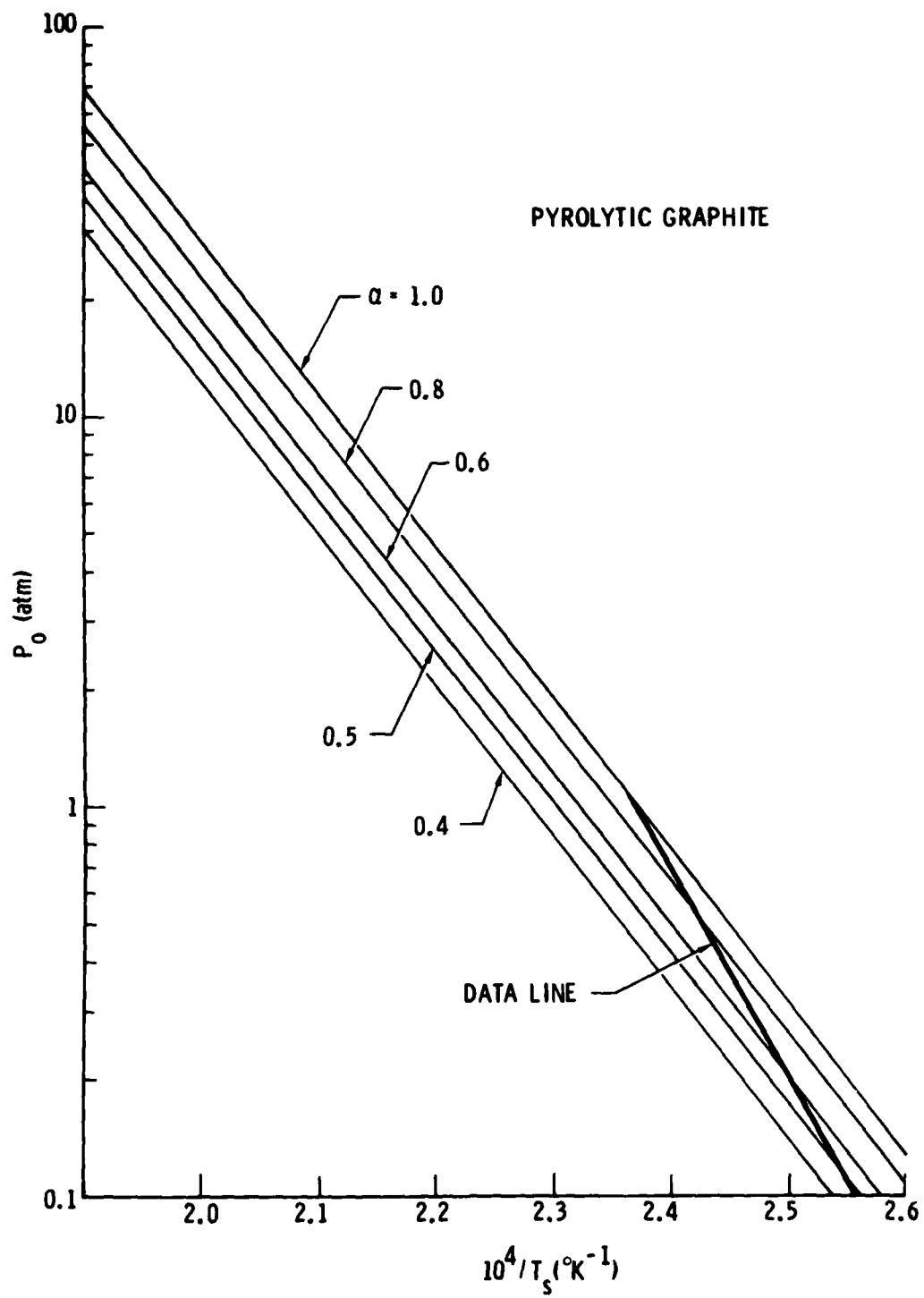


Fig. 14. Comparison of Pulsed Laser Data and Predicted Results (JANAF)

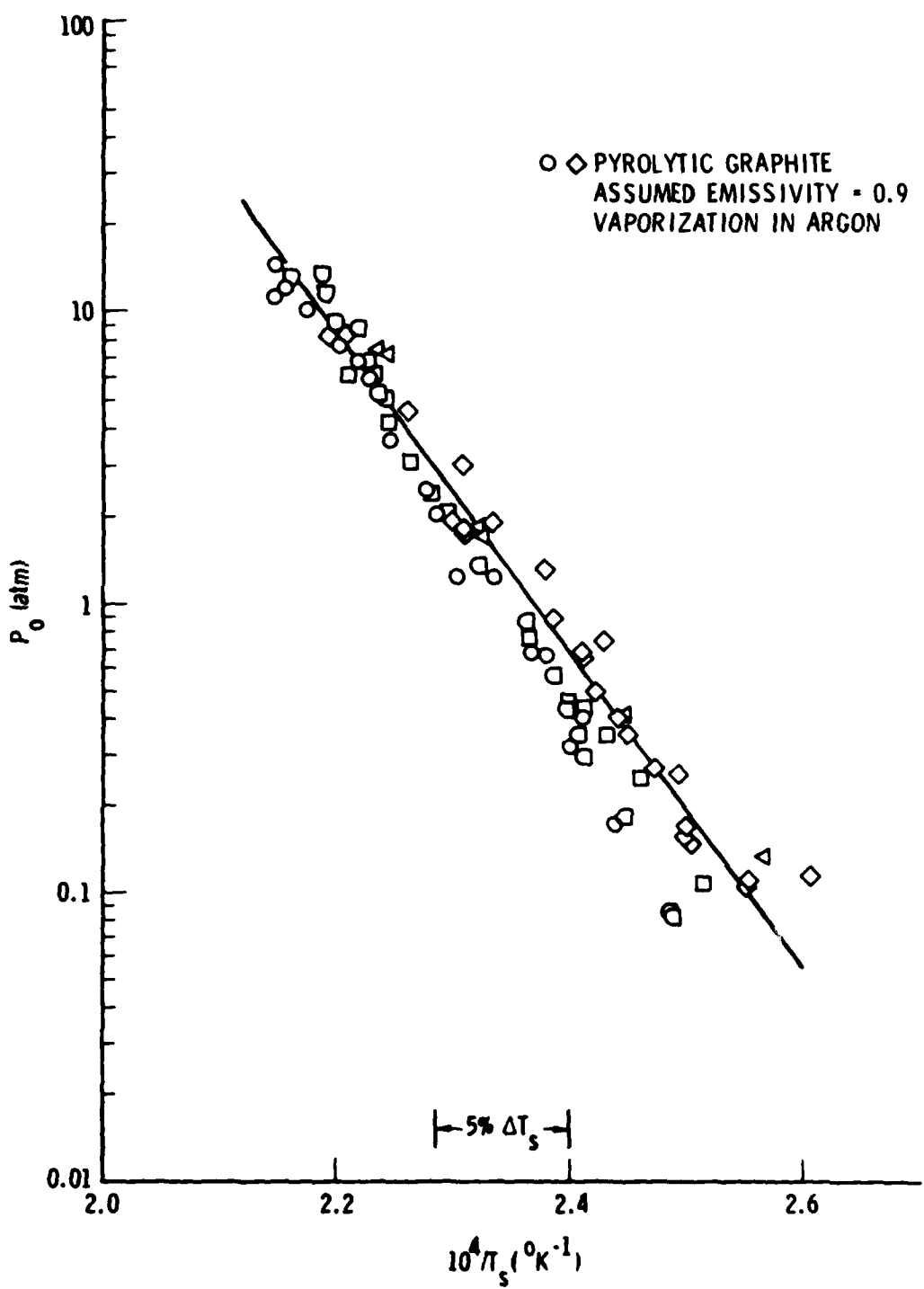


Fig. 15. Pulsed Laser Data and Data Line

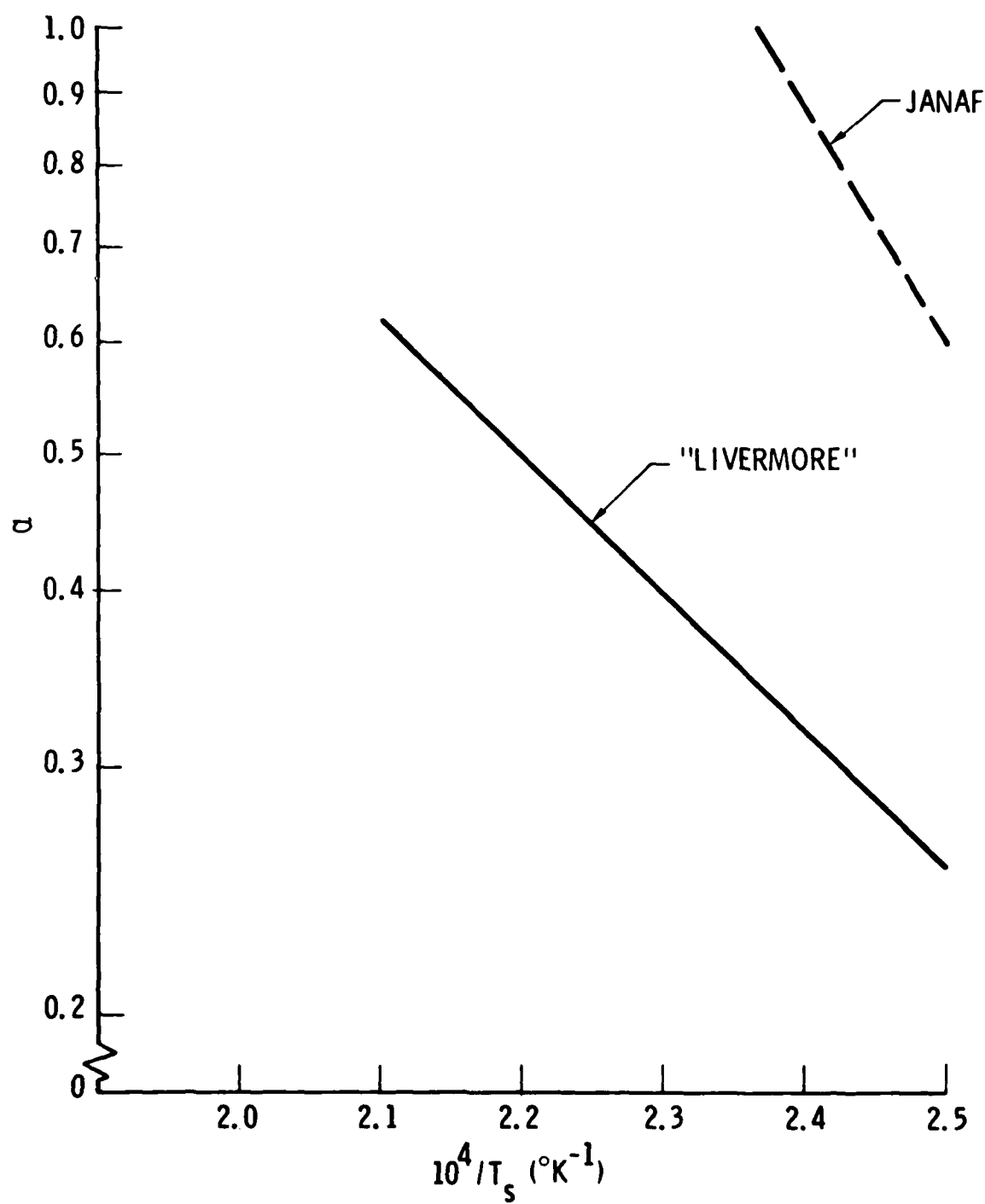


Fig. 16. Vaporization Coefficients Derived from Pulsed Laser Data

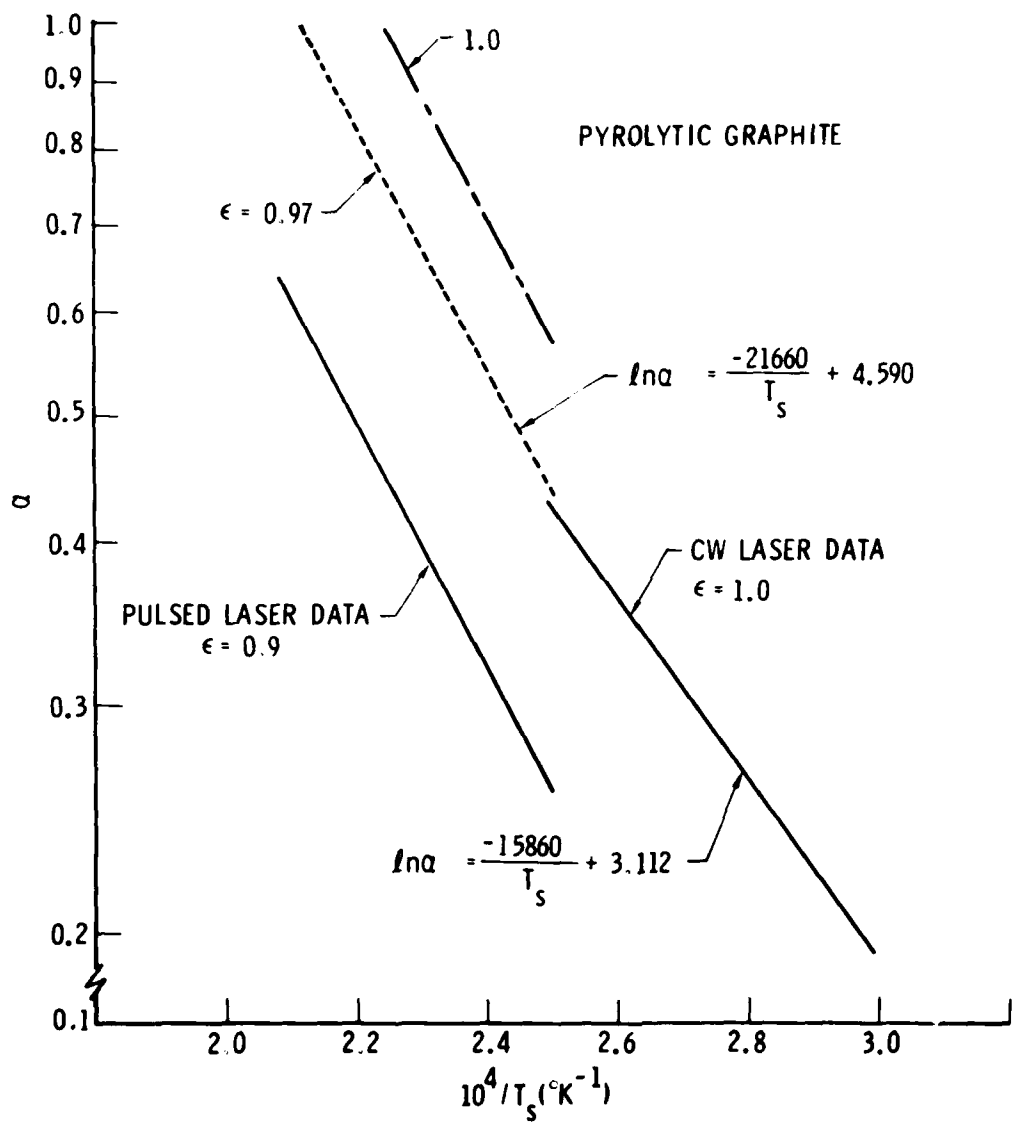


Fig. 17. Vaporization Coefficients for Livermore Thermochemical Data

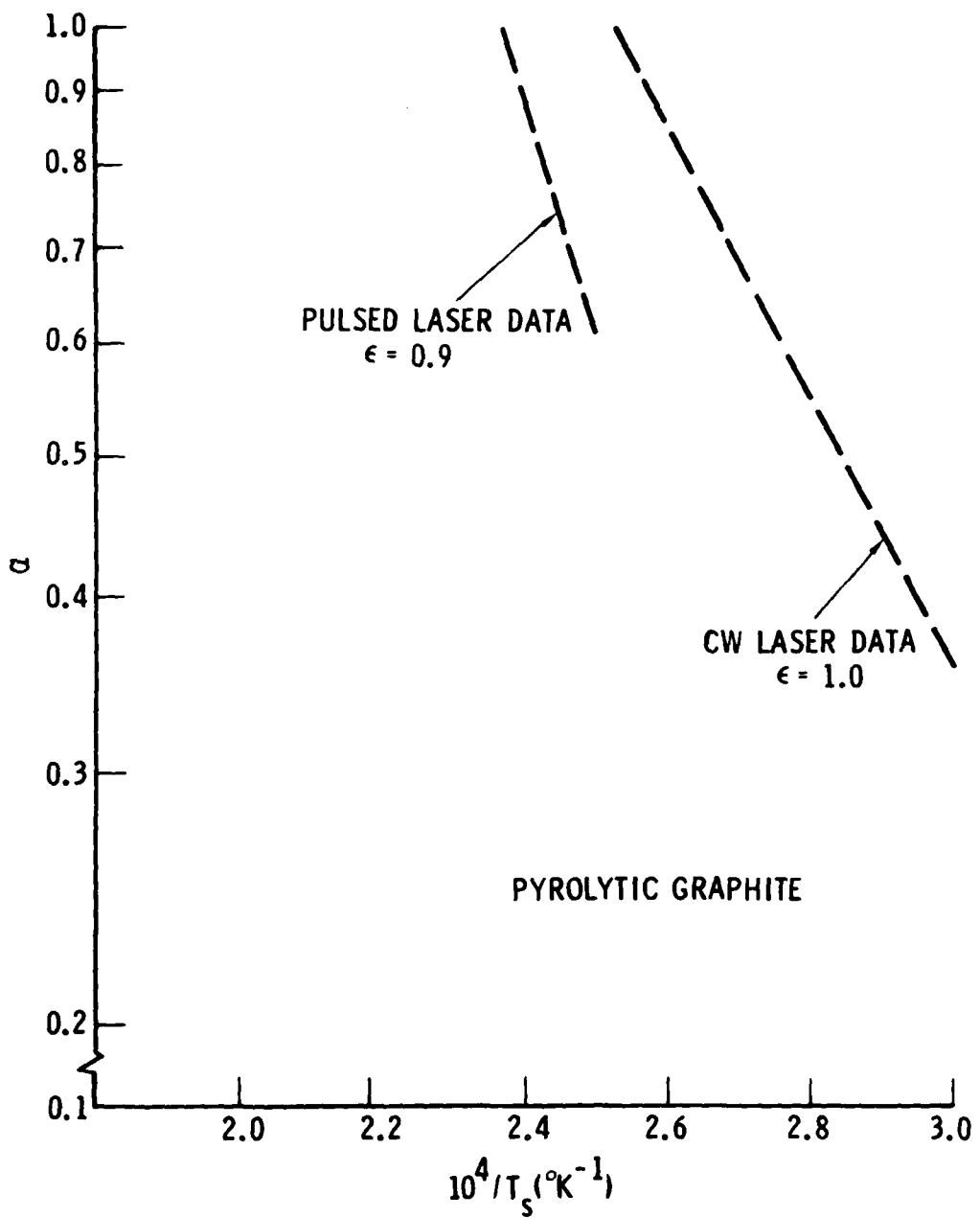


Fig. 18. Vaporization Coefficients for JANAF Thermochemical Data

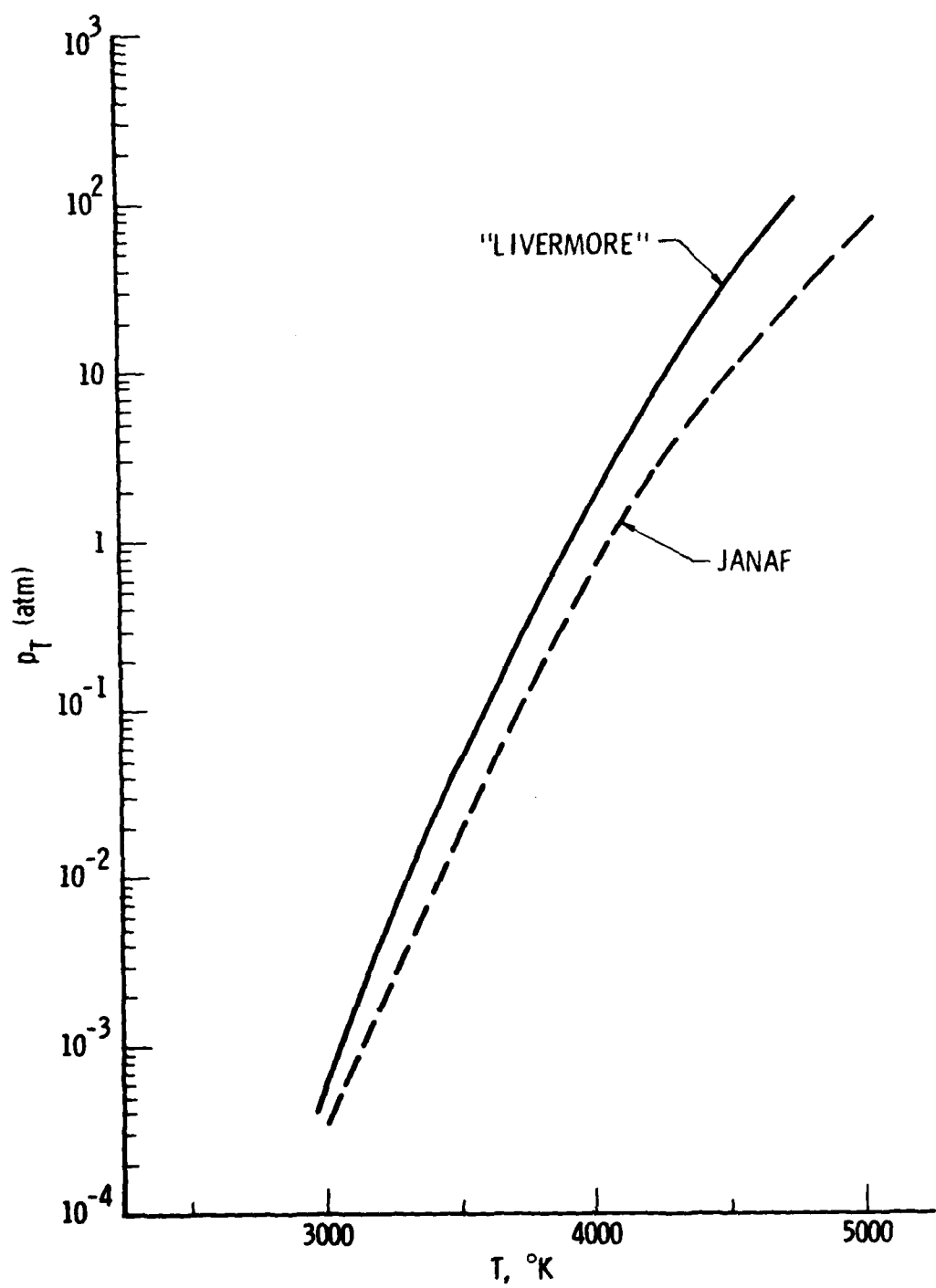


Fig. 19. Carbon Total Vapor Pressure

The intended method of determining which thermochemical data are more nearly correct has been reviewed in Subsection III-A and is discussed in detail in Ref. 10. It is based upon predicted differences in behavior between experimental data obtained when the ambient pressure is low relative to the vapor pressure and other experimental data obtained for higher ambient pressures (the order of the vapor pressure). This is illustrated in Fig. 20.

The data points used to determine the temperature dependence of the vaporization coefficients and the consequent "agreement" of JANAF- and Livermore-predicted mass loss rates with the data are seen in Fig. 20a. The same data points and predicted mass loss rates for ambient pressure $p_a = 1$ Torr are shown in Figs. 20b and 20c. Also shown in these latter figures are predicted mass loss rates for p_a ranging from 0.02 to 1.0 atmospheres for the JANAF and Livermore thermochemical data with corresponding vaporization coefficients. In Figs. 21 through 23, these predicted results are compared with the experimental data.

The data are very sparse, especially in Fig. 21. For these data, the ambient pressure is not high enough relative to the vapor pressure to cause a measurable difference in JANAF- and Livermore-predicted results at the measured surface temperature T_s . For the higher ambient pressure data in Figs. 22 and 23, the observed dependence of mass loss rate on ambient pressure and surface temperature is reasonably in agreement with analytical predictions based upon the Livermore thermochemical data. In contrast to this, much less satisfactory agreement of the experimental data with predictions is obtained when JANAF vapor pressures are used. Based upon this and the discussion below, it is concluded that the Livermore data should be used to calculate carbon vapor pressure as a function of temperature.

The basis for the Livermore thermochemical data appears to be very well founded. The reference heat of formation used for the critical carbon species C_3 molecule is within 0.5 kcal/mol of the average experimental value

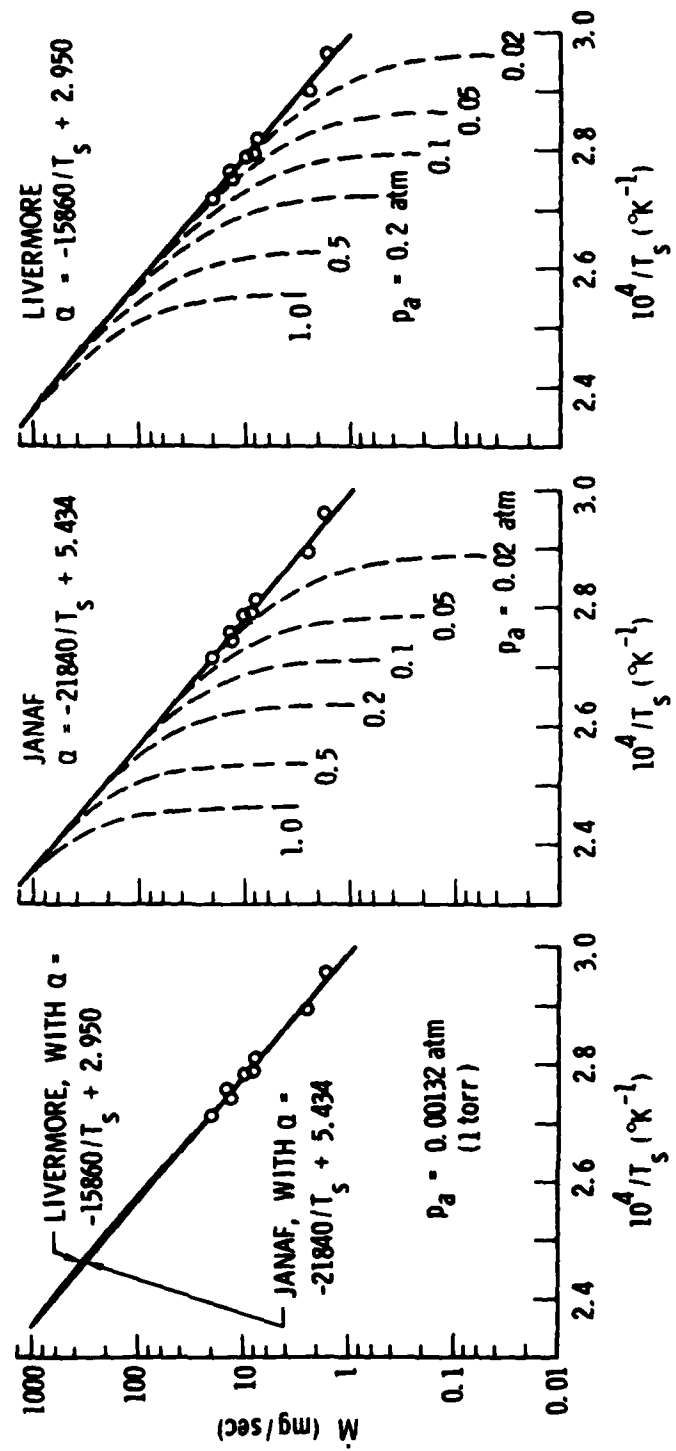


Fig. 20. Variation of Mass Loss Rate with Surface Temperature and Ambient Pressure

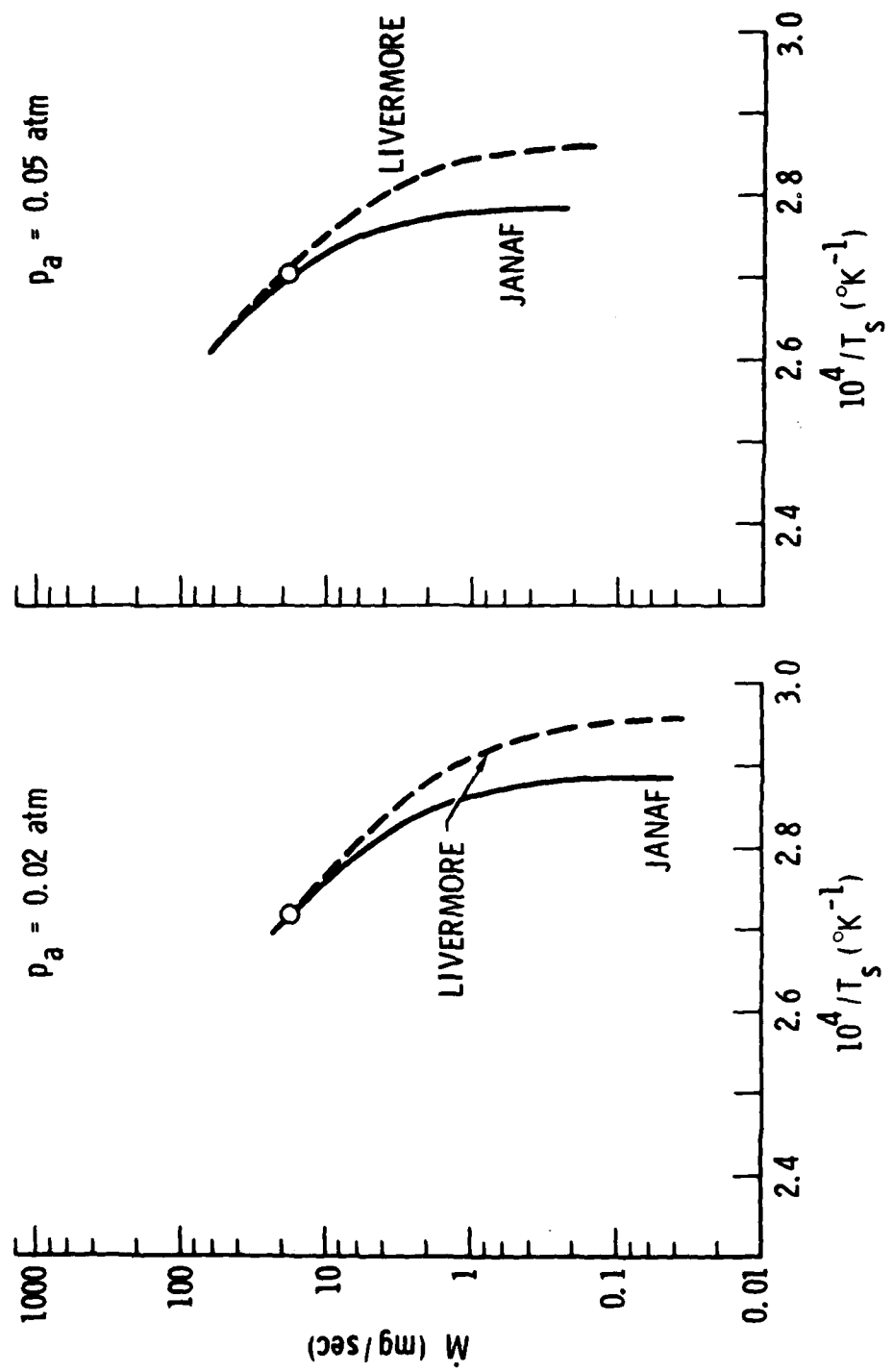


Fig. 21. Comparison of Measured and Predicted Loss Rates,
 (a) $p_a = 0.02 \text{ atm}$, (b) $p_a = 0.05 \text{ atm}$

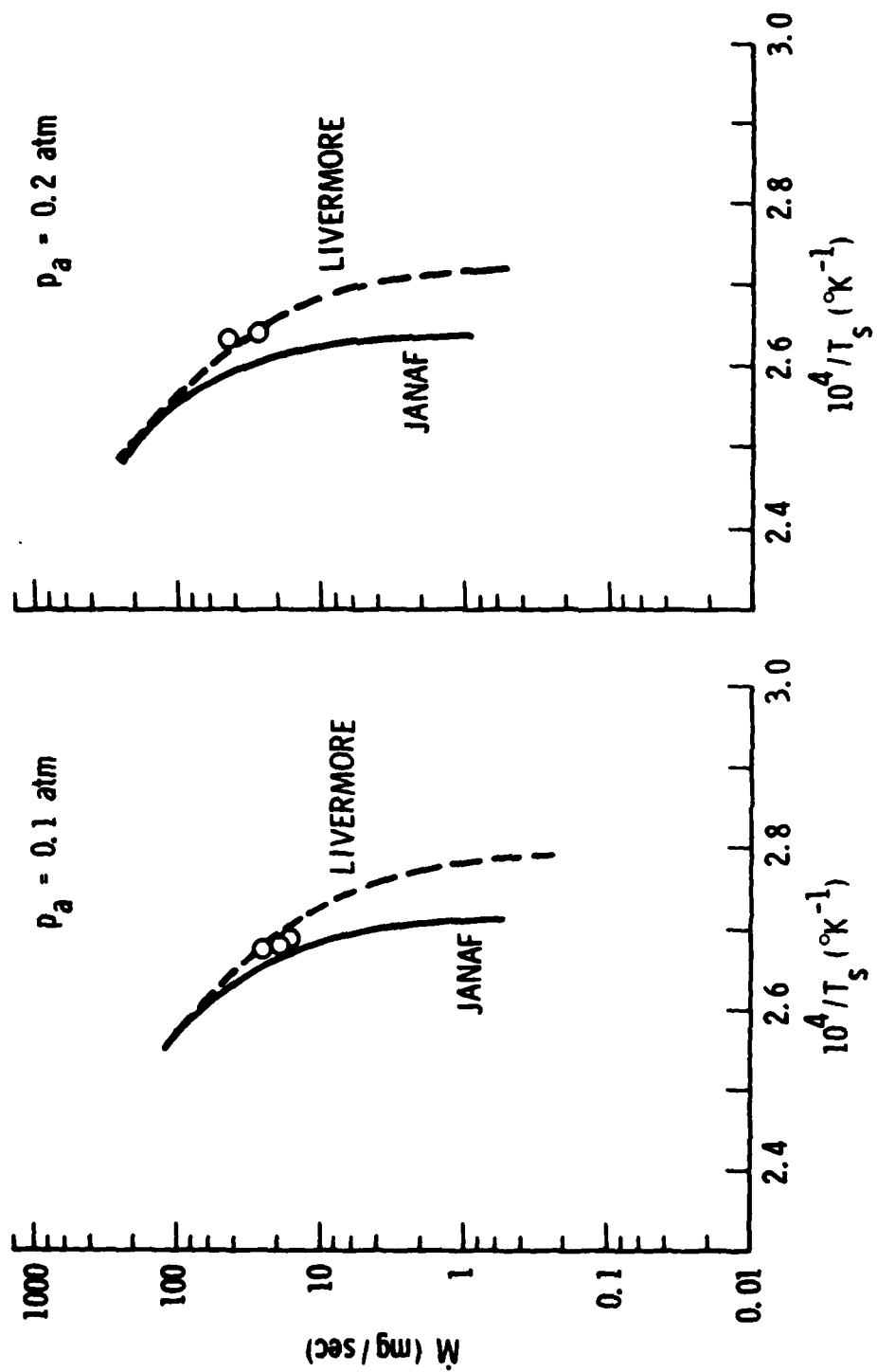


Fig. 22. Comparison of Measured and Predicted Loss Rates,
 (a) $P_a = 0.1 \text{ atm}$, (b) $P_a = 0.2 \text{ atm}$

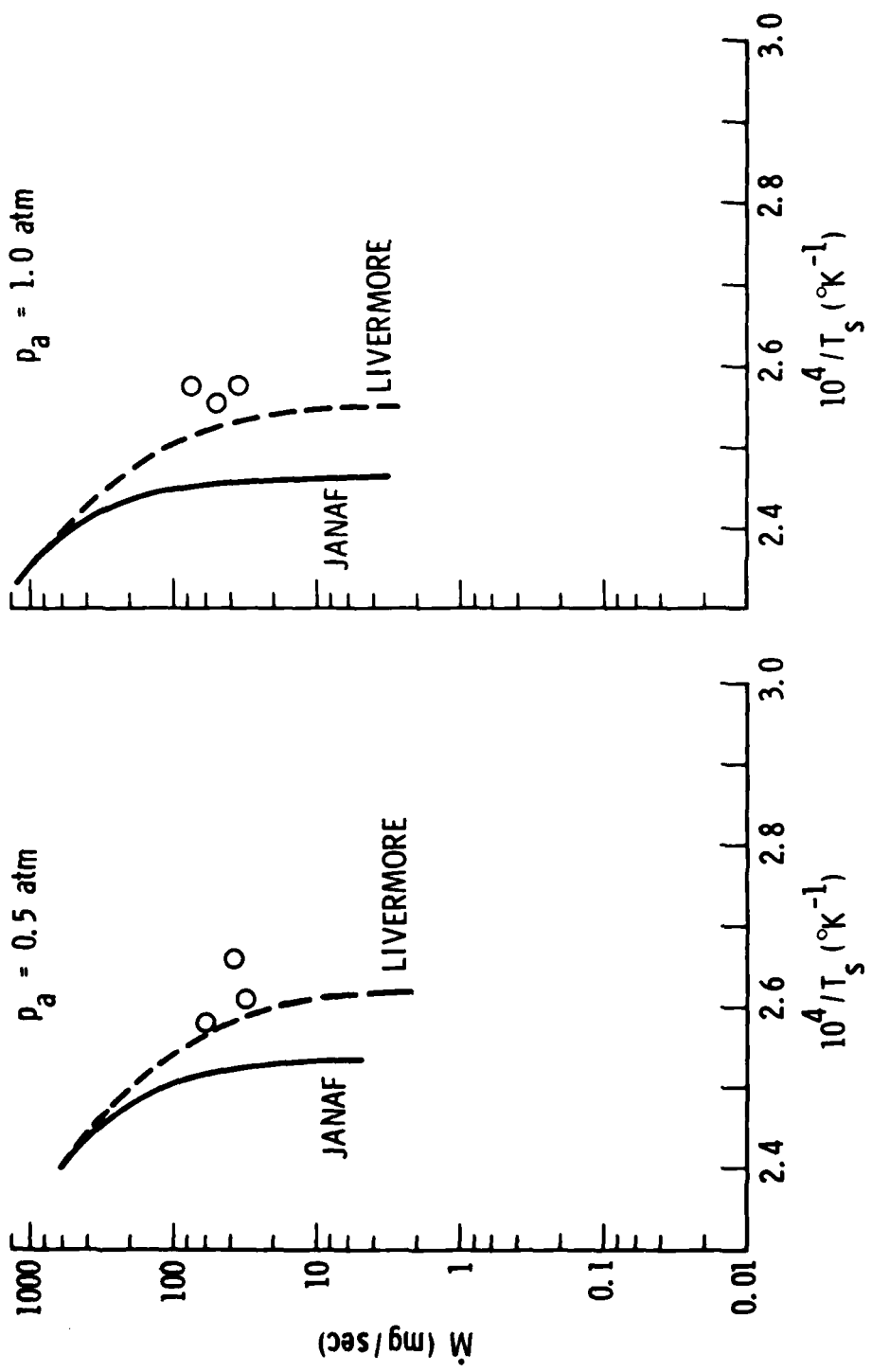


Fig. 23. Comparison of Measured and Predicted Loss Rates,
(a) $p_a = 0.5$ atm, (b) $p_a = 1.0$ atm

determined by Wachi and Gilmartin.²⁸ This is significant because these investigators, for the first time, obtained very good agreement of their third-law and second-law derived heat of formation. The free energy functions for the Livermore data were calculated by Lee and Sanborn²⁶ including contributions of electronic degrees of freedom. Without the very high temperature contributions due to the electronic degrees of freedom, their thermal functions are essentially in agreement with the established values of Strauss and Thiele,²⁹ and their entropy values are above the "lower limits" determined by Hansen and Pearson.³⁰ In contrast to this, the JANAF-recommended entropies for C₃ are below the Hansen and Pearson lower limits, and the JANAF reference heat of formation for C₃ is 5.7 kcal/mol less than the average Wachi and Gilmartin value.

A final appealing feature of the Livermore data, as discussed by Leider, Krikorian, and Young,²⁷ is that the total vapor pressure reaches the triple point pressure (≈ 100 atm) at 4765°K. This is several hundred degrees above the literature values for triple point (melt) temperature, but consistent with the melt temperature conclusion discussed in the following section. A significant fraction of the Livermore-predicted total carbon vapor pressure at 4765°K is due to carbon species above C₅, especially C₇. The contributions of these species to the total vapor pressure are supported by the larger slope of the high temperature Langmuir vapor pressure data in Fig. 15. The JANAF tables presently do not give data for carbon species above C₅. Because of this and the low JANAF C₃ vapor pressure, the JANAF-predicted triple point temperature is ≈ 5125 °K.

²⁸Wachi, F. M. and D. E. Gilmartin, "Heat of Formation and Entropy of C₃ Molecule," High Temperature Science, Vol. 4, No. 5, pp. 423-431.

²⁹Strauss, H. L. and E. Thiele, "Thermodynamics of C₃. II. General Methods for Nonrigid Molecules at High Temperatures," Journal of Chemical Physics, Vol. 46, No. 7, pp. 2473-2480.

³⁰Hansen, C. F. and W. E. Pearson, "A Quantum Model for Bending Vibrations and Thermodynamic Properties of C₃," Canadian Journal of Physics, Vol. 51, 1973, pp. 751-760.

3. Melt Temperature

a. Carbon Phase Change Detection Using Surface Reflectance

This investigation of the possible phase change of carbon used a new technique evidently not employed previously in carbon studies to detect the presence of a melt layer on a solid substrate. The application of this method was inspired by recent success in the use of time-resolved spectral reflectivity of doped silicon to monitor surface phase change during laser-heated annealing.¹⁸ The reflective behavior of germanium (Ge) and silicon (Si) heated to melting are included along with carbon results to provide comparative data when a liquid layer was known to be present.

The reflection and refraction of an electromagnetic wave at the optically smooth surfaces of liquid and solid materials can be accurately described by the Fresnel equations in terms of the material's optical indices and the incidence angle of the radiation. However, once a surface is heated to temperatures where melting or significant vaporization occurs, it becomes roughened and is no longer optically smooth. The induced discontinuities cause scattering of incident radiation independent of the material's intrinsic optical properties and, if the size of the irregularities is of the order of the radiation wavelength or larger, the scattering dominates the reflective behavior. In this case, the directional distribution of reflected radiation can be best described by geometric optics that take into account the statistical nature of surface features.

In these experiments, it was found to be advantageous to roughen the Ge and Si surfaces prior to exposure to insure uniform melting over the heated area. Also, graphite surfaces were roughened by vaporization regardless of their initial smoothness. This makes the strict application of the Fresnel relations for predicting expected changes between solid and liquid phases inappropriate for the data included herein. Since the purpose of this investigation was to measure relative, transient changes in surface reflectance as a means to detect melting, comparisons between absolute reflectivity values predicted from electromagnetic theory for smooth surfaces and experimentally measured bidirectional or spatially integrated reflectivities are not included.

However, for the directional reflectance method and the materials used, the reflected radiation flux is characterized by a specular component and a diffuse component distributed about the reflection angle of the specular component. The specular component increases in relative intensity with increasing incidence angle (i.e., larger grazing angles), and reflection of a collimated beam approaches that for pure specular reflection. This makes the Fresnel equations useful for comparing beam polarization and incidence angle effects as well as the relative reflectances expected during heating.

For a solid or liquid material having optical properties that are constant in all directions, the Fresnel equations for an isotropic, absorbing medium relate the fraction of incident radiation that is reflected from an optically smooth surface to the refractive index, the absorption index, and the incidence angle of the radiation:³¹

$$R_{\perp} = \frac{(\cos\theta - \alpha)^2 + \beta^2}{(\cos\theta + \alpha)^2 + \beta^2} \quad (20)$$

$$R_{\parallel} = \frac{(\gamma\cos\theta - \alpha)^2 + (\delta\cos\theta - \alpha)^2}{(\gamma\cos\theta + \alpha)^2 + (\delta\cos\theta + \alpha)^2} \quad (21)$$

³¹Born, M., and E. Wolf, Principles of Optics, 2nd Edition, Pergamon Press, NY, 1964.

where

R_{\perp} and R_{\parallel} = the reflectivity of radiation polarized perpendicular and parallel, respectively, to the plane of incidence.

$$\left\{ \begin{array}{l} 2\alpha^2 \\ 2\beta^2 \end{array} \right\} = \left[(n^2 - k^2 - \sin^2\theta)^2 + 4n^2 k^2 \right]^{1/2} \pm (n^2 - k^2 - \sin^2\theta)$$

$$\gamma = n^2 - k^2 , \quad \delta = 2nk$$

n = refractive index

k = absorption index

θ = incidence angle

These relations are appropriate for many solid and liquid substances including the crystalline and liquid Ge and Si and, probably, the liquid phase of carbon considered herein.

For strongly absorbing anisotropic crystals, the above relationship for isotropic materials does not properly account for different optical properties along the crystal axes. Anisotropic uniaxial materials having only one unique direction are typified by pyrolytic graphite with its stacked parallel layers of carbon atoms. The reflection from optically smooth surfaces of uniaxial crystals having optical properties along the c-axis that are different from those normal to the axis is given by³²

$$R_{\perp} = \frac{(\cos\theta - a_{\perp})^2 + b_{\perp}^2}{(\cos\theta + a_{\perp})^2 + b_{\perp}^2} \quad (22)$$

$$R_{\parallel} = \frac{(c \cdot \cos\theta - a_{\parallel})^2 + (d \cdot \cos\theta - b_{\parallel})^2}{(c \cdot \cos\theta + a_{\parallel})^2 + (d \cdot \cos\theta + b_{\parallel})^2} \quad (23)$$

³²Mosteller, L. P., and F. Wooten, "Optical Properties and Reflectance of Uniaxial Absorbing Crystals," J. Optical Society of America, Vol. 58, 1968, pp. 511-518.

where

R_{\perp} and R_{\parallel} = the reflectivity of radiation polarized perpendicular and parallel, respectively, to the plane of incidence.

$$\left\{ \frac{2a_{\perp}^2}{2b_{\perp}^2} \right\} = \left[(n_x^2 - k_x^2 - \sin^2 \theta)^2 + 4n_x^2 k_x^2 \right]^{1/2} \pm (n_x^2 - k_x^2 - \sin^2 \theta)$$

$$\left\{ \frac{2a_{\parallel}^2}{2b_{\parallel}^2} \right\} = \left[(n_z^2 - k_z^2 - \sin^2 \theta)^2 + 4n_z^2 k_z^2 \right]^{1/2} \pm (n_z^2 - k_z^2 - \sin^2 \theta)$$

$$c = (n_x n_z - k_x k_z) \quad , \quad d = (n_x k_z - n_z k_x)$$

n_j = refractive index in j -direction

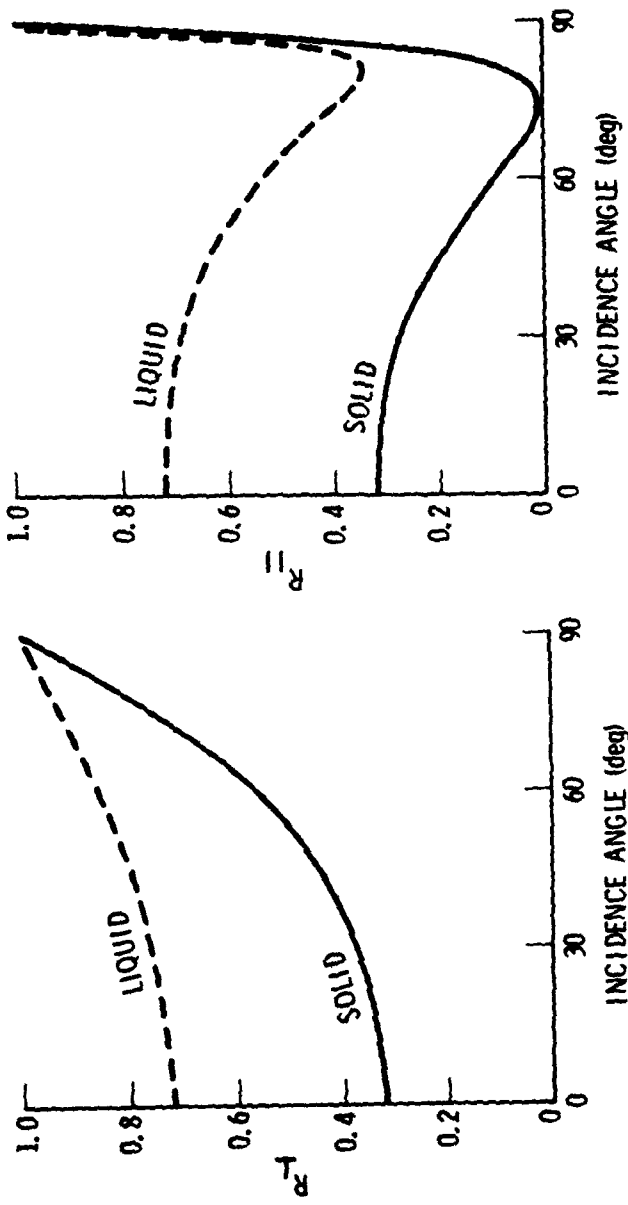
k_j = absorption index in j -direction

θ = incidence angle

Note that the equations for uniaxial crystals differ from those for isotropic materials only by including the differences in refraction and absorption indices along orthogonal axes.

Using Eqs. (20) and (21) with optical properties taken from Refs. 33 and 34, for the reflection from optically smooth surfaces of solid and liquid Si in vacuum as shown in Fig. 24, it is easily seen that the use of a collimated beam polarized so that its electric vector is perpendicular to the plane of incidence, and large grazing angles will maximize the reflected energy. Likewise, the use of Eqs. (22) and (23) for the reflection from smooth surfaces of solid pyrolytic graphite with its anisotropic optical properties taken from Ref. 35 provides a similar conclusion as shown in Fig. 25. A prediction for the reflectivity of liquid carbon is not included since the optical properties of the liquid phase are not known, and the exact structure of

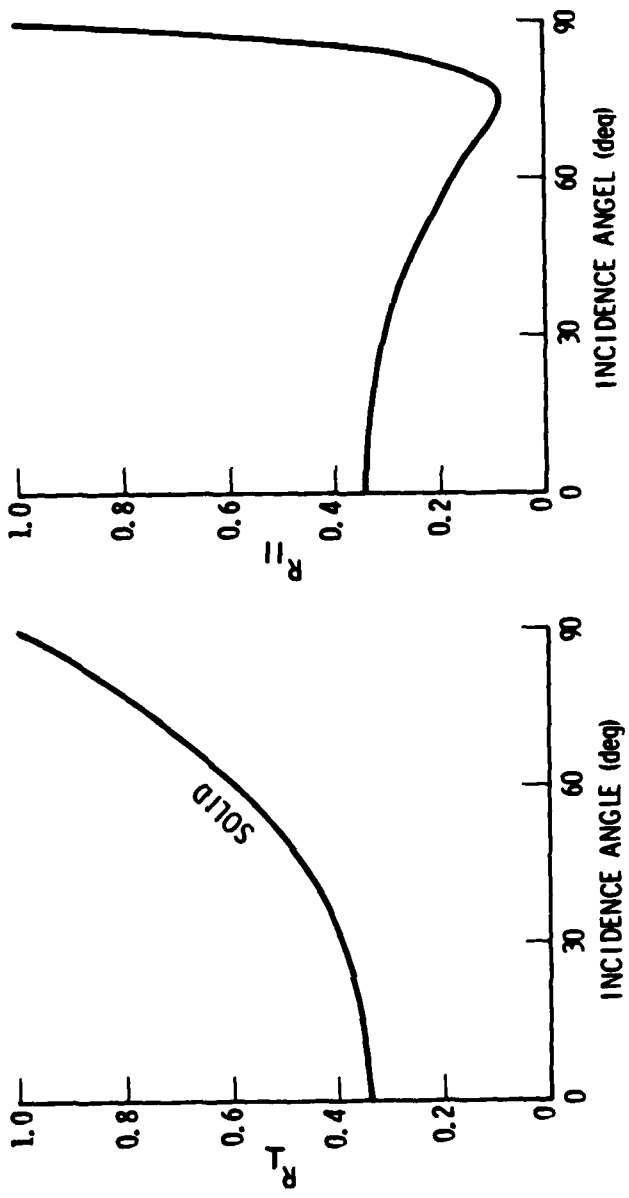
OPTICAL INDICES -- SOLID (Ref. 33): $n = 3.6, k = 0.025$
 LIQUID (Ref. 34): $n = 2.8, k = 5.1$



(a) Polarization Perpendicular to Plane of Incidence (b) Polarization Parallel to Plane of Incidence

Fig. 24. Bidirectional Reflectivity of Silicon

OPTICAL INDICES -- SOLID (Ref. 35): $n_x = 2.55$, $n_z = 1.78$
 $k_x = 1.68$, $k_z = 0$



(a) Polarization Perpendicular to Plane of Incidence (b) Polarization Parallel to Plane of Incidence

Fig. 25. Bidirectional Reflectivity of Pyrolytic Graphite

the liquid is still a matter of debate.^{36,37} However, there is no reason to expect that the reflectance from liquid carbon would be lower than that for the solid.

b. Experimental Results and Conclusions

A schematic of the experimental apparatus utilized is shown in Fig. 26. Material samples were heated within a cylindrical vacuum tank having windows on both ends and around the perimeter. Heating was provided by a pulsed Nd/glass laser producing a uniform cross-section beam at $1.06 \mu\text{m}$ wavelength and operated in the normal, or burst, node. The Nd/glass laser beam irradiated the material sample normal to the front surface over heated areas 2.5 to 4 mm in diameter, and the heating pulse was approximately triangular in shape with a total pulse length of about 1.2 msec. During laser heating cycles the tank was filled with argon at pressures at 10 Torr or less. The incident beam for reflectivity measurements was obtained from a He/Ne laser focused onto the heated sample area at a grazing angle of 60° from the normal.

The He/Ne laser beam was polarized perpendicular to the plane of incidence (E-vector parallel to surface) to maximize the reflectance as previously noted, and the beam was chopped at a frequency of 20 kHz. The beam flux reflected within a small solid angle passed through a $0.633 \mu\text{m}$ spectral line filter to minimize contributions due to the heating laser beam reflection and thermal radiation flux, and then was focused onto a photodiode detector. Simultaneous time-resolved surface temperatures on graphite samples were measured with a Si photodetector pyrometer in conjunction with spectral filters to minimize reflected $1.06 \mu\text{m}$ laser radiation. Because of the low temperatures at which Ge and Si melt, it was not possible to measure time-resolved surface temperatures on these materials.

³⁶Bundy, F. P., "The P, T Phase and Reaction Diagram for Elemental Carbon, 1979," *J. Geophysical Research*, Vol. 85, 1980, pp. 6930-6936.

³⁷Ferraz, A., and N. H. March, "Liquid Phase Metal-Nonmetal Transition in Carbon," *Physical Chemistry of Liquids*, Vol. 8, 1979, pp. 289-297.

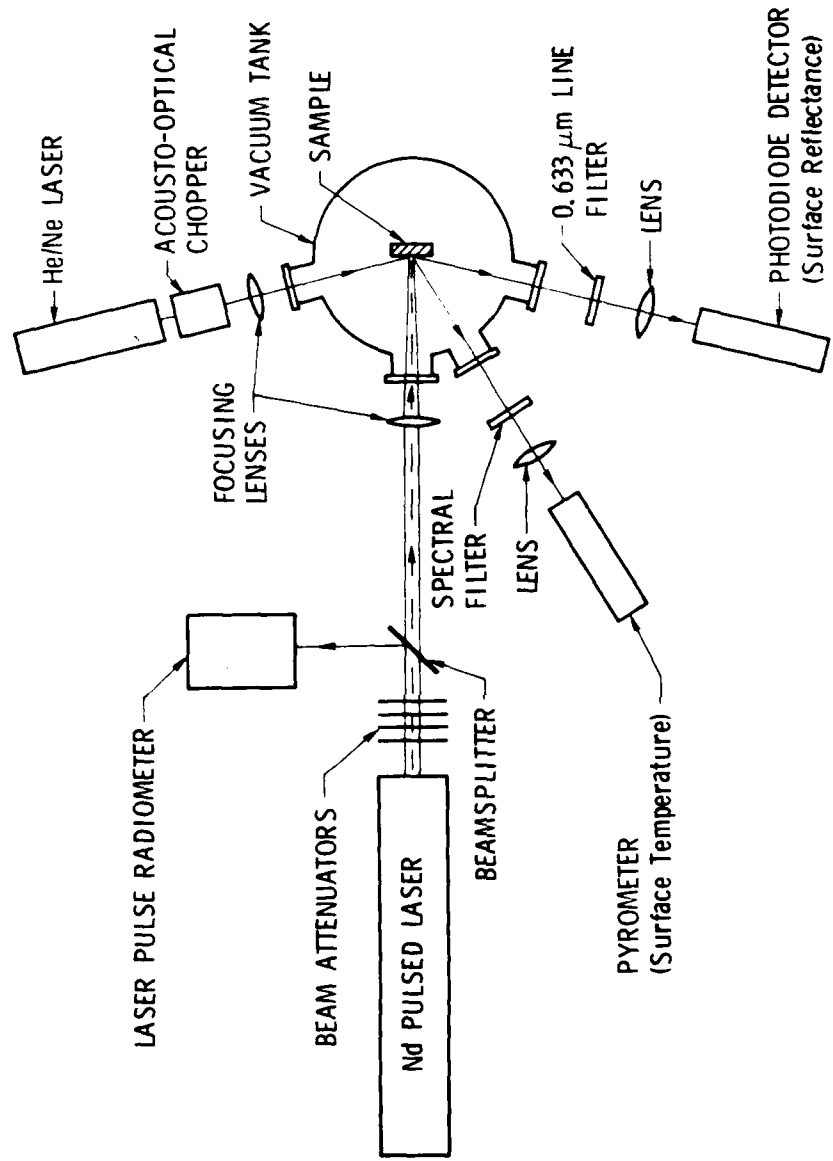


Fig. 26. Experimental Apparatus

The surfaces of Ge and Si samples were roughened with 500 grit paper before exposure to insure uniform surface melting when the surface was heated sufficiently. The pyrolytic graphite surfaces roughened to what appeared to be a stable state as vaporization progressed through multiple heating cycles. The Nd/glass laser beam irradiated the material samples normal to their surface and, in the case of the graphite, this heating and resultant vaporization was perpendicular to the carbon deposition planes.

Typical oscilloscope traces of the surface reflectance signal for laser-heated Ge and Si are given in Figs. 27 and 28. In these photos, the upper trace is the chopped reflected beam signal, and the lower trace shows the time history of the laser pulse intensity. For Ge and Si heated to temperatures below their melting points, the reflectances shown in Figs. 27a and 27b are seen to increase slightly with increasing temperature and then to return to their preheated values.

In contrast to the small changes in reflectance at temperatures below the melting point, Ge and Si exhibit large transient changes when melting does occur, as illustrated in Figs. 28a and 28b. In these oscilloscope photos, the time-resolved reflectance signal is again the upper trace and the instantaneous laser heating flux in arbitrary units is the lower trace. For both Ge and Si, the reflectance is seen to increase as the surface melts and then to decrease to a value intermediate between the liquid and the original solid surface as the melted phase solidifies. The large reflectance changes shown occurred during the first heating pulse that visual evidence of surface melting was observed after several heating cycles with increasing laser peak heating flux. The increase in reflectance is due to the differences in reflectivity of the liquid and solid phases as predicted by Eqs. (20) and (21) in Fig. 24, and as observed during laser annealing of doped Si semiconductor materials.

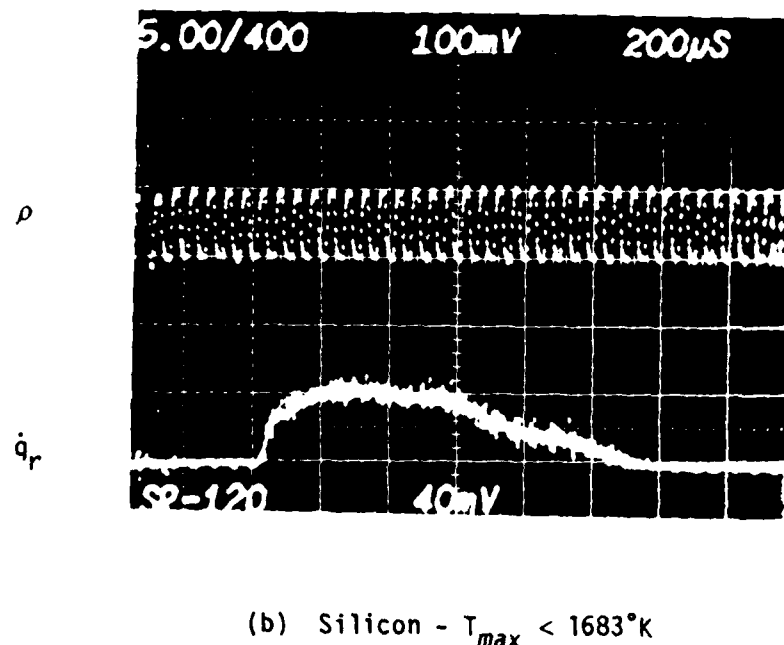
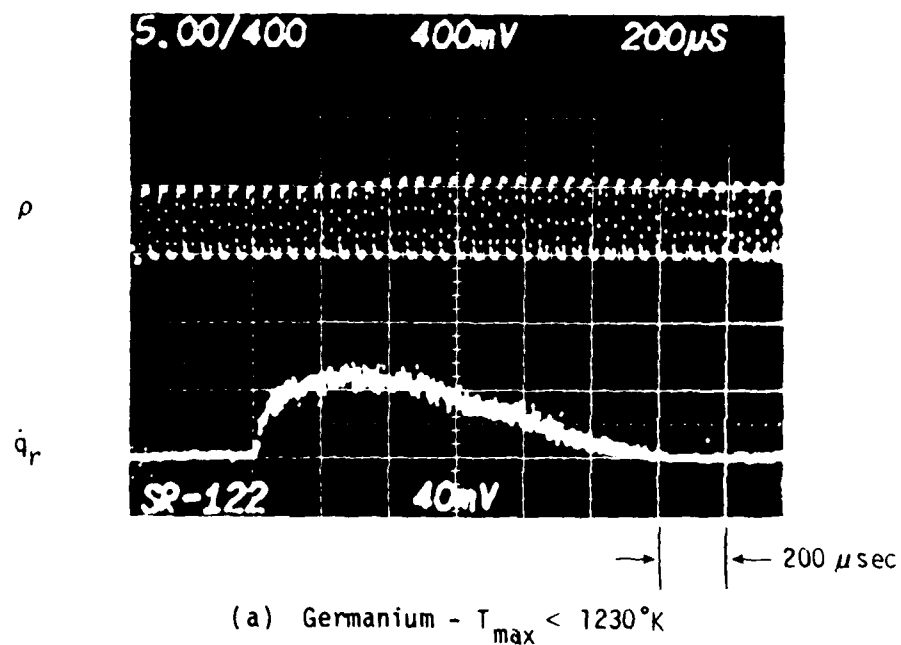


Fig. 27. Reflectance Below Melting Temperature

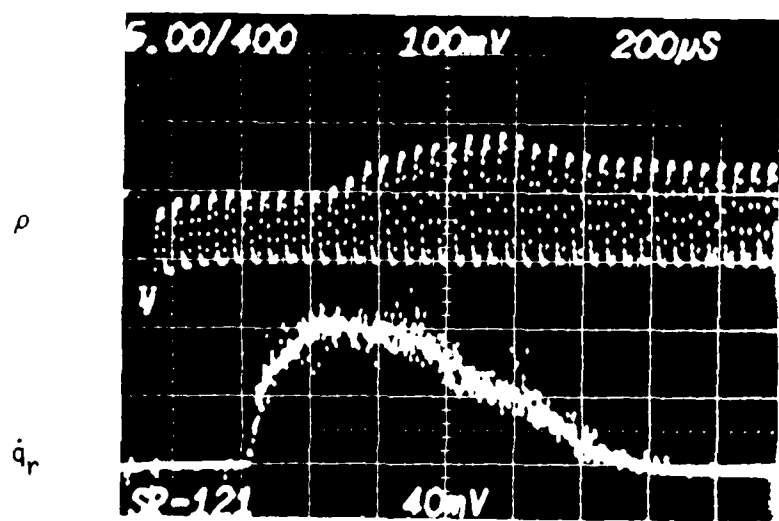
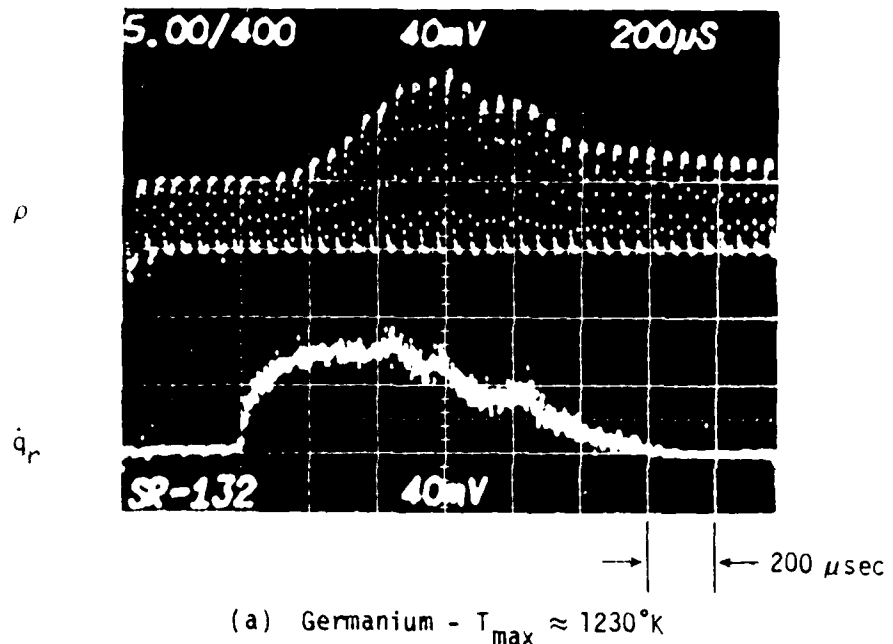


Fig. 28. Reflectance at Melting Temperature

The transient, bidirectional reflectance of roughened pyrolytic graphite during pulsed laser heating was over a wide range of temperatures by the same technique. Figures 29a through 29d show the reflectance response over the range of 2850°K to 4485°K. These temperatures assume a surface emissivity of 0.9 at the pyrometer detection wavelength of 0.81 μm , which has been found to be a reasonable value for graphite.²⁰ In these oscilloscope photos, the upper trace is the relative reflectance signal and the lower trace is the surface temperature signal. At the temperatures to which the graphite samples were heated, the continuum thermal radiation flux from the heated surface area within the spectral bandpass of the pyrometer becomes greater than the He/Ne laser beam flux after diffuse reflection from the roughened surfaces and into the solid angle viewed by the pyrometer. This causes an increase in the overall intensity of the chopped reflectance signal as seen in Figs. 29a and 29b. In contrast, a change in surface reflectance is indicated by an increased height (peak to valley) of the chopped signal. Thus, it was necessary to electronically subtract the pyrometer signal from the reflected He/Ne beam detector signal to obtain adequate sensitivity for the chopped reflectance signal at the highest temperatures. This subtraction process coupled with the low level of He/Ne beam flux from diffuse reflection on the vaporization-roughened graphite surface causes the trace shape shown in Figs. 29c and 29d.

As illustrated in Fig. 29, typical pyrolytic graphite response was consistently observed in that the reflectance smoothly increased 30 to 40 percent during the time the surface temperature was above $\approx 3500^{\circ}\text{K}$, and returned to its initial value upon cooling. Below maximum surface temperatures of $\approx 3500^{\circ}\text{K}$, no changes in the surface reflectance were noted. The reflectance increase at the higher temperature is much smaller than that noted for Si and Ge when a melt layer was created. If a liquid carbon layer was formed on the roughened surface, it would be expected that the reflectance increase would be very large by virtue of the reflection surface changing from diffuse to specular in nature and the inherently greater reflectance of liquid phases. In fact, this has been observed in reflectance data on laser-heated roughened iron surfaces that have not been included in this report. In addition to the relatively small reflectance change during heating, post-test observations in these and previous experiments²¹ show no physical evidence of a melt phase having been present during pulsed laser heating.

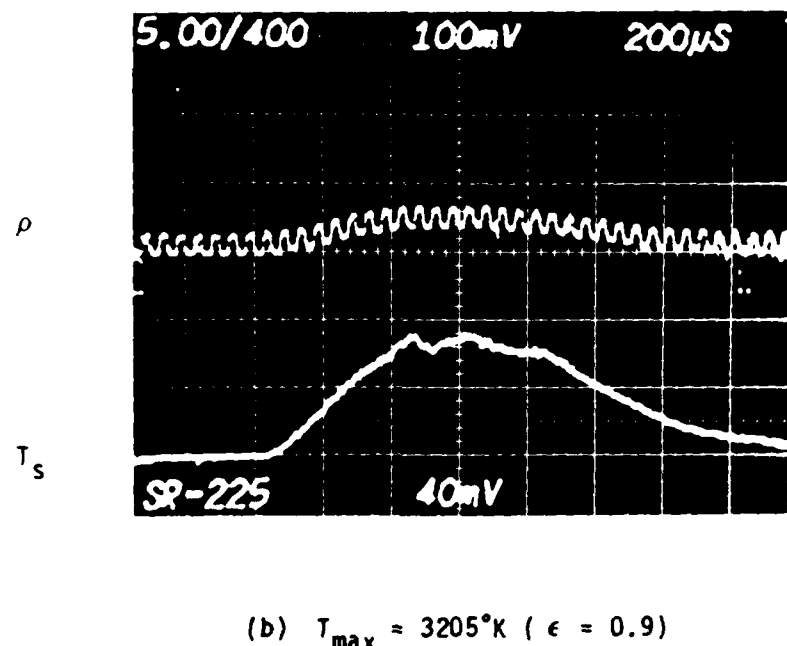
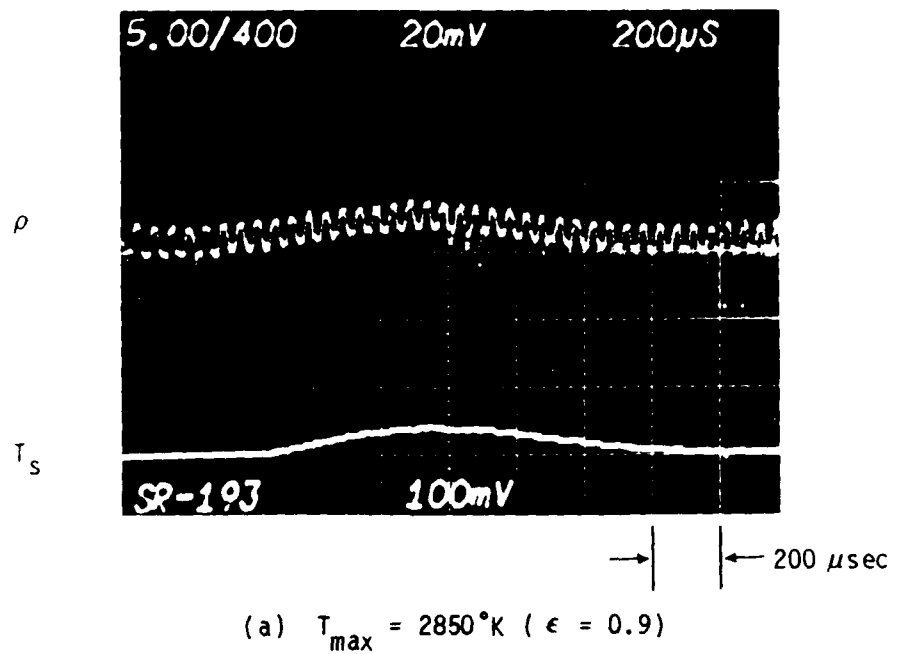
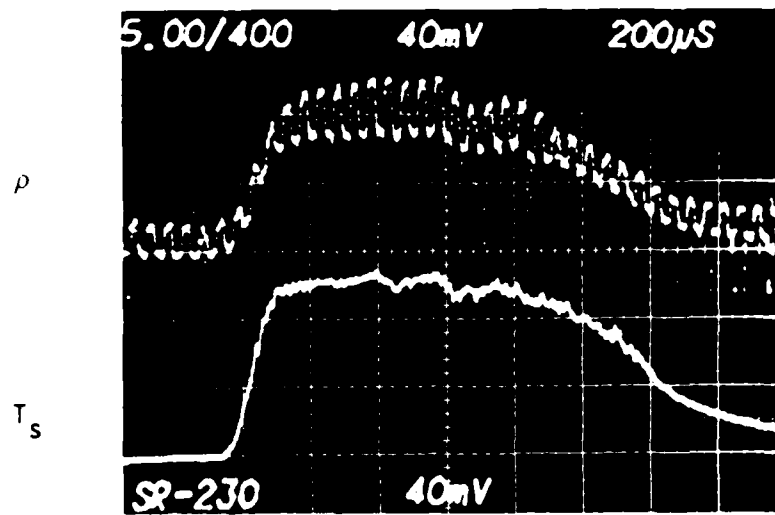
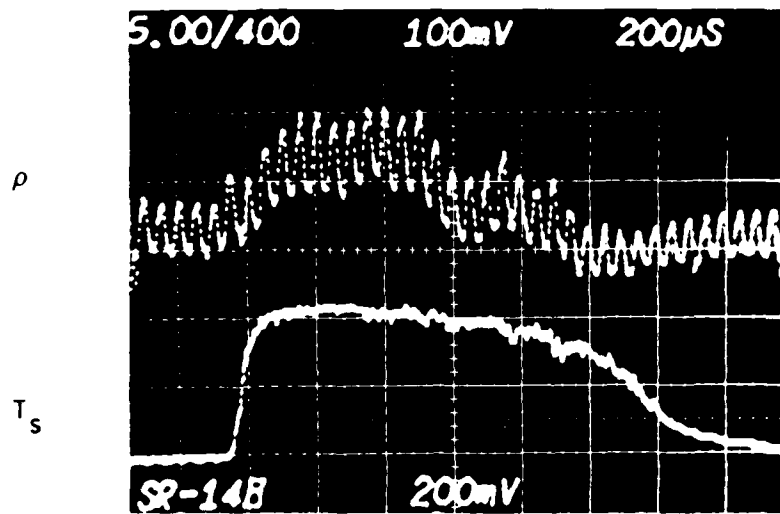


Fig. 29. Reflectance of Pyrolytic Graphite



(c) $T_{\max} = 4210^{\circ}\text{K}$ ($\epsilon = 0.9$)



(d) $T_{\max} = 4485^{\circ}\text{K}$ ($\epsilon = 0.9$)

Fig. 29. Reflectance of Pyrolytic Graphite (continued)

From these considerations, it is concluded that the observed small reflectance increase of pyrolytic graphite probably is not due to melting but, rather, to some alternative possibility such as a solid phase crystalline transition. The conclusion that the carbon triple point temperature is above 4500°K is in contrast to much of the earlier experimental results⁶ that suggested melting temperatures in the range of 3800 to 4200°K. However, as indicated previously, it is in agreement with the Livermore^{26,27} thermodynamic properties and thus further supports our previous conclusions concerning carbon vapor pressure and vaporization coefficients.

C. REMAINING QUESTIONS

The vapor pressure conclusion in Subsection III-B-2 is dependent upon the assumed emissivity. However, since the assumed value of unity (for viewing parallel to the a-b planes) is strongly supported by literature data,^{19,20} this conclusion should be considered firm. Likewise, because the melting conclusion is based upon a direct observational approach, this conclusion is also not likely to be in error. The vaporization coefficient conclusions below 4000°K would also appear to be defensible because of the reliability of the emissivity assumption.

For the pulsed laser data above 4000°K, the pyrolytic graphite was irradiated and viewed perpendicular to the a-b planes. The emissivity in this direction for an ablated surface is less well-known. The sensitivity of derived vaporization coefficients to the assumed emissivity value is seen in Fig. 17. An independent determination of the pyrolytic graphite emissivity (or surface temperature) is needed to reduce the uncertainty in the high temperature vaporization coefficient values. In addition, before reliable vaporization coefficients for the polycrystalline graphite, Graphnol (see Appendix B), can be obtained, it will be necessary to determine the emissivity of this carbon as a function of temperature for ablated surfaces.

Based upon the discussion in Subsection III-B-1, relatively strong dependence of the pyrolytic graphite vaporization coefficients on temperature may be the correct explanation of the "steep" slope of the data in Fig. 15. However, other possible explanations discussed in Subsection III-A-2, and not yet eliminated, need to be given further consideration. Therefore, we plan to look for condensed carbon particles directly in the free-jet plume by using a He-Ne laser and looking for backscattered radiation from carbon particulates. Also, we hope to be able to modify an existing method-of-characteristics inviscid plume computer code to address the question of energy release effects on Mach disk location.

IV. SUMMARY AND CONCLUSIONS

A new method, based upon the combined use of carbon laser ablation data and analytical modeling, has been used to determine carbon vapor pressure and vaporization coefficients at high temperatures (up to 4600°K). In addition, a surface reflectivity method has been used to place a lower limit on the melt temperature of carbon.

The consistently best agreement of total vapor pressure data with model predictions was obtained using carbon species thermochemical properties recommended by Lawrence Livermore Laboratory.^{26,27} In contrast, comparisons to the data with model predictions using JANAF-recommended properties showed consistently much less satisfactory agreement. On the basis of these comparisons and the more consistent agreement of the Livermore thermodynamic functions (heat of formation and entropy) with recent literature values,^{28,30} it was concluded that the vapor pressure of carbon is best represented by the Livermore properties. At 4000°K , the JANAF-predicted total vapor pressure is a factor of 2.5 smaller than the Livermore value. Above 4000°K , the importance of including the contributions of carbon species C_6 and especially C_7 to the total carbon vapor pressure is supported by the high temperature laser data. These species are included in the Livermore publications.

Until now, no information has been available concerning the temperature dependence or high temperature values of carbon species vaporization coefficients. From the carbon laser ablation data, vaporization coefficients consistent with the Livermore thermochemical data conclusion above have been derived. The values of vaporization coefficients obtained are sensitive to the assumed values of surface emissivity. Thus, particularly for the data above 4000°K , there is a need to accurately establish the emissivity of the pyrolytic graphite surface or to accurately measure the temperature by some other method (three-color photometry). If it is assumed that the high temperature emissivity is 0.97, then the high temperature and intermediate temperature vaporization coefficient data are in agreement at 4000°K .

An auxiliary He-Ne laser was used to monitor the carbon surface reflectivity as a function of time during the laser pulse. NASA data at measured temperatures up to 4500°K showed no evidence of the large increase in reflectivity expected when the surface melts. Such changes (increases) were successfully observed for other group IV-A elements. Thus, it was concluded that the melt temperature of carbon is greater than 4500°K.

The conclusions regarding vapor pressure and vaporization coefficients are important because the mass loss rate is proportional to the Langmuir pressure, i.e., the product of the vaporization coefficient and the vapor pressure. In addition, the melt temperature conclusion is technologically important, since melting could reduce the energy-dissipating efficiency by as much as a factor of three if the liquid carbon is stripped away without vaporizing.

REFERENCES

1. Dolton, T. A., H. E. Goldstein and R. E. Mauer, "Thermodynamic Performance of Carbon in Hyperthermal Environments," Progress in Astronautics and Aeronautics: Thermal Design Principles of Spacecraft and Entry Bodies, Vol. 21, Ed. J. T. Bevans, Academic Press, NY, 1969, pp. 169-201.
2. Baker, R. L., "Graphite Sublimation Chemistry Nonequilibrium Effects," AIAA Journal, Vol. 15, October 1977, pp. 1391-1397.
3. Kratsch, K. M., et al., "Graphite Ablation in High Pressure Environments," AIAA Paper 68-1153, 1968.
4. JANAF Thermochemical Tables, National Bureau of Standards, NBS-37, June 1971.
5. Baker, R. L. and P. G. Crowell, "Graphite Material Ablation Performance in High Thermal Radiation Environments," Progress in Astronautics and Aeronautics: Entry Heating and Thermal Protection, Vol. 69, Ed. W. Olistad, AIAA, NY, 1980, pp. 198-221.
6. Palmer, H. B. and M. Shelef, "Vaporization of Carbon," Chemistry and Physics of Carbon, Vol. 4, Ed. P. L. Walker, Jr., Marcel Dekker, Inc., NY, 1968.
7. Baker, R. L., "An Irreversible Thermodynamics Model for Graphite Sublimation in Radiation Environments," Progress in Astronautics and Aeronautics: Outer Planet Heating and Thermal Protection Systems, Vol. 64, Ed. R. Viskanta, AIAA, NY, 1979, pp. 210-227.
8. Zavitsanos, P. D., "The Vaporization of Pyrolytic Graphite," General Electric Co., GE R 66SD31, May 1966.
9. Margrave, J. L., ed., The Characterization of High-Temperature Vapors, John Wiley & Sons, NY, 1967.
10. Baker, R. L., "Carbon Nonequilibrium Phase Change," Office of Naval Research Interim Report, TR-0081(6728-02)-1, The Aerospace Corporation, El Segundo, CA, December 1981.
11. Anisimov, S. I., "Vaporization of Metal Absorbing Laser Radiation," Soviet Physics JETP, Vol. 27, No. 1, 1968, pp. 182-183.
12. Bird, G. A., Molecular Gas Dynamics, Oxford University Press, London, 1976.

REFERENCES (Continued)

13. Rosenblatt, G. M., Personal Communication, Pennsylvania State University, Department of Chemistry, University Park, PA.
14. Kleinschmidt, P. D. and G. M. Rosenblatt, "Relative Vaporization Rates of $As_2(g)$ and $As_4(g)$ from an Arsenic (111) Surface," American Society of Mass Spectrometry Meeting, June 1977.
15. Resler, E. L., "The Shock Tube and Chemical Kinetics," Fluid Dynamics and Applied Mechanics, Ed. Diaz and Pai, 1961, pp. 125-145.
16. Turner, J. S., "Discrete Simulation Methods for Chemical Kinetics," Journal of Physical Chemistry, Vol. 81, 1977, pp. 2379-2408.
17. Turner, J. S., "From Microphysics to Macrochemistry via Discrete Simulations," Computer Modeling of Matter, ACS Symposium Series No. 86, American Chemical Society, Washington, D.C., Ed. P. Lykos, pp. 231-264.
18. Auston, D. H., et al, "Time Resolved Reflectivity of Ion-Implanted Silicon During Laser Annealing," Applied Physics Letters, Vol. 33, 1978, pp. 437-440.
19. Pyrolytic Graphite Handbook, Metallurgical Production Department, General Electric Company, Schenectady, NY, 1964, as quoted in Gokcen, N.A., et al., "Determination of Graphite/Liquid/Vapor Triple Point by Laser Heating," High Temperature Science, Vol. 8, June 1976, pp. 81-97.
20. Touloukian, Y. S., ed., Thermophysical Properties of Matter, Vol. 8, IFI/Plenum Press, NY, 1970.
21. Covington, M. A., G. N. Liu, and K. A. Lincoln, "Free-jet Expansions from Laser-vaporized Planar Surfaces," AIAA Journal, Vol. 15, August 1977, pp. 1174-1179.
22. Ashkenas, H. and F. S. Sherman, Rarefied Gas Dynamics, Vol. 2, Ed. J. H. de Leeuw, Academic Press, NY, 1966, p. 84.
23. Rosenblatt, G. M., "The Role of Defects in Vaporization: Arsenic and Antimony," Surface Defect Properties of Solids, Vol. 5, 1976, pp. 36-64.
24. Wen, Y. S., "Derivation of the Free-jet Mach-disk Location Using the Entropy-balance Principle," Physics of Fluids, Vol. 18, No. 11, pp. 1421-1425.
25. Rosenblatt, G. M., "Evaporation from Solids," Treatise on Solid State Chemistry, Vol. 6a, Ed. N. B. Hannay, Plenum Press, NY, 1976, p. 199.

REFERENCES (Concluded)

26. Lee, E. L. and R. H. Sanborn, "Extended and Improved Thermal Functions for the Gaseous Carbon Species C₁-C₇ from 298 to 10,000°K," High Temperature Science, Vol. 5, 1973, pp. 438-453.
27. Leider, H. R., O. H. Krikorian, and D. A. Young, "Thermodynamic Properties of Carbon Up to the Critical Point," Carbon, Vol. 11, 1973, pp. 555-563.
28. Wachi, F. M. and D. E. Gilmartin, "Heat of Formation and Entropy of C₃ Molecule," High Temperature Science, Vol. 4, No. 5, pp. 423-431.
29. Strauss, H. L. and E. Thiele, "Thermodynamics of C₃. II. General Methods for Nonrigid Molecules at High Temperatures," Journal of Chemical Physics, Vol. 46, No. 7, pp. 2473-2480.
30. Hansen, C. F. and W. E. Pearson, "A Quantum Model for Bending Vibrations and Thermodynamics Properties of C₃," Canadian Journal of Physics, Vol. 51, 1973, pp. 751-760.
31. Born, M., and E. Wolf, Principles of Optics, 2nd Edition, Permagon Press, NY, 1964.
32. Mosteller, L. P., and F. Wooten, "Optical Properties and Reflectance of Uniaxial Absorbing Crystals," J. Optical Society of America, Vol. 58, 1968, pp. 511-518.
33. Moss, T. S., Optical Properties of Semiconductors, Butterworths, London, 1961.
34. Shvarev, K. M., B. A. Baum, and P. V. Gel'd, "Optical Properties of Liquid Silicon," Soviet Physics-Solid State, Vol. 16, 1975, pp. 2111-2112.
35. Berman, M., H. R. Kerchner, and S. Ergun, "Determination of the Optical Properties of Absorbing Uniaxial Crystals from Reflectance at Oblique Incidence," J. Optical Society of America, Vol. 60, 1970, pp. 646-648.
36. Bundy, F. P., "The P, T Phase and Reaction Diagram for Elemental Carbon, 1979," J. Geophysical Research, Vol. 85, 1980, pp. 6930-6936.
37. Ferraz, A., and N. H. March, "Liquid Phase Metal-Nonmetal Transition in Carbon," Physical Chemistry of Liquids, Vol. 8, 1979, pp. 289-297.
38. Covington, A., "Ames Free-jet Laser Vaporization Experiments," Data Report, NASA Ames Research Center, Moffett Field, CA, September 1980.

APPENDIX A

DATA SUMMARY

The experimental data analyzed in this report are summarized in Tables A-1 and A-2 (CW laser data) and in Figs. A-1 through A-4 (pulsed laser data). A more complete description is given in Refs. 10 and 38. The data lines in Fig. A-4 were obtained by combining the information in Figs. A-1 through A-3.

³⁸Covington, A., "Ames Free-jet Laser Vaporization Experiments," Data Report, NASA Ames Research Center, Moffett Field, CA, September 1980.

Table A-1. Pyrolytic Graphite Ablation Data*

Laser Power (kw)	AMBIENT PRESSURE									
	TORR		ATM							
	0.5	1	0.005	0.02	0.05	0.1	0.2	0.25	0.5	1.0
1.59		3384°K 1.66mg/sec								
1.89		3455°K 2.51mg/sec								
2.18										3687°K 17.2mg/sec
2.32										
2.47		3560°K 7.80mg/sec								
2.83		3592°K 9.41mg/sec								
2.90										
3.05	3587°K 8.67mg/sec	3642°K 13.3mg/sec	3631°K 13.9mg/sec	3687°K 20.2mg/sec	3698°K 18.8mg/sec	3740°K 25.0mg/sec	3790°K 29.4mg/sec	3830°K 31.2mg/sec	3880°K 34.1mg/sec	
3.20						3731°K 18.7mg/sec				
3.34						3720°K 17.2mg/sec				
3.34								3760°K 37.9mg/sec		
3.79									3912°K 47.9mg/sec	
3.92										
4.10						3810°K 47.1mg/sec	3822°K 68.3mg/sec	3878°K 59.4mg/sec		
4.58									3884°K 72.9mg/sec	

*The numbers given in each column are the measured surface temperature and mass loss rate.

Table A-2. Graphol Ablation Data*

Laser Power (kw)	AMBIENT PRESSURE						
	Torr	Atm					
		1	0.05	0.1	0.2	0.5	1.0
1.45	2870°K 1.11mg/sec						
1.96	3335°K 1.89mg/sec						
2.04	3217°K 5.11mg/sec						
2.10		3400°K 18.0mg/sec					
2.33	3466°K 4.90mg/sec						
2.41			3532°K 18.0mg/sec		3521°K 18.2mg/sec		
2.76				3565°K 18.1mg/sec		3715°K 30.8mg/sec	
2.83	3535°K 12.5mg/sec						
2.83	3530°K 9.33mg/sec						
2.90						3687°K 30.6mg/sec	
2.91	3532°K 8.52mg/sec						
2.98	3565°K 11.7mg/sec						
2.98	3526°K 10.1mg/sec						
2.98							
3.05	3565°K 12.6mg/sec						
3.05	3520°K 11.3mg/sec		3570°K 21.4mg/sec				
3.05							
3.05						3648°K 27.3mg/sec	

*The numbers given in each column are the measured surface temperature and mass loss rate.

Table A-2. Graphol Ablation Data (Continued)

Laser Power (kw)	AMBIENT PRESSURE						
	Torr		Atm				
	1	0.05	0.1	0.2	0.5	1.0	1.05
3.19					3681°K 29.4mg/sec		
3.34		3609°K 27.0mg/sec					
3.41			3631°K 29.5mg/sec				
3.63					3754°K 37.2mg/sec		
3.99					3777°K 42.9mg/sec		
4.07	3600°K 31.6mg/sec						
4.21		3587°K 31.2mg/sec			3794°K 49.4mg/sec		
4.29							
4.36		3687°K 25.2mg/sec					
4.36			3665°K 46.8mg/sec				
4.36			3642°K 39.3mg/sec				
4.36				3687°K 42.4mg/sec			
4.36					3833°K 56.5mg/sec		
4.50					3743°K 68.8mg/sec		
4.58						3830°K 52.6mg/sec	
4.58						3833°K 47.5mg/sec	
5.30							3884°K 117mg/sec

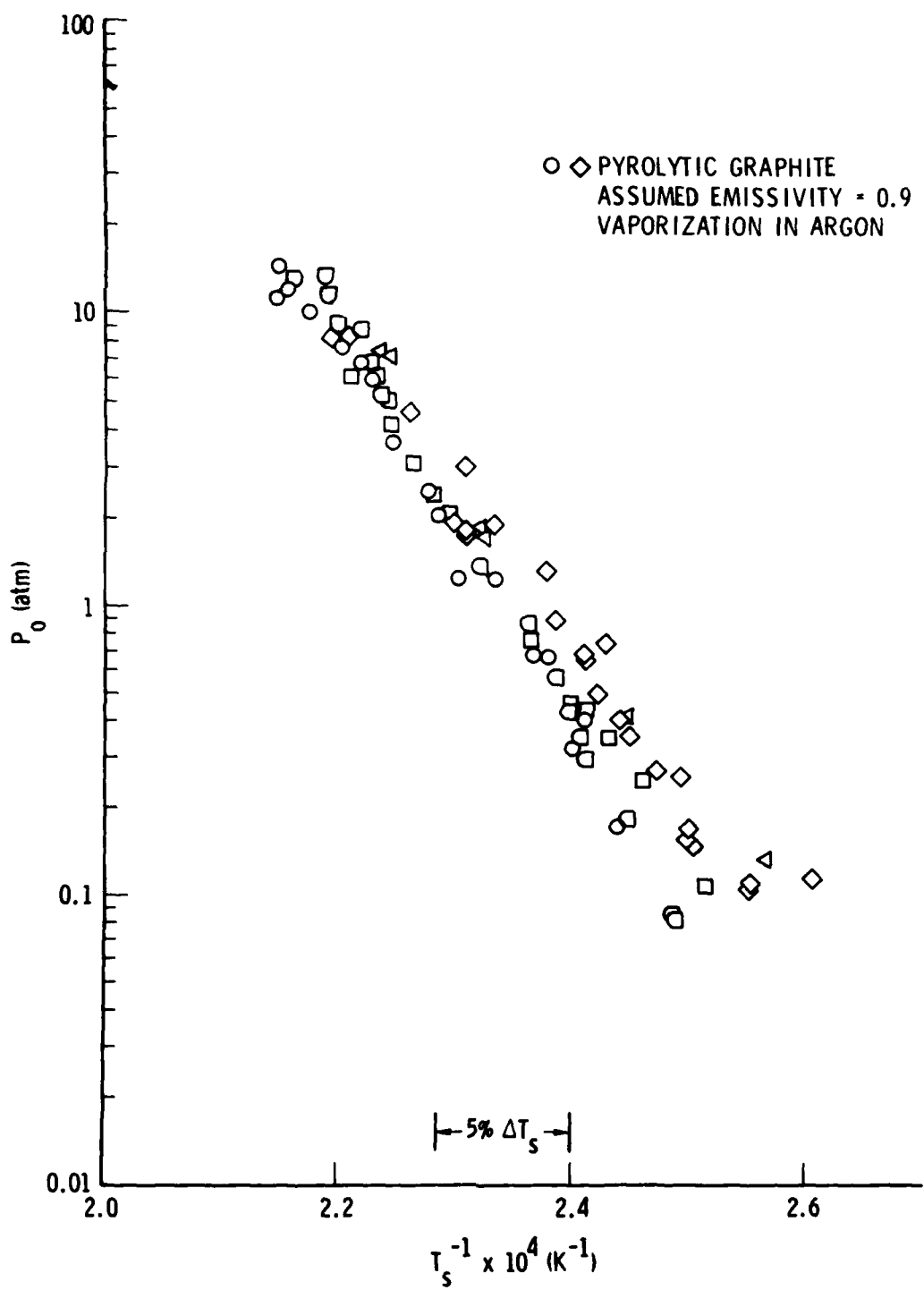


Fig. A-1. Free-Jet Peak Total Pressure versus Peak Surface Temperature

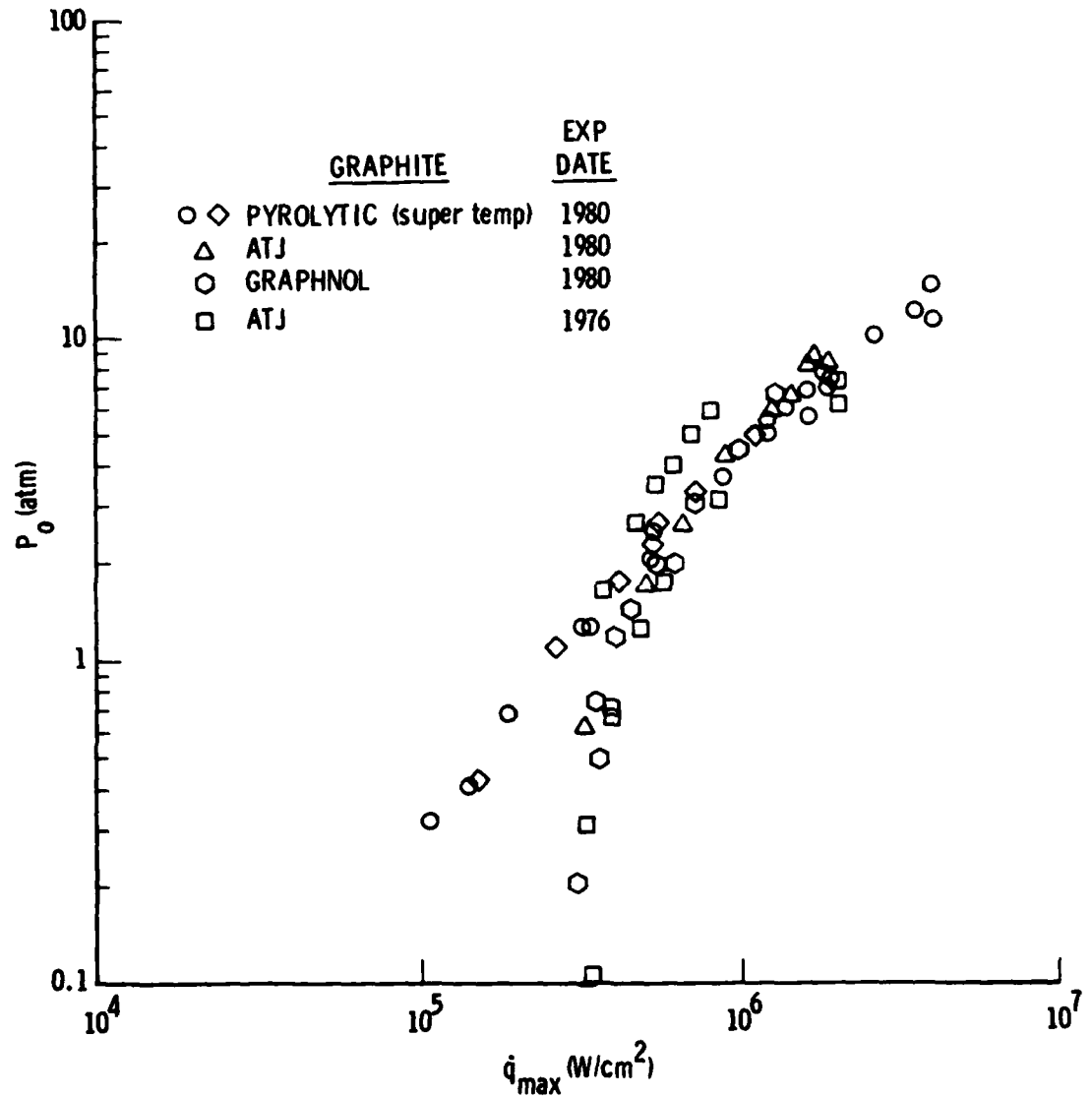


Fig. A-2. Derived Free-Jet Total Pressure versus Peak Laser Flux for Vaporization in Argon

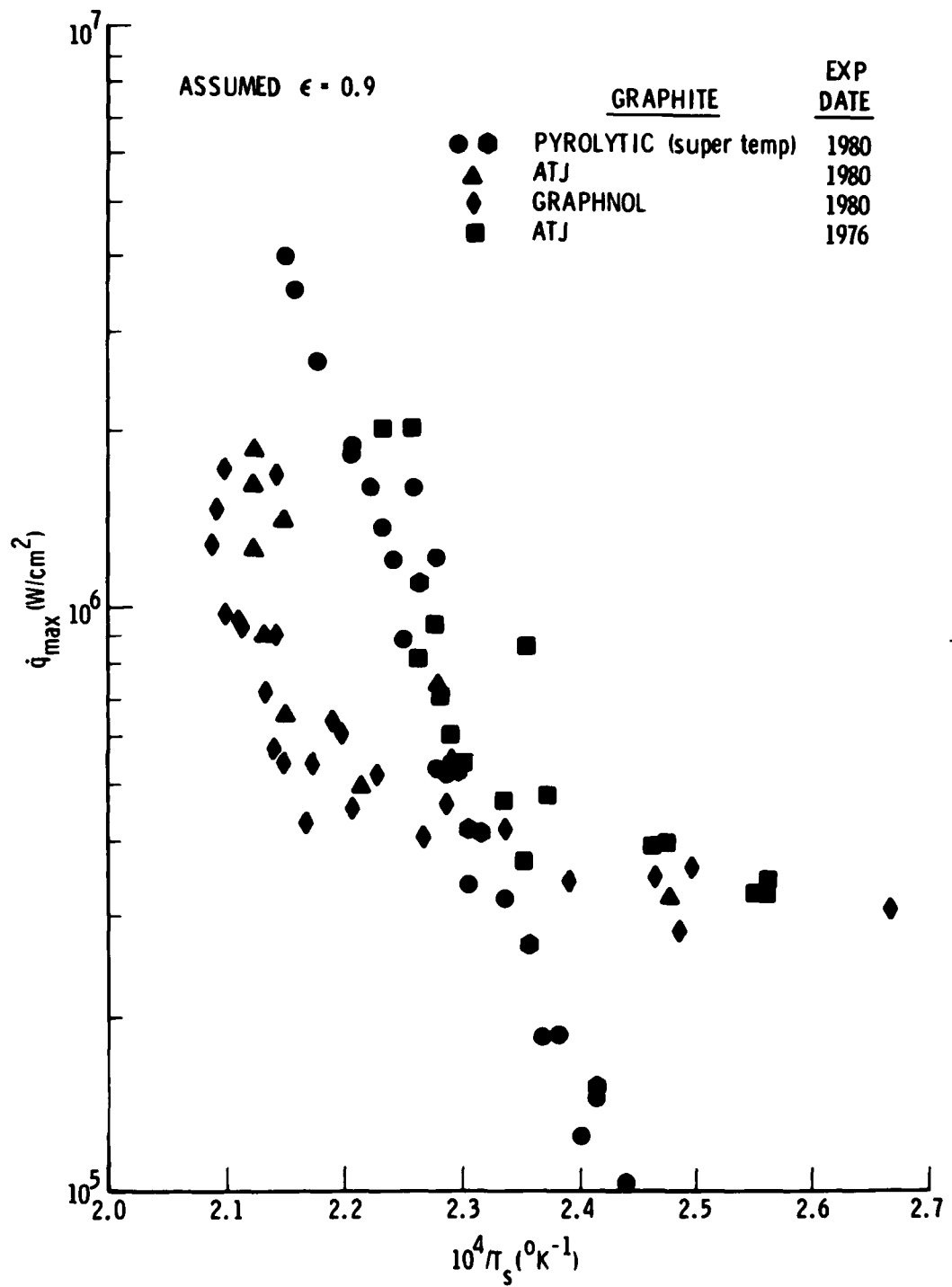


Fig. A-3. Peak Surface Temperature versus Peak Laser Flux for Vaporization in Argon

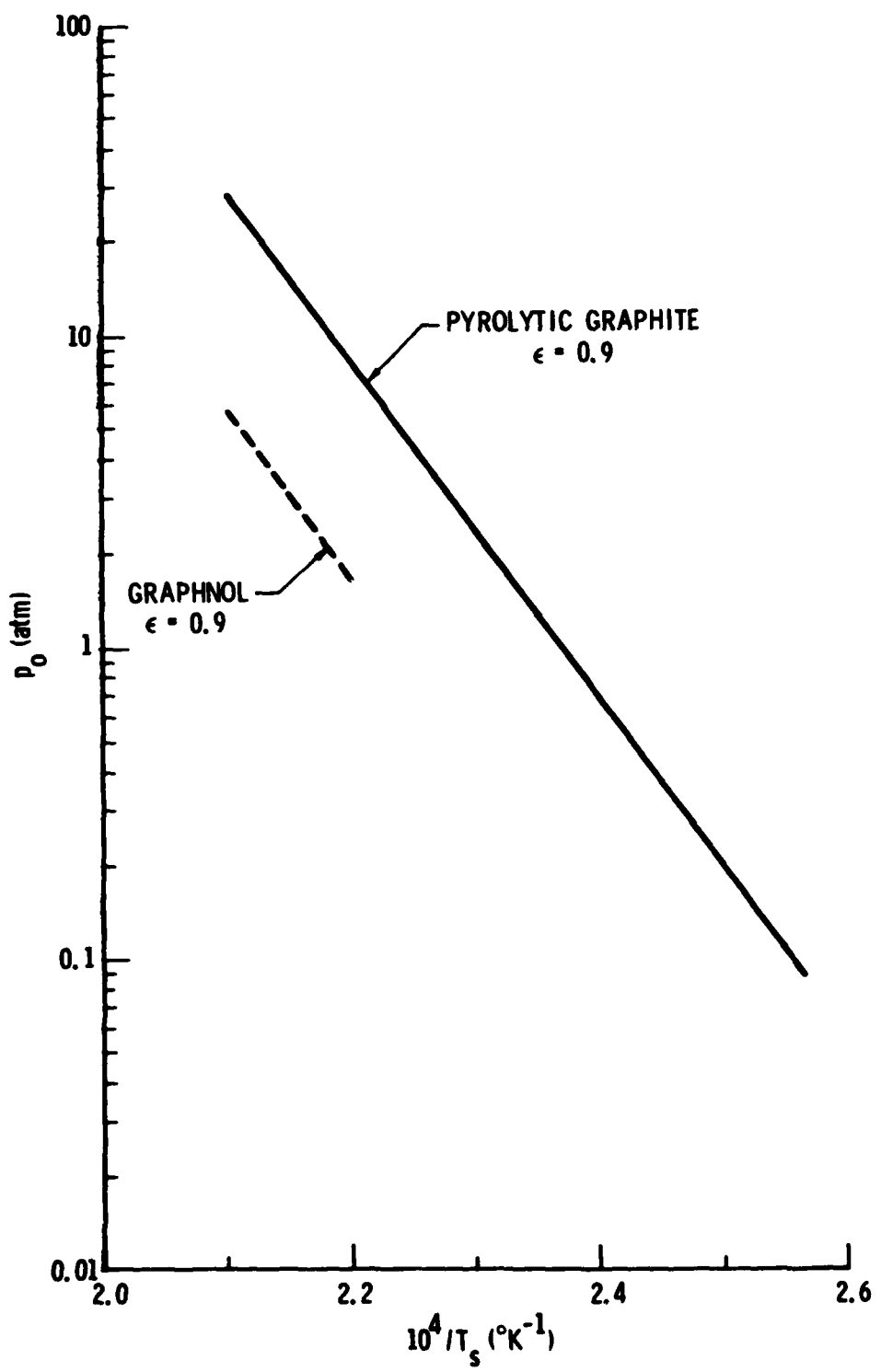


Fig. A-4. Comparison of Pyrolytic Graphite and Graphnol Data

APPENDIX B

GRAPHNOL DATA INTERPRETATION

As seen in the data summary given in Appendix A, a large quantity of experimental data were also obtained for the fine-grain polycrystalline graphite, Graphnol. Because the Graphnol thermal conductivity is nearly isotropic, the Graphnol cylindrical samples were heated to a bright glowing orange by axial conduction away from the laser irradiated area. This caused mass to be lost from the cylindrical surface due to heterogeneous reaction with oxygen in the ambient chamber atmosphere. A considerable effort was devoted to eliminating the oxidation mass loss contribution to the total mass loss so that the sublimation mass loss rates could be used to obtain vapor pressure and vaporization coefficient information. Unfortunately, no satisfactory unambiguous method of doing this was found, even for the very low pressure (1 Torr) data.

The 1 Torr data points from Appendix A are plotted in Fig. B-1. Also shown is the pyrolytic data line from Fig. 10. Note that both lines have about the same slope. Interpreting these data directly, as discussed in connection with Figs. 10 through 12 in the report, we conclude that the vaporization coefficient for Graphnol is greater at a given temperature than that for pyrolytic graphite by a factor of about 1.7. The amount of mass lost by oxidation is not known, and the emissivity of the Graphnol is likely to be less than unity (as assumed in the data reduction). Since correction for both these effects would reduce the vaporization coefficients derived from the data, it is probable that the vaporization coefficient for Graphnol is actually less than that for pyrolytic graphite at a given temperature.

The high temperature Graphnol data from Appendix A, when interpreted as discussed in the report (see discussion of Figs. 13 through 16), give vaporization coefficients as seen in Fig. B-2. Again, shown for comparison is the pyrolytic graphite data line from Fig. 16. If the emissivity of Graphnol and pyrolytic graphite are about the same, then these results indicate that carbon vaporization coefficients for Graphnol are approximately a factor of 5 smaller than those for pyrolytic graphite at a given temperature.

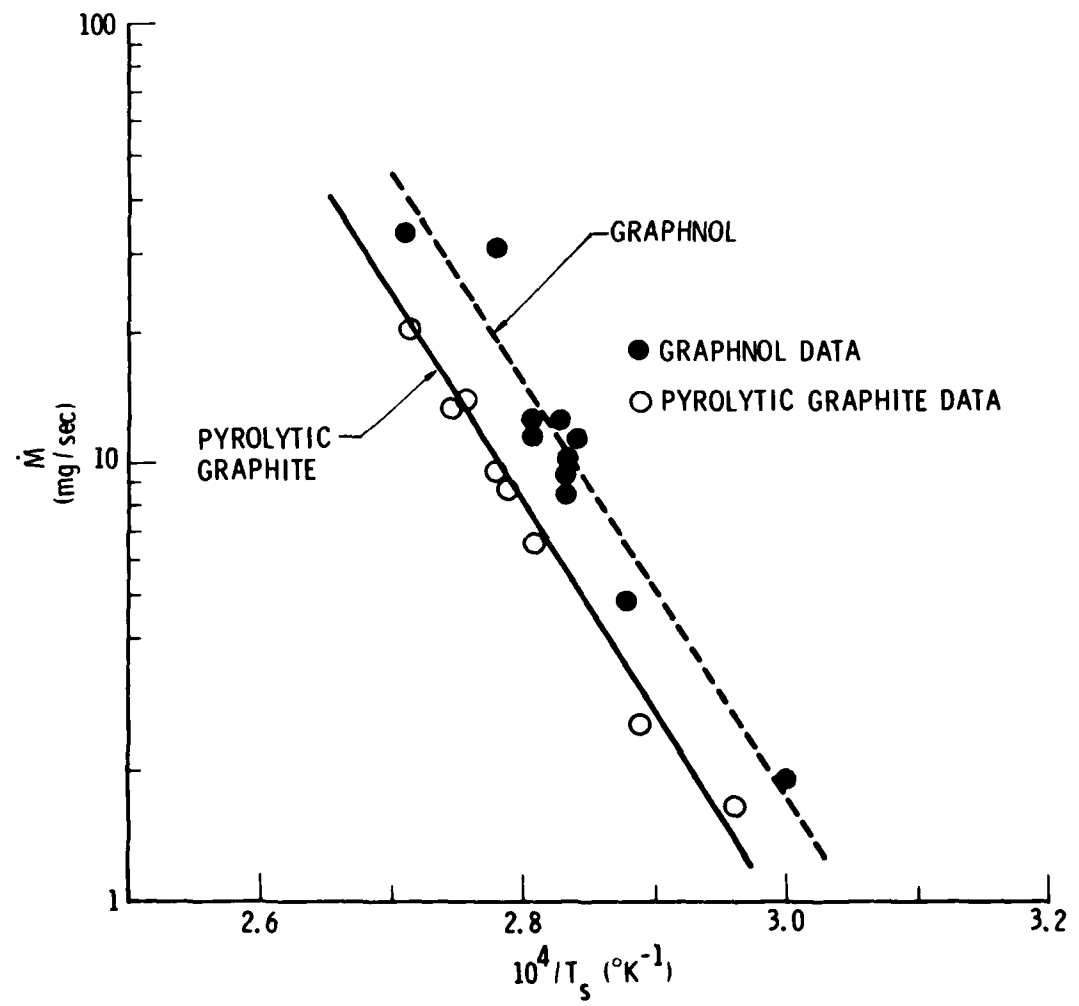


Fig. B-1. Comparison of Low Pressure Pyrolytic Graphite and Graphnol Mass Loss Rate Data

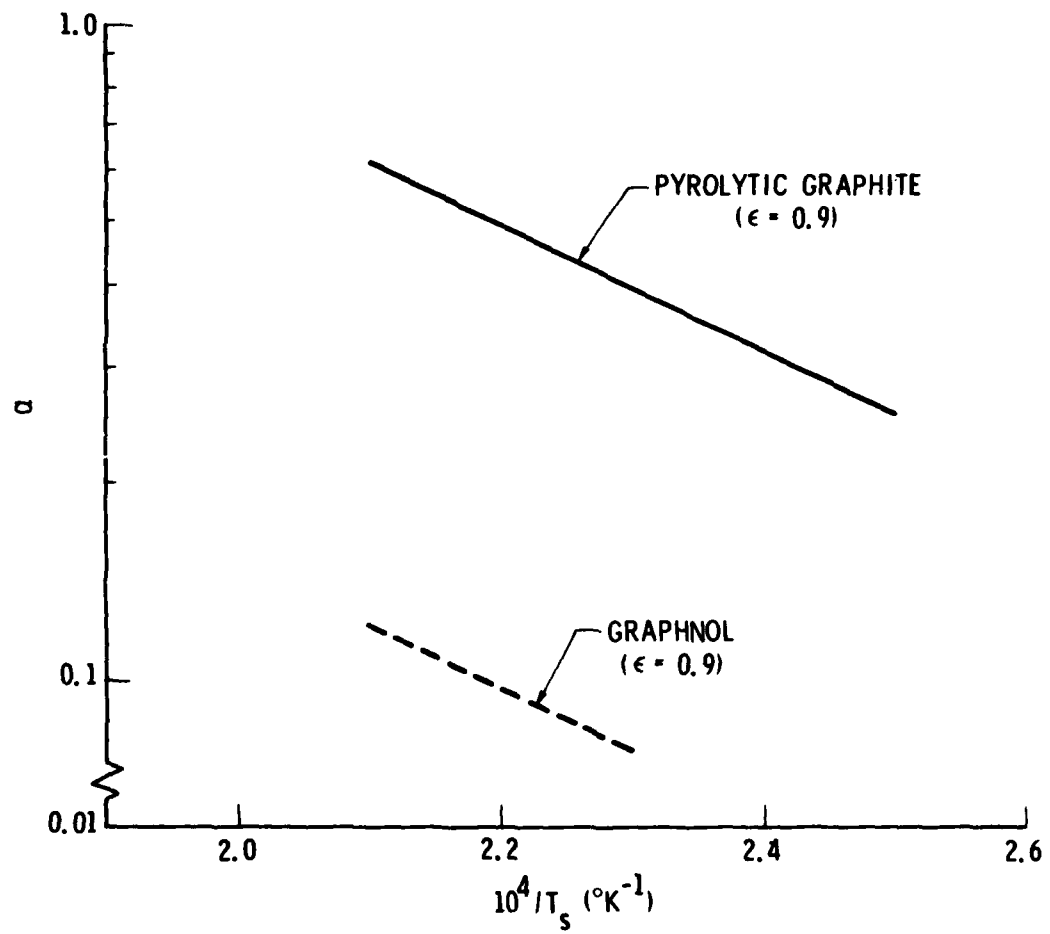


Fig. B-2. Vaporization Coefficients (Livermore)
Derived from Pulsed Laser Data

APPENDIX C

INFORMATION AVAILABLE FROM CW VERSUS PULSED LASER DATA

As indicated schematically in Fig. 8, carbon vapor pressure information is obtained only from the CW laser data. The purpose of this Appendix is to discuss why vapor pressure information cannot be derived from the pulsed laser data.

The theoretical model predictions (Subsection II-A) can best be summarized by referring to Fig. 20. When the ambient pressure p_a is much less than the carbon-saturated vapor pressure p_s at temperature T_s , then the predicted mass loss rate-surface temperature behavior is described by the straight line in Fig. 20a. From the CW laser data shown in Fig. 20a or the pulsed laser data shown in Fig. 15, the Langmuir vapor pressure can be obtained via Eq. (11). Then, once p_s is obtained by independent means, Eq. (11) can be solved for the vaporization coefficient α .

When the above condition, i.e., $p_a \ll p_s$, is not satisfied, the predicted mass loss rate-surface temperature behavior is described by the various curved lines (each for a different p_a) shown in Figs. 20b and 20c. In Figs. 21 through 23, CW laser data are compared with model predictions using different thermochemical data sets to determine the "more nearly correct" vapor pressure relationship. In order to do this, it is necessary that the data be in the curved lines region (see Fig. 20b) of the \dot{m} - $1/T_s$ plane. Since the pulsed laser data (Fig. 15) all lie in the straight line region of model predictions, the method applied to the CW data in Figs. 21 through 23 to obtain vapor pressure information cannot be used.

The reason that the pulsed laser data all lie along a straight line is fundamentally inherent to the experimental method, i.e., stagnation pressure p_0 is derived from measured Mach disk geometry. To have a Mach disk, the flow must be sonic (choked) at the surface and expand in a supersonic free-jet expansion. The condition required for sonic flow at the surface is $p_a \ll p_s$. From above, recall that this is the same condition as that required for the straight line \dot{m} versus $1/T_s$ behavior. Thus, all the pulsed laser data are in the straight-line region.

